Unravelling Off-pulse emission in outer magnetosphere of Pulsars.

A Thesis

Submitted to the
Tata Institute of Fundamental Research, Mumbai
for the degree of Doctor of Philosophy
in Physics

by

Rahul Basu

National Centre for Radio Astrophysics
Tata Institute of Fundamental Research
January, 2014

DECLARATION

This thesis is a presentation of my original research work. Wherever contributions of others are involved, every effort is made to indicate this clearly, with due reference to the literature, and acknowledgement of collaborative research and discussions.

The work was done under the guidance of Dr. Dipanjan Mitra, at National Center for Radio Astrophysics (NCRA), Tata Institute of Fundamental Research (TIFR), Pune.

.....
(Rahul Basu)

In my capacity as supervisor of the candidate's thesis, I certify that the above statements are true to the best of my knowledge.

.....
(Dr. Dipanjan Mitra)

Date:

Acknowledgements

It is a great pleasure to acknowledge the contribution of all the people who have helped me in my endeavour of completing this PhD. First and foremost I would like to express my deepest gratitude to Dipanjan Mitra who has been more than a Research supervisor and a constant source of encouragement. His excitement about pulsars is infectious and our multiple interactions over the years have been a source of learning and great fun.

I am grateful to Ramana Athreya for introducing me to Radio Astronomy and coding. I would like to thank Subhashis Roy, C. H. Ishwara Chandra, B. C. Joshi, Sandeep Sirothia, Nimisha Kantharia, Nissim Kanekar, Yogesh Wadadekar, Jayaram Chengalur, Yashwant Gupta for all their help.

A part of the thesis work was done during a month long stay at Zielona Góra, Poland. I would like to thank George I. Melikidze for many interactions which helped me understand Pulsar emission better. I would like to thank Jarek Kijak and Janusz Gil for their help during my stay. I would also like to thank Krzysztof Maciesiak and Marta Dembska for all their help.

I would like to thank the referees R. T. Gangadhara and Janusz Gil for their critical comments which helped to improve the thesis.

The process of working on a thesis can get quite tedious at certain points and I would take this opportunity to thank my friends at NCRA who supported me all along. I thank Aritra, Arun, Naren, Vishal, Raghu, Ujjwal for being there in my times of need. I would also like to thank Aditya, Yogesh, Rohit, Abhishek, Mayuresh, Prakash, Sambit, Viswesh, Nirupam, Chandreyee, Sanhita, Prasun, Jayanti, Kanan, Breezy, Jayanta, Bhaswati and others who made my stay in NCRA enjoyable.

I would like to thank the staff at NCRA for their help. I would also like to thank the staff at GMRT for their help during my multiple visits for observations and particularly the Telescope operators who were very patient with all my demands.

Finally, I am eternally grateful to my parents, my first teachers, for their support and encouragement at all stages of my life. I would also like to acknowledge the support of my younger brother Rajat.

Synopsis

The radio emission form a tiny fraction of the total energy released by pulsars during spin down. The majority of this energy is lost as high energy X-ray and γ-ray radiation and as a wind of relativistically charged particles flowing out into the ambient Inter Stellar Medium (ISM) in addition to the magnetic dipolar radiation. However, the radio emission is unique for its coherent nature which is demonstrated by the high brightness temperatures of all the radio emission components from pulsars. This puts significant constrains on not only the origin and mechanism of radio emission but also the general conditions in the pulsar magnetosphere and therefore serves as a very useful tool in their understanding. The idea of the presence of the inner vacuum gap above the magnetic poles acting as a source of relativistic outflowing plasma (Sturrock 1971; Ruderman & Sutherland 1975) has been necessitated to explain the origin of the radio emission from pulsars. The conventional pulsar radio emission is pulsed in nature, occupying a fraction of the pulsar period and their polarization features demonstrate traits of their origin from dipolar magnetic field lines (Radhakrishnan & Cooke 1969). Detailed theoretical modelling have revealed two locations in the pulsar magnetosphere where coherent radio emission can originate, in the inner magnetosphere at heights of 50 R_S (Melikidze et al. 2000; Gil et al. 2004), where R_S being the radius of neutron star, and at the outer magnetosphere near the light cylinder (Kazbegi et al. 1987, 1991; Lyutikov et al. 1999). In the inner magnetosphere nonlinear instabilities develop in the outflowing plasma leading to charge bunching which instigate a large number of charged particles to emit in phase. One of the major developments in our understanding of pulsar radio emission has been the observational

demonstration of emission heights of the main pulse emission to be 20–50 R_S (Rankin 1993a; Blaskiewicz et al. 1991; Kijak & Gil 1997; Gangadhara & Gupta 2001). This indicates the bunching mechanism in the inner magnetosphere as a likely source of the radio emission within the framework of the inner vacuum gap. But the question that stands out is the manifestation of the mechanism in the outer magnetosphere which is also a likely outcome of the pulsar process and the possibilities of identifying them. The present thesis is an attempt to address the prospect of radio emission in the outer magnetosphere of pulsars. The radio emission from pulsars originate in the outflowing plasma moving along the open dipolar field lines. The main pulse emission originate in the inner magnetosphere implying that any other emission originating higher up would likely be seen far away from the main pulse emission. This may be manifested as either a continuum background radiation along the baseline of the pulsar profile or a pulsed component far away from the main pulse.

Offline-Gating Technique

The main observational part of this thesis is devoted to search for and categorize the presence of any baseline emission in the pulsar profile away from the pulsed region. The conventional pulsar observations were unsuitable for these studies owing to the inadequate understanding of the baseline level. In order to address this issue we developed the technique of 'Offline-Gating' to separate the On- and Off-pulse data and image them independently to look for the presence of any low level emission in the Off-phase coincident with the On-pulse. This was carried out using the high time resolution (128/256 millisecond) mode of the Giant Meterwave Radio Telescope (GMRT) interferometer and observing long period pulsars (Period $>$ 1.3 seconds) to enable secure separation of the two gates. The interferometric data were folded with the periodicity of the pulsar studied to determine the On- and Off-phases. The data file was copied into two parts and on each part a gate was set up to keep only the On and Off-phase data respectively and edit out the rest. Each of these files were now imaged using standard imaging techniques (NRAO AIPS software) to look for

Off-pulse emission in the position of the On-pulse. The signals in the Off-pulse were expected to be very sensitive to systematics in the receiver chain and careful tests were devised to identify any spurious detections. In particular we looked for noise correlations along adjacent time bins and also checked for leakage in the data chain using a pulsed noise source generator. However, we failed to detect any spurious signals in the Off-phase due to inconsistencies in the telescope system.

Off-pulse emission from Pulsars

We used the 'Offline-Gating' technique to search for Off-pulse emission in six long period pulsars B0525+21, B2045–16, B1237+25, B0834+06, B0320+39 and J2144–3933 at the 325 MHz and 610 MHz frequency band of the GMRT. We succeeded in detecting faint Off-pulse emission ($\leq 1\%$ of peak pulsar flux) in five long period pulsars at both the observing frequencies, J2144–3933 being the only instance of non detection, which were the first secure detections of Off-pulse emission from pulsars, to the best of our knowledge. Two of the pulsars B0525+21 and B2045–16 were observed during multiple epochs and Off-pulse emission were detected at each instance. The ISM densities required to drive a Pulsar Wind Nebulae (PWN) for these weak pulsars turned out be too improbable to explain a PWN origin of the Off-pulse emission (Frail & Scharringhausen 1997). We looked for observational traits of the Off-pulse emission in order to characterize their nature and origin in the pulsar magnetosphere. The Off-pulse emission showed flux variation at all time scales due to scintillation in the ISM. However the variation in the Off-pulse flux closely followed the changes in the On-pulse flux in all the pulsars at both short and long timescales. Using the refractive scintillation timescales (Stinebring & Condon 1990; Bhat et al. 1999; Stinebring et al. 2000) for the pulsars we have estimated the upper limits for the emission heights of Off-pulse emission which indicate a magnetospheric origin of Off-pulse emission. In addition we have also estimated the spectral index of Off-pulse emission at low radio frequencies between 325 MHz and 610 MHz. The Off-pulse emission appear to exhibit a steep spectra similar to the On-pulse emission for the pulsars B0525+21, B2045–16

and B0320+39. However the Off-pulse spectra undergoes flattening for B0834+06 and show turnover in the case of B1237+25. We need to understand how the emission beam is illuminated at the location of the Off-pulse emission and distortions due to propagation effects, aberration-retardation, etc. before we can fully comprehend the diversity in the Off-pulse spectra.

Emission Mechanism in Outer Magnetosphere

The magnetospheric origin of the Off-pulse emission enabled us to estimate their brightness temperatures which turned out to be $\geq 10^{18}$ K indicating the emission to be coherent like the main pulse. In addition the location of the Off-pulse emission far away from the main pulse in the pulsar profile and the underlying dipolar geometry of the pulsar indicated the emission to originate higher up in the pulsar magnetosphere. The cyclotron resonance instability is postulated to develop in the outer magnetosphere of pulsars (Kazbegi et al. 1987, 1991; Lyutikov et al. 1999) and serves as a possible source of coherent radio emission. We have looked into the possibility of the instability developing in the five pulsars with detected Off-pulse emission and found the conditions to be favorable. In addition we have also demonstrated the mechanism to be energetically viable to explain the detected Off-pulse emission from the five pulsars. However, our studies were based on initial estimates and detailed modelling is required taking into account the illumination of the emission beam, the exact location of emission, propagation effects, spectral behaviour of Off-pulse emission, polarization characteristics, etc., for a thorough understanding of the Off-pulse emission process within the purview of this emission mechanism.

Pre-Cursor emission from Pulsars

The core-cone morphology have been successful in explaining the underlying structure of the main pulse emission in a vast majority of normal pulsars. However the

pre-cursor emission (Backus et al. 2010; Mitra & Rankin 2011) seen in a handful of pulsars seem to be incompatible with this picture. We have investigated four pulsars with signatures of pre/post-cursor emission components within the purview of the established geometrical picture with particular emphasis on pulsars B1822–09 and B2224+65 which have been observed over a wide radio frequency range. The multi frequency studies reveal that the post-cursor component in B2224+65 resembles an outer cone emission. The pre-cursor component in B1822–09, B1322+83 and B0943+10 however cannot be reconciled within the standard mechanism. We have demonstrated the morphological differences of pre/post-cursor from the wider outer cone emission and in the process also tried to characterize the morphology of the pre-cursor emission. The presence of pre-cursor emission raises interesting questions about their origin with respect to the main pulse. The dipolar geometry of the pulsar magnetosphere constrain the precursor emission to originate higher up the open field lines thereby highlighting the possibility of a different emission mechanism being involved.

In this thesis we have studied radio emission which originate far away from the main pulse emission in pulsars, in the form of Off-pulse and pre-cursor emission. In the standard geometrical picture of pulsars we have demonstrated these emission components to originate higher up the pulsar magnetosphere. We have explored cyclotron resonance mechanism originating in the outer magnetosphere which is consistent with the Off-pulse emission and may also be the source of pre-cursors. The radio emission seem to encompass two distinct regimes in pulsars, the conventional main pulse emission originating in the inner magnetosphere and the distinct class of Off-pulse emission and pre-cursors which originate in the outer magnetosphere near the light cylinder.

List of Publications

Refereed publications:

1. **Basu, R.**; Mitra, D.; Melikidze, G. I.; "An Emission Mechanism Explaining Off-pulse Emission Originating in the Outer Magnetosphere of Pulsars", 2013, The Astrophysical Journal, 772, 86

2. Hermsen, W.; Hessels, J. W. T.; Kuiper, L.; van Leeuwen, J.; Mitra, D.; de Plaa, J.; Rankin, J. M.; Stappers, B. W.; Wright, G. A. E.; **Basu, R.**; et al.; "Synchronous X-ray and Radio Mode Switches: A Rapid Global Transformation of the Pulsar Magnetosphere", 2013, Science, 339, 436

3. **Basu, R.**; Mitra, D.; Athreya, R.; "On the Nature of Off-pulse Emission from Pulsars", 2012, The Astrophysical Journal, 758, 91

4. **Basu, R.**; Athreya, R.; Mitra, D.; "Detection of Off-pulse Emission from PSR B0525+21 and PSR B2045-16", 2011, The Astrophysical Journal, 728, 157

In Preparation:

1. **Basu, R.**; Mitra, D.; Rankin, J.M.; "Pre/Post-Cursors: A distinct radio emission from Pulsars.", 2014, to be submitted.

Others:

1. **Basu, R.**; Mitra, D.; Athreya, R.; "Off-pulse Emission from Long Period Pulsars", Electromagnetic Radiation from Pulsars and Magnetars. Proceedings of a Conference held at University of Zielona Góra, Zielona Góra, Poland, 24-27 April 2012. San Francisco: Astronomical Society of the Pacific, 2012., p.71

2. Athreya, R.; **Basu, R.**; Mitra, D.; "Gated interferometric imaging of pulsars to detect off-pulse emission", General Assembly and Scientific Symposium, 2011 XXXth URSI, 13-20 August. 2011, p.1-4

Contents

List of Figures

List of Tables

Chapter 1

Introduction

The radio emission from pulsars is one of the most fascinating phenomenon in modern astrophysics. The pulsars are rapidly rotating neutron stars emitting bursts of radio pulses (usually 10% of the time) and are supposedly radio quiet for the rest of the period. The neutron star is characterized by mass of $1.4M_{\odot}$ and radius of around 10 km and is also believed to harbour very high magnetic fields whose dipolar component is of the order of 10^{12} gauss on the stellar surface. The neutron stars exhibit fast spin periods ranging from few milliseconds to a few seconds which manifest as the interval between successive pulses. The neutron stars can be categorized into two main classes the accretion powered X-ray binaries and the rotation powered pulsars. The rotation powered radio pulsar slows down with time as the pulsar looses energy due to loss of dipolar radiation of the spinning magnet and can be further classified into young pulsars, middle aged/old pulsars and millisecond pulsars. The young pulsars are highly energetic with high spin down rates and fast periods of several tens of milliseconds. The young pulsars are also known to emit high energy radiation in the X-ray and γ-ray frequencies. The middle aged and old pulsars, also known as normal pulsars, with periods ranging from a few hundred milliseconds to several seconds, form the majority of the pulsar population and is the subject of our present studies. In addition there are also the millisecond pulsars which are expected to be recycled burnt out pulsars with periods of few milliseconds.

Radio Pulsars have been extensively studied since their discovery by Hewish et al.

(1968) more than four decades ago. The radio emission form a tiny fraction of the total electromagnetic radiation emitted by pulsars but it is distinguished by its coherent nature. This is reflected in the high brightness temperatures ($\sim 10^{30}$ K) associated with the radio emission. The coherent emission requires a specialized emission mechanism where a large number of charged particles must radiate in phase. A number of sophisticated observations coupled with theoretical advances over the past few decades have revealed great details about the radio emission mechanism in normal pulsars. Though a comprehensive mechanism explaining the overall radio emission is still at large we have nonetheless gained a basic understanding of the underlying physical processes necessary for the origin of radio emission. In the subsequent sections of this chapter we present the current understanding about the physical conditions around the neutron star necessary for the generation of radio emission in normal pulsars.

1.1 Physical Characteristics

The presence of any electromagnetic radiation requires one or multiple regions in or around the pulsar capable of producing and/or accelerating charged particles. A large number of possible sites have been proposed in the literature ranging from the Inner Acceleration Region as a Vacuum Gap above the polar caps (Sturrock 1971; Ruderman & Sutherland 1975) to the Outer Gap originating higher up the magnetosphere (Cheng et al. 1986a,b) and intermediates like the Slot Gap and Extended Outer Gaps (Arons 1983). In this thesis we take the viewpoint that the coherent radiation leading to the main pulse emission in normal pulsars originates as a result of curvature radiation from charged bunches (like solitons) at emission heights of $\sim$ 500 km above the stellar surface (e.g. Cordes 1978; Blaskiewicz et al. 1991; Rankin 1993a; Kijak & Gil 1997, 1998, 2003; Malov & Suleimanova 1998; Mitra & Deshpande 1999; Gangadhara & Gupta 2001; Mitra & Li 2004; Krzeszowski et al. 2009). The Inner Acceleration Region produces spark associated nonstationary, relativistic, singly charged primary particles ($\gamma_b \sim 10^6$). A primary particle moving along high magnetic fields radiates high energy photons which further give rise to a secondary pair plasma ($\gamma_p \sim 500$). The plasma instabilities developing in the secondary plasma is capable of

producing charge bunches in the inner magnetosphere. We believe the Inner Acceleration Region to be most appropriate for explaining the observed main pulse radio emission from normal pulsars and in the rest of this section we briefly explore the conditions leading to the generation of pair plasma in neutron stars (Ruderman & Sutherland 1975).

1.1.1 Pulsar Magnetosphere

The pulsar is characterized by its fast rotation periods (P) and large magnetic fields (B). A rotating magnetic dipole loses energy due to dipole radiation which is readily seen in radio pulsars as a gradual increase in its period. The slow down rate ($\dot{P}$) gives a direct estimate of the surface dipolar fields of neutron stars. The spindown power of the pulsar is given by:

$$\dot{E} = -I\Omega\dot{\Omega} = \frac{4\pi^2 I\dot{P}}{P^3} \tag{1.1}$$

Here $\Omega(=2\pi/\mathrm{P})$ is the angular velocity and $I(\sim 10^{45}$ g cm$^3)$ the moment of Inertia of the neutron star. The power due to dipole radiation on the other hand is given as (magnetic axis orthogonal to the rotation axis):

$$\dot{E} = \frac{B_d^2\Omega^4 R_S^6}{6c^3} \tag{1.2}$$

Here B_d corresponds to the dipolar component of the surface magnetic field and $R_S(\sim 10^6$ cm) is the radius of neutron star. The surface dipolar magnetic field can be obtained equating eq.(1.1) and eq.(1.2) as $B_d \simeq 3.2\times\ 10^{19}(P\dot{P})^{1/2}$ G. For a typical pulsar with period 1 sec and period derivative 10^{-15} sec/sec the surface dipolar field is 10^{12} G. The magnetic field near the stellar surface (B_s) however is highly multipolar with $B_s = bB_d$ and $b \gg 1$ (e.g. see Mitra et al. 1999b).

The presence of very high magnetic field ensures the existence of a charge separated magnetosphere around the neutron star satisfying the "force-free" condition (Goldreich & Julian 1969). In the context of the neutron star this implies that the electromagnetic forces overshadows the other inertial and dissipative forces. The rotating magnetic field gives rise to an electric field which in the observer's frame is

given as:

$$E = -\frac{(\Omega \times r) \times B}{c} \tag{1.3}$$

A charge separated magnetosphere is formed around the neutron star with the Goldreich-Julian density

$$n_{GJ} = \frac{1}{e}\nabla \cdot E = -\frac{\Omega \cdot B}{2\pi ce}\frac{1}{1-(\Omega \times r/c)^2} \tag{1.4}$$

The charges in the pulsar magnetosphere co-rotates with neutron star to ensure that the electric field is neutralized and the "force-free" condition ($E \cdot B = 0$) is maintained.

1.1.2 The Inner Vacuum Gap and outflowing plasma

The pulsar magnetosphere is divided into two distinct regions, the closed field line region with corotating charges and the open field line region above the polar regions. The open and closed field line regions are demarcated by the light cylinder ($R_{LC} = c/\Omega$). The charges flow out along the open field lines where the force free condition breaks down leaving behind a vacuum gap above the polar caps with large electric potential drop across it. This gap region called the Inner Vacuum Gap (IVG) undergoes periodic breakdown where charge particles are produced, accelerated and ultimately escape the pulsar magnetosphere into the surrounding medium. The IVG is fundamental to all electromagnetic radiation emitted from the pulsar as it is the primary source of moving charges.

The IVG is discharged by a cascade of pair production, which starts with a γ-ray photon interacting with the magnetic field producing an e^-e^+ pair and stops as the n_{GJ} charge density is attained. This process ultimately produces the singly charged, ultra relativistic primary particles beyond the IVG and takes place through the following steps: (i) The e^-e^+ pair is accelerated by the electric potential in opposite directions (The electric field ensures that only particles of single charges escape the IVG). (ii) The accelerated particles radiate further γ-ray photons via curvature radiation and/or inverse compton scattering. (iii) The γ-ray photons so produced give rise to further pairs which continue the process till n_{GJ} charge density is reached and the potential along the magnetic field line quenches. The gap height

stabilizes at the mean free path length of the γ-ray photons and is given by (Ruderman & Sutherland 1975):

$$h = 5 \times 10^3 \; b^{-4/7} \; P^{1/7} \dot{P}_{-15}^{-2/7} {\rho_6}^{2/7} \text{ cm} \tag{1.5}$$

Here $\rho_6 = \rho/10^6$ cm, where ρ is the radius of curvature of the highly multipolar magnetic field lines in the gap region. The maximum potential drop across the gap is given as:

$$\Delta V = \Omega B h^2/c \; \simeq \; 5 \times 10^9 \; b^{-1/7} P^{-3/14} \dot{P}_{-15}^{-1/14} {\rho_6}^{4/7} \;\; \text{Volts} \tag{1.6}$$

The 'Sparking' model proposed by Gil & Sendyk (2000) postulate that the discharge in the IVG is carried out via a series of sparks of lateral dimension $\sim h$, the height of the gap. The mean separation between the sparks is also of similar size, i.e h. The maximum energy the primary particles can attain for typical pulsar parameters (i.e. $P = 1$ sec; $\dot{P} = 10^{-15}$ sec/sec; $\rho = 10^6$ cm) is $\gamma_b = e\Delta V/mc^2 \sim 3{\times}10^6$.

Once the primary particles escape the IVG the electric potential drop vanishes stopping further acceleration but they keep on emitting γ-ray photons either due to curvature radiation, with characteristic frequencies $\hbar\omega_c = \frac{3}{2}\gamma_b^3 \hbar c/\rho$, or resonant and nonresonant inverse compton scattering (Medin & Lai 2010). The photons continue pair production resulting in a cloud of secondary $e^- e^+$ plasma with typical energies $\gamma_p = \hbar\omega_c/2mc^2 \sim 10$ - 1000 and density $n_p = \chi n_{GJ}$, where $\chi \sim 10^4$ is the Sturrock multiplicative factor (Sturrock 1971). The periodic breakdown of the IVG results in a series of secondary plasma clouds with a wide spread in energy, moving outward along the open magnetic field lines. The sparks in the IVG undergo a $E \times B$ drift due to the presence of the uncanceled electric fields. The $E \times B$ drifting is believed to be responsible for the well known phenomenon of subpulse drifting seen in certain pulsars. In order to explain the slower subpulse drift rates compared to the purely vacuum gap case, as seen in some pulsars, Gil et al. (2003) have proposed a modification to the IVG model by introducing the concept of Partially Screened Gap (PSG). According to the PSG model the electric potential in the Vacuum Gap in certain instances is partially screened by charged particles and ions escaping from the stellar surface as the polar regions gets heated up by a continuous bombardment of back flowing particles. In

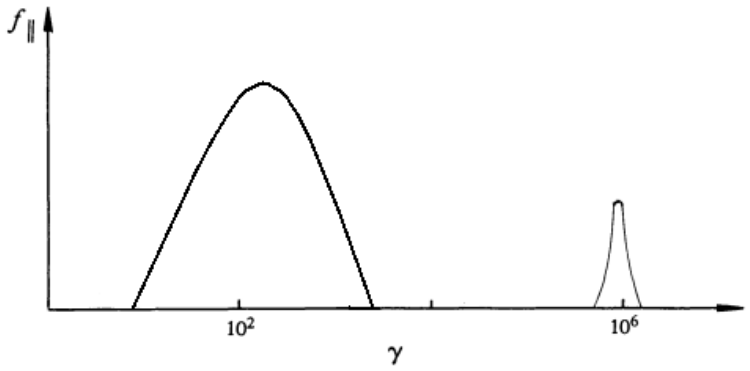

Figure 1.1 The figure shows the energy distribution function of the outflowing plasma in the pulsar magnetosphere (Goldreich & Julian 1969; Sturrock 1971; Ruderman & Sutherland 1975). The plasma consists of two principal components, the primary plasma, $\gamma_b \sim 10^6$ with a narrow spread in energies, and a secondary plasma, $\gamma_p \sim 10^2$ with a much wider spread in energies.

such a scenario the maximum energy of the primary particles would be lower due to the reduced electric potential across the gap and inverse compton scattering effects are expected to be more dominant. In most cases the screening effect would vary with time depending on the heating of the polar surface.

The relativistic plasma produced as a result of the periodic breakdown of the IVG is fundamental to the production of radio emission in pulsars and has certain unique characteristics. A rough overview of the plasma energy distribution function is represented in figure 1.1. The plasma is nonstationary, multi component, one dimensional and overlapping. The nonstationary nature, in contrast to a uniform supply of plasma, results from the periodic breakdown of IVG leading to a discharge for a few tens of microseconds which subsequently produces the primary and secondary clouds. The process stops for a few tens of nanoseconds while the gap potential builds up before the next discharge begins. This further leads to overlapping clouds of plasma where the higher energy particles of the plasma cloud in the rear catches up with the

slower particles of the plasma cloud above it and is very important for generating instabilities which can lead to coherent radiation. The high value of the magnetic fields in the pulsar magnetosphere further ensures a one dimensional plasma flow, closely following the magnetic field lines, with any perpendicular component of the energy dissipating fast. In summary the open field line region consists of certain field lines where a 'spark' develops in the IVG which give rise to clouds of outstreaming, dense, overlapping secondary $e^{-}e^{+}$ plasma penetrated by highly energetic singly charged primary particles.

1.2 Origin of Coherent Radio Emission

The basic ingredient for the development of coherent radio emission is a stream of overlapping clouds of relativistic plasma, with a relatively wide energy distribution, moving along dipolar magnetic field. The multipolar components decay faster and only the dipolar components are prominent beyond the vacuum gap. The coherent emission can arise due to the growth of plasma instabilities in the outflowing plasma. There are two prominent sites in the pulsar magnetosphere where such instabilities may develop due to various physical processes. In this section we briefly explore the likely conditions which may lead to coherent radio emission in pulsar magnetosphere.

1.2.1 Emission mechanism in inner magnetosphere

One popular model for radio emission in normal pulsars has been the concept of charge bunching exciting coherent curvature emission at heights of $50R_S$ ($\sim 10^9$ cm). At observed radio frequencies ($\sim$ 1 GHz) $\gamma_p \sim 500$ particles are required at these heights for curvature radiation. A possible mechanism for charge bunching was suggested by Ruderman & Sutherland (1975) to be the two stream instability. The secondary pair plasma would undergo bunching by its collective coulomb interaction with the surviving primary particles ($\gamma_b \sim 10^6$). However, detailed studies revealed that the above mechanism is inefficient for bunch formation as the growth rate of the instability is inadequate (Ursov & Usov 1987). In recent years the bunching model have been

improved utilizing the inherent nonstationarity in the outflowing plasma. The charge bunching leading to formation of relativistic solitons have been proposed as a possible mechanism for radio emission (Melikidze et al. 2000; Gil et al. 2004). The overlapping particles of different energies from successive clouds of secondary plasma give rise to strong Langmuir oscillations which is the only instability that develops at these heights. The Langmuir oscillations so developed are longitudinal, electrostatic waves which are still unable to account for the observed radio emission. The Langmuir waves are modulationally unstable and their nonlinear evolution give rise to plasma solitons with characteristic length$\sim$ 30 cm. The secondary e^-e^+ pair plasma as they propagate along open field lines undergo a relative energy separation ($\Delta\gamma = |\gamma^+ - \gamma^-|$) in order to maintain the 'force-free' condition ($E \cdot B = 0$). In the case when $\Delta\gamma$ is large (i.e $\Delta\gamma/\gamma_p \sim 1$), e.g. in presence of highly nondipolar fields in IVG, the resultant relativistic mass difference between the two induce the pondermotive forces to act on the two charged species at different rates. This cause charge separation within a soliton which is however electrically neutral with zero total charge. The charge density of the solition is $n_s \sim 10 n_{GJ}$. Using the characteristic length of solitons and the 'Spark' area ($S_\perp = \pi(h/2)^2(R/R_S)^3 \sim 3\times10^{12}$ cm^2) translated to emission heights, an estimated $\sim 10^{21}$ charges are expected to be present in a soliton. The charge separated solitons moving along the dipolar magnetic fields emits coherent curvature radiation (soliton length scales $\leq$ wavelength of radio waves, ensuring coherent nature). There are approximately 10^5 solitons associated with each 'Spark' and about 25 such 'Sparks' in the IVG. The total power emitted from the pulsar is an incoherent combination of all these sub elements with the basic unit, the charge separated soliton, emitting coherent curvature radiation.

1.2.2 Emission mechanism in outer magnetosphere

In the IVG model, resulting in dense overlapping clouds of secondary plasma penetrated by highly energetic primary particles, there is a possibility of generating coherent radio emission in the outer magnetosphere near the light cylinder. The emission mechanism first proposed by Kazbegi et al. (1987, 1991) gives rise to radio emission

via the resonant interaction of the plasma waves in the secondary plasma with the drifting primary particles. The emission mechanism known as the cyclotron resonance instability in relativistic plasma which leads to the cyclotron maser emission has been proposed as a feasible mechanism for generating coherent emission at low radio frequencies in many astrophysical systems. The emission mechanism works in plasma systems where excess free energy in the particle distribution is unable to dissipate internally. The excess energy is directly emitted as electromagnetic radiation through a mechanism of negative absorption in the plasma equivalent to a maser like emission. The cyclotron resonance instability is expected to be the source of radio emission in a large number of space plasma and astrophysical systems like the auroral kilometric radiation of Earth, the auroral emission in Jupiter, Saturn and exoplanets, spikes in radio emission from the Sun and stars at low radio frequencies, coherent radiation from Blazar jets, and so on (Treumann 2006).

As previously mentioned the neutron star is characterized by a strong magnetic field, especially near the surface which makes the plasma flow one dimensional along the field lines (as any velocity component perpendicular to the field is damped out by emitting synchrotron radiation). This condition is however relaxed near the light cylinder where the magnetic fields have decreased sufficiently ($B_R = B_d(R_S/R)^3$) to allow drift across it. The outflowing secondary plasma harbours various electromagnetic modes which are capable of escaping the plasma boundary. A certain mode in the secondary plasma may undergo resonant interaction with the drifting primary particles. If the growth rate of this mode is sufficient they would escape the plasma boundary as coherent radio emission.

This emission mechanism is of particular interest in the context of this thesis and a detailed analysis have been carried out regarding its applicability to pulsars in chapter 4.

1.3 Observational bounds

There is a wealth of observational results in the literature which have revealed great insights about the radio emission from pulsars. Some of these observational proper-

ties help discriminate between various physical models explaining the origin of radio emission while others are still outside the bounds of our current understanding. In this section we look at a few observational results that are key in identifying the radio emission mechanism within the physical picture presented earlier. We also briefly explore certain observational features that lie outside the purview of the emission mechanism so identified and motivate the work presented in this thesis.

1.3.1 Shape of Main Pulse and Emission Heights

The radio emission from pulsars is highly beamed and exhibit high degree of polarization. The observed emission is a complex function of the inherent orientation (the angle between magnetic and rotation axis) of the pulsar and the observers line of sight geometry. The average pulsar profiles (obtained after averaging several thousand periods) show the presence of a main pulse which occupies about 5–10% of the pulsar period (although the extent depends on geometry) and in most cases the remainder of the profile appear to be radio quiet. The main pulse show a high level of linear polarization with some circular polarization also being present. The Polarization Position Angle (PPA) show a S-shaped swing across the main pulse which is in excellent agreement with the Rotating Vector Model (RVM) proposed by Radhakrishnan & Cooke (1969) and underlines the dipolar nature of magnetic field at the emission region.

The main pulse emission has a complex morphology which exhibit a frequency evolution. A number of studies involving many normal pulsars have helped uncover the underlying structure and location of the main pulse emission. The main pulse is made up of one or more pulsed components known as subpulses. The subpulses show slow drifting phenomenon and their width scales with period as $2.4^{\circ}P^{-1/2}$ (Rankin 1990; Maciesiak et al. 2012). The origin of subpulses and the overall morphology of the main pulse have been explained in the context of the 'Sparking' model presented in section 1.1 and the dipolar geometry. The main pulse emission can be decomposed into a core emission occupying the central field lines surrounded by two or more nested cones (Rankin 1993a; Mitra & Deshpande 1999). The core and the conal regions are

populated by sparks where each spark give rise to radio emission at the emission height in the form of a subpulse. The conal emission exhibit modulation and drifting due to slow $E \times B$ drift of the sparks, which cause the subpulses to circulate around the cone. The morphology of the observed emission will depend on whether the line of sight cuts the emission cone centrally (core emission with/without outriding conal components) or in a tangential manner (conal double profiles). The frequency evolution of the morphology is accounted for by recognizing the fact that radio emission at different frequencies originate at different heights with lower frequency emission originating at a higher altitude resulting in a different cut to the emission cone by the line of sight and usually an increase in the pulse width with decreasing frequency. Using the dipolar geometry an estimate of the emission height at 1 GHz is given as (Kijak & Gil 1997):

$$r_G = 10 \left(\frac{\theta}{1.23^\circ} \right)^2 P \quad \text{km} \tag{1.7}$$

Here the opening angle θ, the angle between the magnetic axis and the tangent to the outermost open field line, is determined from the line of sight geometry and the observed width of the main pulse. Solving for the geometry of the pulsar (angle between magnetic and rotation axis α, and opening angle β, the minimum angle between the observer's line of sight and magnetic axis) and using the measured width of the observed main pulse the emission height have been measured to be (Kijak & Gil 2003)

$$r_G = (400 \pm 80)\ \nu_{GHz}^{-0.26 \pm 0.09}\ \dot{P}_{-15}^{0.07 \pm 0.03}\ P^{0.30 \pm 0.05} \quad \text{km} \tag{1.8}$$

The height of the main pulse emission can also be independently determined by considering the effects of aberration/retardation (A/R) which will shift the emission with respect to the central field line depending on the emission height (Gangadhara 2005; Blaskiewicz et al. 1991). The aberration in the pulsar profile is a result of the rotation of the pulsar which gives rise to a perpendicular component of the velocity causing a relative shift in the observed emission position while retardation arises due to the slightly different path lengths the emission from different parts of the pulsar profile has to cover in order to reach the observer. The emission altitude using the

A/R effect is given as (Dyks et al. 2004):

$$r_{AR} = -\frac{\Delta\phi}{2}\frac{2\pi}{360^\circ}\ R_{LC} \tag{1.9}$$

Here $\Delta\phi$ is the shift in the profile due to the A/R effect which can be determined in a variety of ways (see Mitra & Li 2004, for a discussion of the different methods used). The emission height in this case turns out to be $r_{AR} \leq r_G$ (Krzeszowski et al. 2009). This method suffers from uncertainty in identifying a fiducial point for the central phase with the emission height estimates representing a lower limit. A detailed calculation for the phase shift due to A/R effect including shift due to polar cap current is carried out in Gangadhara (2005).

The estimates of the emission heights using various independent techniques reveal that the main pulse emission originate in the inner magnetosphere around $50R_S$. This indicates that the relativistic charge separated soliton discussed in section 1.2.1, originating within the framework of IVG, is a likely candidate for main pulse emission in normal pulsars.

1.3.2 Emission outside Main Pulse

In the vast majority of pulsars the region outside the main pulse do not show any pulsed emission component. In special cases, when the magnetic axis is perpendicular to the rotation axis, the emission from the other pole is observed in the profile at approximately 180° away from the main pulse as an interpulse emission (Hankins & Fowler 1986). The interpulse emission is accommodated within the purview of the emission mechanism explaining the main pulse, being its counterpart from the opposite pole. However a few pulsars show the presence of a pre/post cursor (PPC) component preceding/succeeding the main pulse emission. These PPC components are usually connected to the main pulse via a bridge emission and exhibit a high degree of linear polarization. In the model explaining the pulsar emission with the radio emission originating along dipolar field lines, the PPC emission lies outside the region where the instability condition, viz. the charge separated solitons, giving rise to the main pulse emission can develop and as such their origin is hitherto unexplained.

There have been a few studies (Backus et al. 2010) where the detection of the PPC components have been reported but no systematic studies have been conducted to characterize their basic properties. In the course of this thesis we have made an attempt to compile the nature and characteristics of the PPC emission given its importance in uncovering a new location of radio emission from pulsars. A detailed study is reported in chapter 5 detailing the basic results obtained in this context.

1.4 'Off-Pulse' emission: Historical overview

In this chapter we have presented a physical picture of the pulsar magnetosphere and the conditions leading to radio emission in normal pulsars under certain assumptions. We have briefly delved into some emission mechanisms that can give rise to coherent radio emission in section 1.2 and found out two regions in the pulsar magnetosphere where coherent emission can arise, in the inner magnetosphere and nearer to the light cylinder respectively. The main pulse emission in pulsars originates in the inner magnetosphere which highlights the first mechanism explained in section 1.2.1, viz. curvature radiation due to charge separated solitons, as a likely candidate for its origin. However, the second emission mechanism discussed in section 1.2.2, the cyclotron resonance instability, is also a natural outcome of the framework of IVG responsible for the soliton model leading to main pulse emission. Any emission originating in the outer magnetosphere is expected to be away from the main pulse and would likely spread out in longitude due to the larger opening angle of the field lines higher up. The major motivation of this thesis is to look for observational signatures of radio emission outside the main pulse as a natural consequence of its origin in the outer magnetosphere of normal pulsars.

The other possible source of off-pulse emission is the interstellar medium (ISM) around the pulsar. As described before the pulsar loses most of its rotational energy in the form of an outflowing relativistic plasma wind which, when confined by the surroundings, may form a pulsar wind nebula (PWN). Several types of PWNe are formed depending on the confinement mechanism. Young and energetic pulsars are often located in their associated supernova remnant (SNR). The pulsar wind stream-

ing into the ambient medium produces standing shocks resulting in a plerionic PWN (like the one observed in the Crab nebula). In older pulsars, where the surrounding SNR is likely to be dissipated, the relativistic particles may interact with the ISM magnetic field and radiate, creating ghost remnants (proposed by Blandford et al. (1973), but not observed till date). Finally, a pulsar moving through the ISM with supersonic speed can produce a bow-shock nebula, where ram pressure balance is established between the pulsar wind and the ambient medium. Several such bow shock nebulae have been detected in Hα, and some in the radio as plerionic bow shocks, but never in both (see Chatterjee & Cordes (2002) for a detailed study). Several searches for PWNe have been conducted in the past with varying sensitivities and resolutions. However, only in about 10 young pulsars have radio emission been detected outside the main-pulse and all of these are believed to be associated with PWNe. In all such cases the associated pulsars are young (10^3–10^5 yr), have high spin-down luminosities ($\dot{E} \geq 10^{35}$ erg s^{-1}) and all except one are associated with SNRs (Gaensler et al. 1998, 2000; Stappers et al. 1999). It is believed that the pulsar wind and the environment change as pulsars slow down and age, making them less likely to harbour PWNe.

The standard pulsar observations geared for detecting pulsed temporal emission components would be inadequate for detecting a low level baseline emission as the baseline value is uncertain. We would require interferometric studies aimed at detecting low-level emission where the baseline noise floor is around zero in the absence of any emission. However a special technique of 'Gated Interferometry' would be required for our purpose in order to separate the much brighter main pulse which would otherwise corrupt the faint emission, if any, in the off-phase of the pulsar.

We have conducted a literature survey yielding many reports of searches for 'off-pulse' emission from pulsars (see Table 1.1). Perry & Lyne (1985) reported off-pulse emission from 4 pulsars (PSRs B1541+09, B1604–00, B1929+10 and B2016+28) using a gated two-element interferometer at 408 MHz. Subsequent studies showed that two of these pulsars, B1541+09 and B1929+10, were aligned rotators, undermining the claim of off-pulse origin (Hankins et al. 1993; Rathnasree & Rankin 1995). The off-pulse emission in the other two pulsars, B1604–00 and B2016+28, were later identified with unrelated background sources (Strom & Van Someren Greve 1990; Hankins et al.

Table 1.1 Literature survey for off-pulse studies.

Non detections/ subsequent SNR	Detections later refuted	Tentative detection	PWNe detection
1. Schönhardt (1973, 1974)	1. Gopal-Krishna (1978)	1. Gaensler et al. (2000)^G	1. Frail & Kulkarni (1991)
2. Weiler et al. (1974)	2. Glushak et al. (1981)		2. Frail et al. (1996)
3. Cohen et al. (1983)	3. Perry & Lyne (1985)^G		3. Gaensler et al. (1998)
4. Bartel et al. (1985)^G			4. Giacani et al. (2001)
5. Strom & Van Someren Greve (1990)^G			
6. Hankins & Rickett (1975)^G			
7. Frail & Scharringhausen (1997)			
8. Stappers et al. (1999)^G			

The gated interferometry studies in Table 1.1 have been indicated with ^{G}.

1993). Bartel et al. (1985) reported a non-detection from PSR B0329+54 using gated VLBI interferometry at 2.3 GHz. Strom & Van Someren Greve (1990) reported non-detections in 43 pulsars using the WSRT in gated mode at 327 and 609 MHz. Stappers et al. (1999) reported non-detection in 4 pulsars using ATCA in gated interferometric mode at 1.3 and 2.2 GHz. Gaensler et al. (2000) searched for unpulsed emission from 27 energetic and/or high velocity pulsars using gating interferometry with the VLA and ATCA at 1.4 GHz and found emission in two cases. However they could not conclusively determine whether these detections corresponded to PWNe or the pulsar magnetosphere; they even suggested that the detections could be spurious and a result of improper online gating. There have been detections of several radio pulsars with associated plerionic bow shock nebula: B1951+32 (Hester & Kulkarni 1988), B1757–24 (Frail & Kulkarni 1991), B1853+01 (Frail et al. 1996) and B1643–43 (Giacani et al. 2001). All of these are highly energetic pulsars associated with SNR (Chatterjee & Cordes 2002). Gaensler et al. (1998) reported the detection of off-pulse emission from PSR B0906–49, which appears to be a PWN generated by

a slow moving pulsar in the dense ISM. None of the studies carried out in the past have succeeded in unambiguous detection of magnetospheric 'off-pulse' emission from pulsars.

The main emphasis of this thesis is to unravel and understand the nature of off-pulse emission from long period pulsars.

Chapter 2

Offline-Gating

2.1 Pulsar Observations: A brief overview

The traditional techniques for detecting radio emission from pulsars usually employ a single dish (e.g. Arecibo, Effelsberg Radio Telescope) or a phased array with multiple antenna elements operating in phase (e.g. Giant Meterwave Radio Telescope). As mentioned in chapter 1 pulsars emit bursts of radio emission or narrow pulses at low radio frequencies which stand out as temporal structures above the baseline level. This is a very different behaviour from other conventional sources which are assumed to be inherently time invariant. In order to decipher the temporal nature of pulsar emission the observations need to be carried out with high time resolutions. In addition these temporal structures exhibit various degrees of polarization with very high linear polarization and significant circular polarization in certain cases. In order to ascertain the polarization characteristics polarized receivers are used and equivalent data for the four Stokes parameters are also recorded. As the pulsed emission propagates through the Inter Stellar Medium (ISM) on its way to the observer it undergoes dispersion, i.e different effective path lengths at different frequencies. The time difference of the signal at two different frequencies ν_1 and ν_2 is given as:

$$t_{12} \simeq 4.149 \times 10^3 DM \left(\frac{1}{\nu_1^2} - \frac{1}{\nu_2^2} \right) \quad \text{sec} \tag{2.1}$$

Here DM $(=\int n_e dl)$ the dispersion measure of the pulsar, expressed in units of cm^{-3} pc, depends on the ISM electron density and distance to the pulsar; the frequencies are expressed in units of MHz. In order to prevent smearing of the signal while averaging over a finite bandwidth (to improve signal to noise) techniques of coherent and incoherent dedispersion are employed. The incoherent dedispersion leads to the frequency band being broken into smaller channels with time corrections applied to each channel, while the coherent dedispersion deals with signals being sampled at time resolutions of inverse of twice the bandwidth and dispersion corrected before further processing. The conventional techniques described above are ideally suited for studying the main pulse emission. However, they fall short in addressing the presence of continuum emission at the baseline level which depend on the background sky emission and receiver system noise which usually show considerable fluctuations.

2.2 Interferometric Studies

2.2.1 Basics of Imaging

A two element interferometer measures the visibility function, which is the fourier transform of the Intensity of a relevant part of the sky, with a angular scale inversely proportional to the separation between the two antennas (Thompson et al. 1986).

$$V(u,v) = \int_{-\infty}^{\infty}\int_{-\infty}^{\infty} A(l,m)I(l,m)e^{-2\pi i(ul+vm+w\sqrt{1-l^2-m^2})}\frac{dl\ dm}{\sqrt{1-l^2-m^2}} \qquad (2.2)$$

In the above equation $V(u,v)$ is the visibility measured with a single baseline (a two element set) and u, v and w are the spatial co-ordinates of the baseline in the interferometer plane known as the uv-plane, measured in units of λ the wavelength of observation. $A(l,m)$ and $I(l,m)$ are the antenna response and the Intensity, respectively, at the two dimensional angular position l and m of the sky, measured in units of radians, with respect to the field center. When a large number of visibilities, with information of various angular scales and distances, are available a two dimensional intensity map can be constructed by inverse fourier transform of eq.(2.2). A multi element interferometer reproduces an image of the sky by utilizing the principle of

aperture synthesis. An array of antennas are placed at various distances from each other, in order to sample different angular scales, and taking into account that as the earth rotates the baseline moves in the uv-plane registering different measurements of visibility. Thus a sufficient number of visibilities can be recorded if the observations are carried out for a long enough duration and an intensity map of the desired part of the sky can be reproduced.

2.2.2 Requirements for 'off-pulse' Studies

The principle of interferometry works under the assumption that the sources in the sky are statistically time invariant and remains unchanged throughout the observation time. This makes these techniques inadequate for studying the temporal nature of pulsed emission from pulsars. However the interferometric technique has the following advantages:

1. An imaging interferometer is insensitive to constant flux density background along the spatial axes while a standard pulsar receiver is usually insensitive to the constant background along the time axis; the detection of off-pulse emission is essentially an attempt to find such a constant background along the time axis.

2. Self-calibration of interferometric data can correct instrumental and atmospheric gain fluctuations on very short time scales. The corrections are determined by the flux densities of the constant and bright background sources in the field and hence would not be affected by the pulse variation of the relatively weak pulsar.

3. The higher spatial resolution of an interferometer greatly reduces the coincidence of nearby unrelated sources; thereby reducing the probability that the off-pulse emission is from an unresolved background source.

Thus the Interferometric technique would be ideal to search for faint emission in the 'off-phase' of pulsars provided the 'on-pulse' contribution is masked. This requires the technique of 'Gated-Interferometry' as discussed in chapter 1. We have developed the technique of 'Offline-Gating' to search for off-pulse emission in normal, long period pulsars.

2.3 Gating Technique

The Giant Meterwave Radio Telescope (GMRT) used for our experiments is an aperture-synthesis radio interferometer located near Pune, India (Swarup et al. 1991). The telescope consists of 30 dishes of 45 m diameter with a maximum baseline length of 27 km and operates at 6 frequency bands between 50 and 1450 MHz. In our present studies we have used the 325 MHz and 610 MHz bands both of which operated with a bandwidth of 16 MHz. The GMRT in the interferometric mode is capable of high time resolution data with 128/256 msec modes. During the course of our studies the GMRT correlator system have been upgraded from a Hardware system (GHB) to a Software backend (GSB). The data for the initial part of our work were recorded with the GHB whose 128 msec mode had an average integration time of 131 milliseconds while the 256 msec mode operated with a time sampling of 261 milliseconds. The GSB initially operated at 256 msec mode with average integration time of 251 milliseconds, but was later extended to the 128 msec mode with average integration time of 125 milliseconds. The integration times in all the modes showed a narrow spread around the average values (see figure 2.9). We recorded data where two circular polarizations RR and LL were present and the frequency band was spanned by 32–256 channels. Each time sample of the recorded data consisted of 435 baseline visibilities and 30 auto correlation data, i.e. 465 records for each polarization and frequency channel. In standard observations the data is further averaged over several seconds (2–16 sec) before recording in contrast to our high time sampling rates.

Several earlier studies (see for e.g. Strom & Van Someren Greve (1990); Stappers et al. (1999)) have utilized the technique of online gating to separate the on and off-pulse regions based on pulsar timing information, and they accumulated time averaged on and off-pulse data. The advantage of these methods include the relatively shorter size of files to handle and hence shorter computation time (a major factor at the times the studies were done). The disadvantage is the impossibility of rectifying any errors during the gating process (see the results and discussions in Gaensler et al. (2000)). In order to separate the on and off-pulse regions it is important to identify their phases. This was initially achieved by folding the auto correlation data with

the known periodicity of the pulsar studied. The phases once identified were used to separate the cross correlated data (visibilities) into two separate files containing the on and off-pulse respectively. The two files were imaged separately by conventional imaging techniques to search for any off-pulse emission at the location of the on-pulse. The details of the analysis are discussed below.

2.3.1 Data Format

The radio interferometric data is recorded in a special data format called the Flexible Image Transport System (FITS). The GMRT data is stored in the form of a primary Header Data Unit (HDU) which consists of an ascii header followed by binary data. The header file contains information about the data such as date of observation, the name and position of source, the classification of records in the binary array, etc. The data unit consists of a series of binary numbers which can be classified into two parts, the parameter array and the image array. The parameter array contains information like time of record, the baseline identifier, the u, v and w value of the baseline, source identifier etc. The image array records the complex visibility (in the form of Real, Imaginary and weight) for each basic unit of polarization, channel, baseline, time (in the same order). In addition to the primary HDU the FITS file also contains certain 'extensions' in the form of FQ file (containing frequency information), CL file (containing antenna calibration information), AN file (containing parameters of individual antennas), etc. The FITS file can be manipulated using c codes with the help of specialized library 'cfitsio' which is an open source software freely available at: http://heasarc.gsfc.nasa.gov/. There are several functions in 'cfitsio' library for reading and modifying the FITS files and these were extensively used in the softwares developed for our analysis.

2.3.2 Folding

In order to find the on and off-pulse regions of the pulsar the conventional approach is folding the data. Folding is the process of wrapping around, aligning the phases (so that the on-pulse lines up in the same bins) and averaging the data in time bins to

find the time location of the on-pulse (which emerges above the baseline noise level) and the off-pulse regions within the pulsar period. The pulsar period varies with time and the period on the day of observation was estimated using the open source software 'Tempo' which is freely available at: http://tempo.sourceforge.net/.

In the course of these analysis we resorted to folding the auto-correlation data to determine the temporal positions of the on and off-pulse regions. However, the data suffered from certain irregularities like instrumental gain variations with time, the fluctuations in the frequency band and in certain instances the presence of Radio Frequency Interference (RFI). We have carried out a detailed analysis to rectify these inconsistencies using specially developed software which is summed up in the following steps:

1. Each individual antenna was processed separately with the first step being the determination of a bandshape. For each time record and polarization the representative number was determined by determining the median of the channels and scaling this value to a fixed level. The other channels were scaled accordingly (by the ratio between the fixed level and the representative value). This time normalization will wash away all temporal variations including the on-pulse behaviour. In order to determine the variation across channels, the median value across time for each channel was determined which after normalization gives the bandpass calibration. The time normalizations were reverted back to recover the temporal variations, including the pulsed nature. The band shape for each polarization for one such antenna is shown in figure 2.1.

2. The self data for each polarization after applying bandpass calibration was averaged across the channels and the average data was checked for deviant points using median absolute deviation (MAD) over many periods. The outliers above the 3σ were clipped before further analysis and the data now was channel averaged outlier free, but still with the fluctuations across time. The state of the data at these stage is shown in figure 2.2.

3. In order to correct for the temporal variations in the data the running mean was determined (see figure 2.2) over time intervals of several times the pulsar period (so that the pulsed nature is not compromised) and subtracted from the data. The

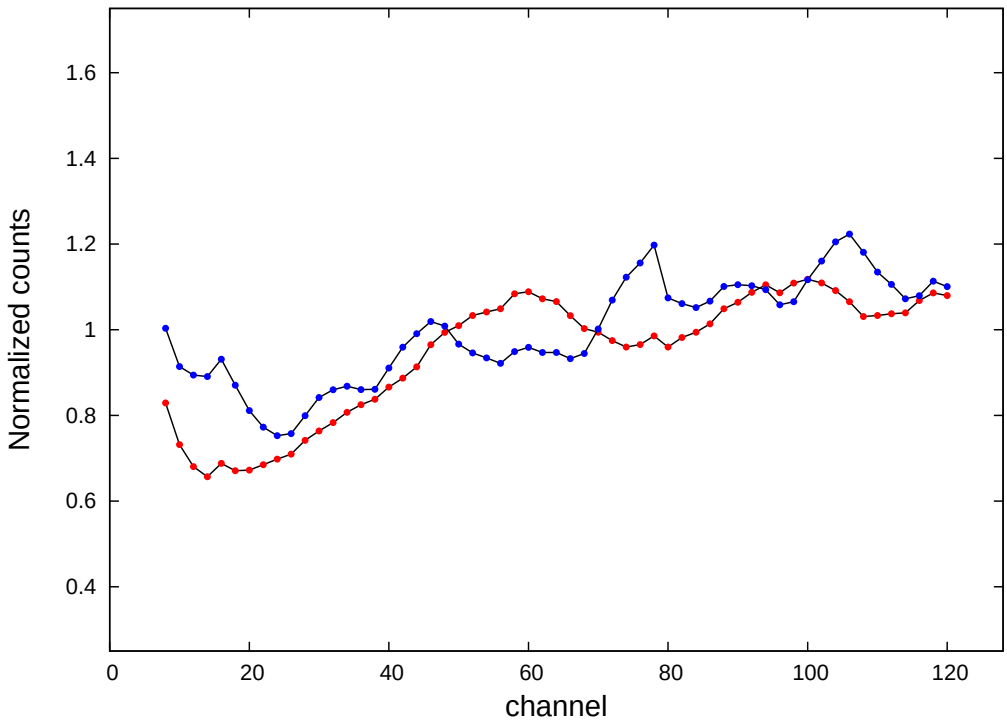

Figure 2.1 The figure shows the frequency band shape for the polarization RR (red) and LL (blue) for a single antenna for 128 channels with the first and last 8 channels not included in analysis. The steps for determination of the bandshape have been detailed in the text. Each channel for this antenna was divided by the value in the band to correct for band variation.

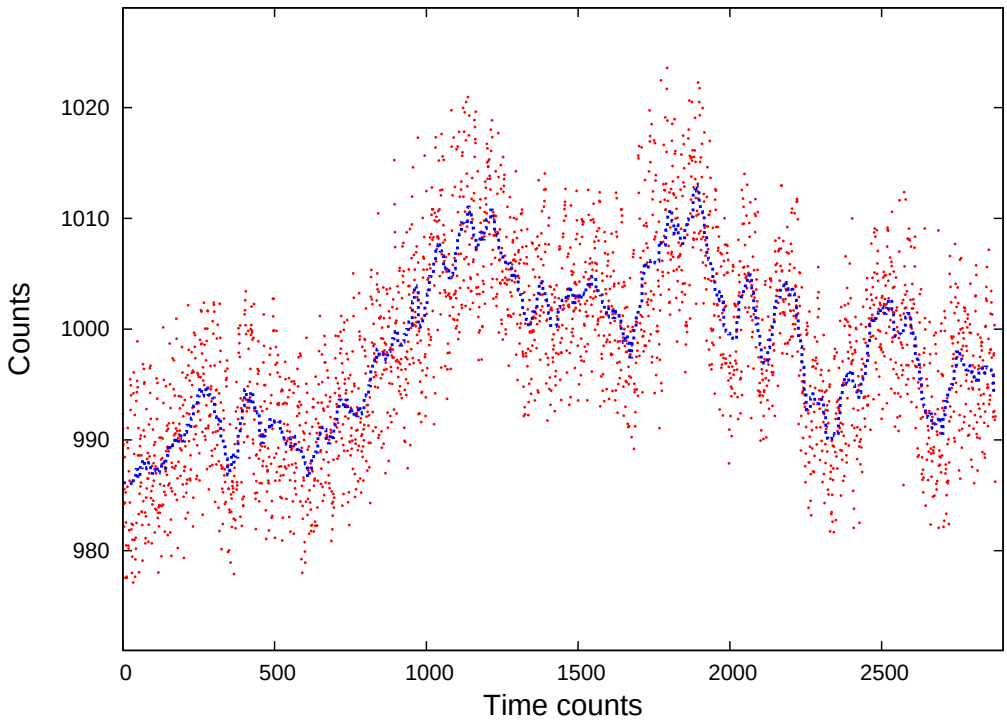

Figure 2.2 The figure shows the time variation in the data averaged across channels, after correcting for the band, for a single polarization. The running mean of the data over a timescale much larger than the periodicity of the pulsar is also shown (in blue).

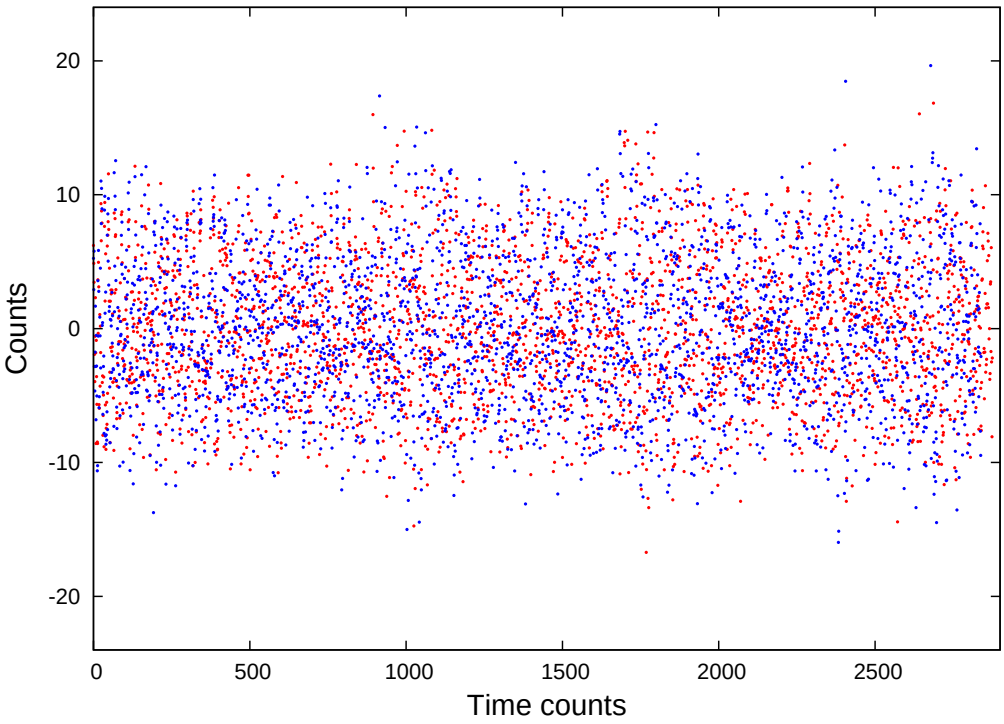

Figure 2.3 The figure represents the time series for a single antenna with two polarizations RR (red) and LL (blue). The data is averaged across frequencies, after correcting for band variations and time fluctuations after running mean subtraction. All outlier points have also been removed. This data is used for folding to determine the On and Off state of the pulsar.

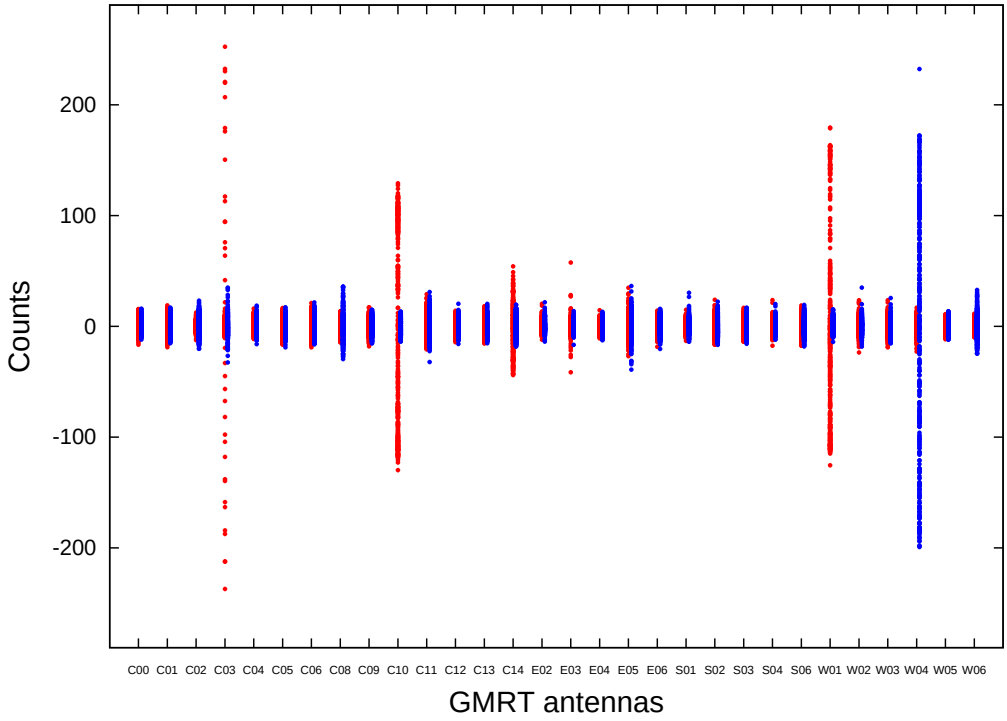

Figure 2.4 The figure shows the spread in the auto-correlation data for the all the 30 GMRT antennas recorded during an observing session. Each antenna have been corrected for the variations in the frequency band and time for each of the polarizations RR (red) and LL (blue).

data so corrected, shown in figure 2.3, is freed of all outliers and variations due to systematics and used for further analysis.

4. The above steps are repeated for each antenna to determine a time series data. It was found that certain antennas showed large variations after all the corrections (see figure 2.4) and were not used for folding. The selected antennas were folded together to determine the profile of the pulsar. The number of bins to fold the data was determined from the periodicity of the pulsar and the time resolution of observation. Examples of a folded profile for the pulsars B0525+21 and B2045–16 are shown in figure 2.5.

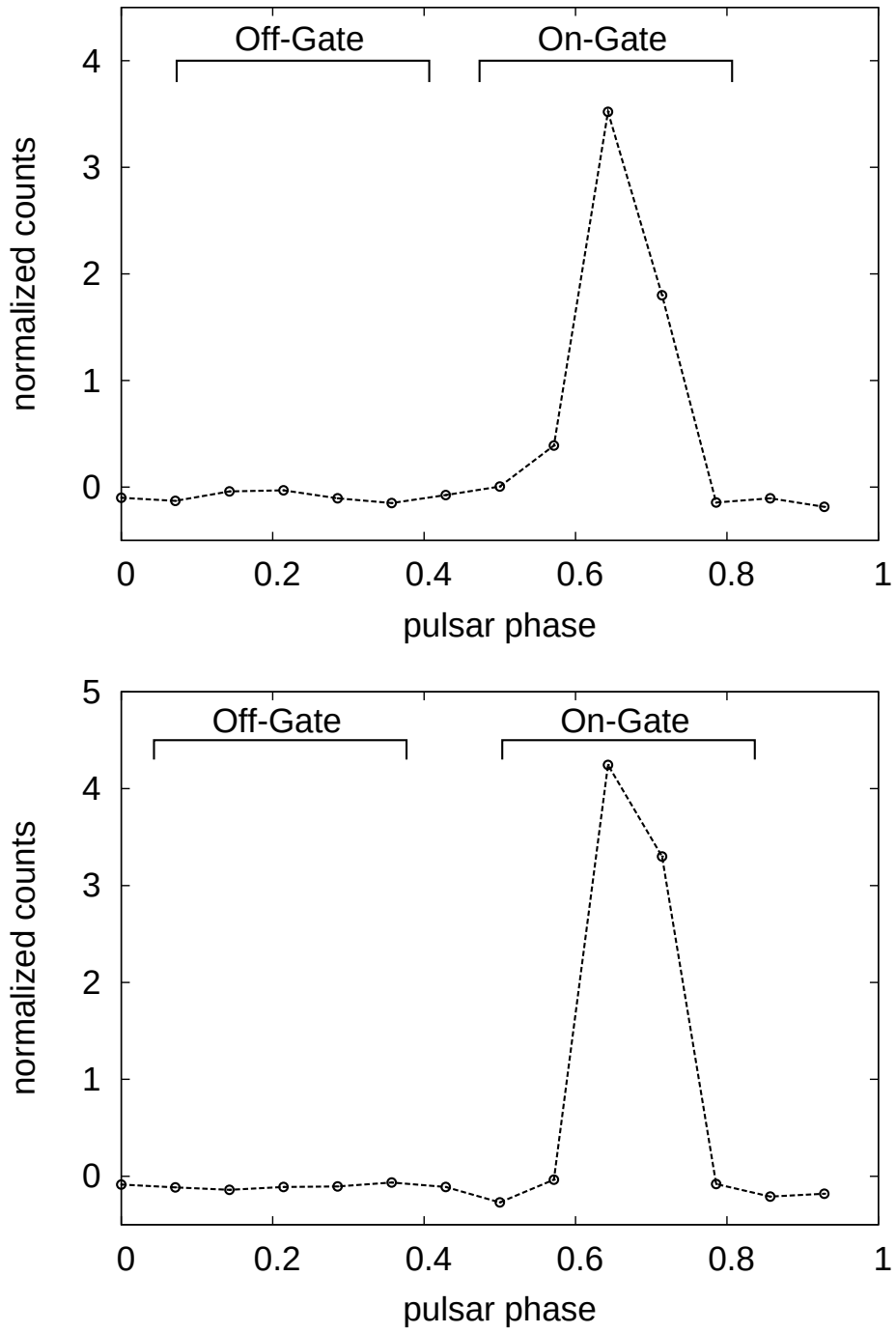

Figure 2.5 The folded profile of pulsar B0525+21 (top) using 256 msec mode of GHB and B2045–16 (bottom) using 128 msec mode of GHB at 325 MHz demonstrating the on and off-pulse regions. The phases of the on-pulse and off-pulse gates are also shown.

2.3.3 Gating

The folding process described above yielded the phase (fractional period) of the on-pulse and off-pulse region for the pulsar to be investigated. It is possible to associate a phase value to each of the time records. Thus the process of 'Gating', where we intend to separate the on and off-pulse regions from the cross-correlated data (visibilities), would involve identifying the specific phases for each time and handling them accordingly. We exploited certain features of the recorded data in FITS format to execute the 'Gating' process. Firstly, the time values associated with the auto correlation data is same as the values associated with the cross correlated data. This ensures that the folding process using the auto correlation data, which was used due to its higher counts compared to the self data, can be seamlessly used to determine the phases of the cross correlated data. Secondly, the non essential parts of the file can be effectively removed by replacing the visibilities with zeros, i.e. replacing the Real, Imaginary and weights with zeros. The 'Gating' process was accomplished using specially designed c codes which worked as follows.

1. The cross correlated data were expected to have instances of RFI and the outlier visibilities were edited out by calculating the running mean and rms around each time and clipping them if they were outside the 3σ level. The data editing was applied looking at real, imaginary and amplitude part of the visibilities for each baseline, polarization and frequency channel separately.

2. The central on and off phases for each dataset were identified from the folded profiles. The number of points around the central phase to be averaged were also determined keeping in mind that enough temporal spacing was maintained between the two regions to avoid overlap.

3. The FITS file was copied into two parts for recording the on and off-pulse data separately. Depending on the central phase and the number of times to be averaged, for each period, the data were averaged and the central phase data was replaced by the average values. This averaging was done in time for each frequency channel and polarization separately. The rest of the data were edited out by replacing the visibilities with zeros.

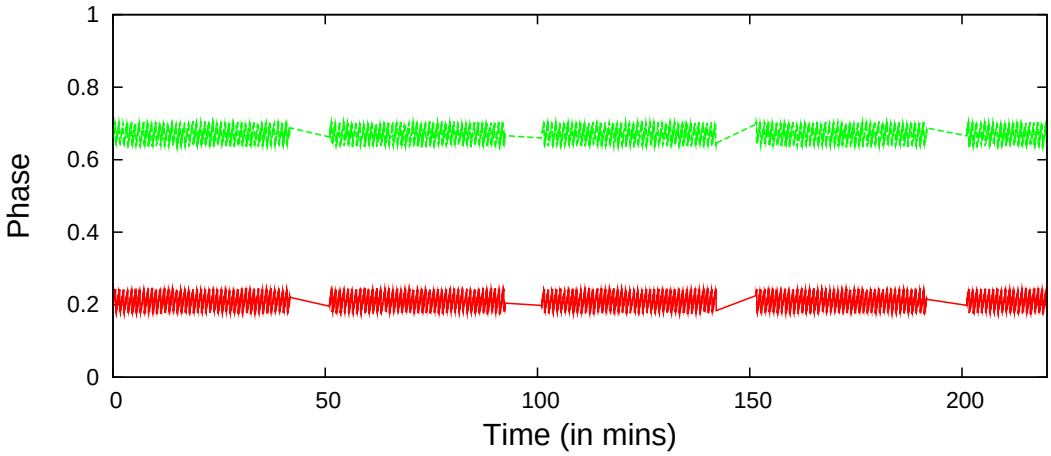

Figure 2.6 The figure shows the phase calculation for a single observing run for the On-pulse (green) and Off-pulse (red) data files. The breaks in between is due to the telescope moving to a phase calibrator (approximately 5 minutes). The concentration of the phases near the central values, 0.67 for on-pulse and 0.21 for the off-pulse, demonstrates the success of the 'Gating' process.

In the end two different FITS files were generated after the 'Gating' process with the on-pulse and off-pulse data separately. Each file consists of one visibility per baseline, channel and polarization for the duration of a single period at a temporal location closest to the central phase. The phase values of the On-pulse and Off-pulse FITS files is shown in figure 2.6, which reflects the fact that only the central phases survive in the new files after the 'Gating' process.

2.3.4 Imaging

The two files containing the on-pulse and off-pules data for each observing run were imaged independently using the standard NRAO AIPS package. Each observing run was interspersed with a 'Phase-calibrator' to correct for complex gain variations at large timescales and the fluctuations across the frequency band for each antenna. The flux scale for each observing run was estimated by observing standard flux calibrators like 3C48, 3C147 and 3C286 and using measurements of Baars et al. (1977) with latest corrections by Perley et al. (2010). The data files were recorded at high

time integrations making their sizes very large ($\geq$100 gigabytes). However, after the 'Gating' process there were a large number of redundant points due to editing out of data (about 90–95% redundancy). In order to facilitate ease of handling of the data files we used the task 'UVCOP' in AIPS to remove the redundant data points and only keep the central phase which contained the gated visibilities. The sources were passed through several rounds of 'Phase' only self calibration and one round of 'Amplitude and Phase' self calibration to correct for systematic variations at finer timescales. At every stage corrupted data were removed by employing standard and non standard techniques of RFI removal. After the final images were obtained the search for off-pulse emission were carried out by looking for emission in the location of the pulsar, i.e. to look for a point source at the position of the pulsar as seen in the on-pulse data.

During our studies for this thesis we searched for off-pulse emission in six pulsars B0525+21, B2045–16, B1237+25, B0834+06, B0320+39 and J2144–3933 at 325 MHz and 610 MHz and detected off-pulse emission in the first five pulsars at both frequencies. An example of one such detection is shown in figure 2.7. In chapters 3 and 4 we undertake a detailed analysis of these results and their implications. Before we move on we conclude this section with an independent estimate of the correctness of the imaging process. The on-pulse and off-pulse images have a large number of detectable sources (> 50) in their field of view. All the sources should be identical in both the images apart from the pulsar on/near the center of the field. The two fields were imaged independently and we determined the ratio of the flux levels for the high SNR sources in the field which should be identical in an ideal case. In figure 2.8 we show the ratio of the flux levels of surrounding sources in the on-pulse and off-pulse images which shows a scatter around unity thereby validating the imaging process.

2.4 Authenticity of the Off-pulse Detections

In the course of our studies we have detected the presence of off-pulse emission from pulsars which we believe is the first instance of such detections. As already mentioned earlier ours were not the first attempt made at these studies and our success at these

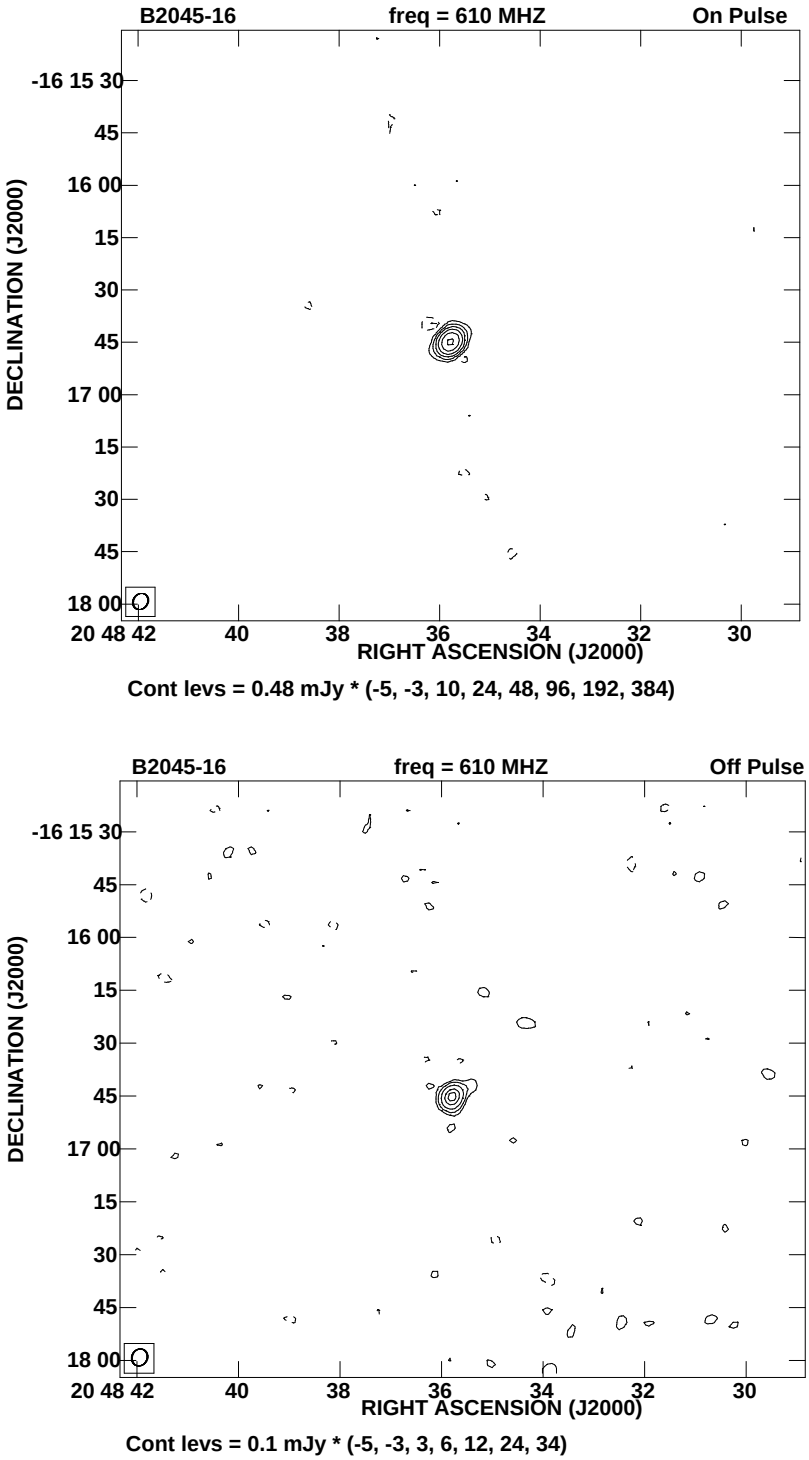

Figure 2.7 The figure shows the contour map in the position of the pulsar B2045–16 for the on-pulse (top) and off-pulse (bottom) respectively. The observations were carried out at 610 MHz and significant Off-pulse flux ($\gg 5\sigma$) was detected for this pulsar.

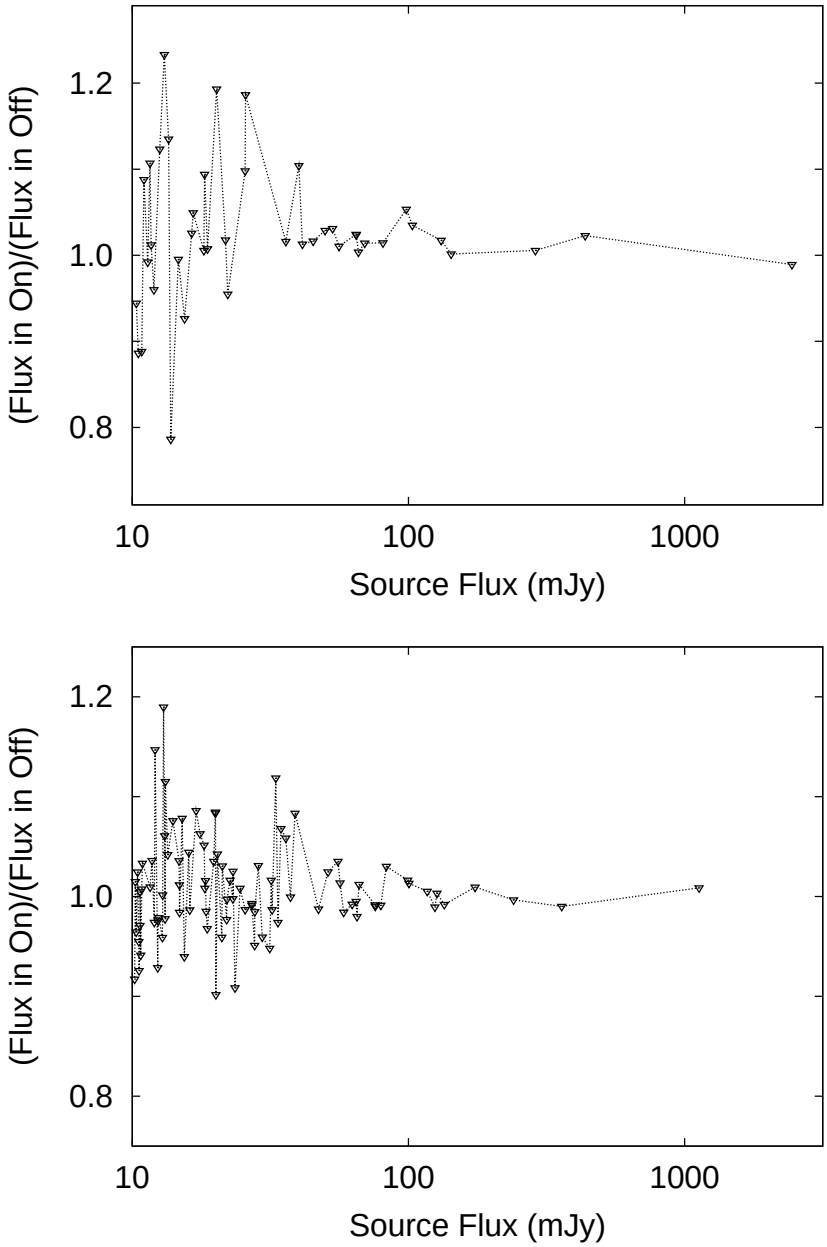

Figure 2.8 The figure show the ratio of Flux values of the surrounding sources in the on-pulse and off-pulse images for the pulsars B0525+21 (left) and B2045–16 (right). The Flux values are identical for both the observations despite the imaging analysis being independent for the on and off-pulse fields. The scatter in the flux ratios increases towards the lower flux range which is expected due to noise contributions becoming prominent.

detections were a result of the following conditions at our favour.
1. Our studies were carried out at the low frequency bands of 325 MHz and 610 MHz. The pulsar radio emission being step spectrum with typical spectral indices of $\sim$ -1.8 (Maron et al. 2000), is supposed to be brighter at these frequencies and thereby easier to detect.
2. The GMRT used for our studies is one of the most sensitive interferometers operating at meter wavelengths. In addition the greater flexibility of the imaging process to correct for the systematic variations made it possible to detect low level emissions.
3. The technique of 'Offline-Gating' developed for these detections made secure separation of the on and off-pulse regions with sufficient flexibility to check for inconsistencies in the separation process and easily rectify them.
4. The higher spatial resolution of an interferometer greatly reduces the coincidence of unrelated sources, thereby reducing the probability that the off-pulse emission is from an unrelated nearby source within the field of view.

In this section we look at certain scenarios, given the uniqueness of our detections, where the off-pulse emission can be a spurious effect in the signal and receiver chain of the telescope or an unrelated background source and rule them out one by one.

2.4.1 Positional Coincidence of Background source

To determine the probability of finding an unrelated source coinciding with the pulsar we used the VLA FIRST catalogue (Becker et al. 1985) to determine the following relationship between source counts (N) and flux-density (S):

$$logN = 2.2 - 0.826 \times logS + log(\delta S) + log(A_{sky}). \tag{2.3}$$

where S is the flux at 1.4 GHz in mJy, δS is the flux bin width at 1.4 GHz in mJy and A_{sky} is the area of sky under consideration in $degree^2$.

The area of the synthesized beam is $\sim$100 $arcsec^2$ at 325 MHz and $\sim$25 $arcsec^2$ at 610 MHz. The flux density for consideration in equation 2.3 is between 3$\times$image rms and 5–10% (Off-pulse flux level) of the pulsar flux, translated to 1.4 GHz using spectral index $\gamma = 0.75$). This yielded a probability of coincident unrelated sources

of $\sim 1.5 \times 10^{-3}$. The probability of detecting coincident sources for five pulsars is the fifth power of the above number and therefore highly improbable.

2.4.2 Error in Recorded Time

This scenario required that a certain percentage of the on-pulse data fell within the off-pulse gate. Any monotonic drift in time, without recovery, would have smeared out the pulse obtained by folding the auto correlation data. However our folding exercise have detected the pulsed signal (see figure 2.5) with a high degree of significance. In an alternate scenario the time can maintain an accurate long term average but with large excursions in the values of the individual time stamps, i.e. excursions of about half the pulsar period. This is a contrived scenario and the a histogram of the time difference between adjacent data would show a large scatter in this case. The histograms plotted in figure 2.9 show a tight scatter around the expected mean values.

2.4.3 Leakage in Signal Chain: Noise Correlation

This scenario requires temporal correlation between data separated by at least half the pulsar period. The basic sampling interval of the GMRT correlator is 30.72 nanoseconds. A cross correlated band is output every 16 microseconds by fourier transforming 512 such samples. The data output every 16 microseconds should be independent from all other such data in the time series. Around 8000/16000 independent samples are averaged to obtain the data output rates of the 128/256 msec modes. Given the independence at the 16 microseconds level it is difficult to envisage correlation between two consecutive time samples let alone across half the pulsar period. The standard interferometric mode of the GMRT would not be affected as a result of this leakage as they are mostly worried about time average signals and their integration time is rarely less than 2 seconds. The leakage, if present, would redistribute the flux density along the time axis without causing any change in the measured flux density. We tested this possibility by estimating the temporal correlation in the 128 msec mode of the GHB time series data. Assuming that the off-pulse

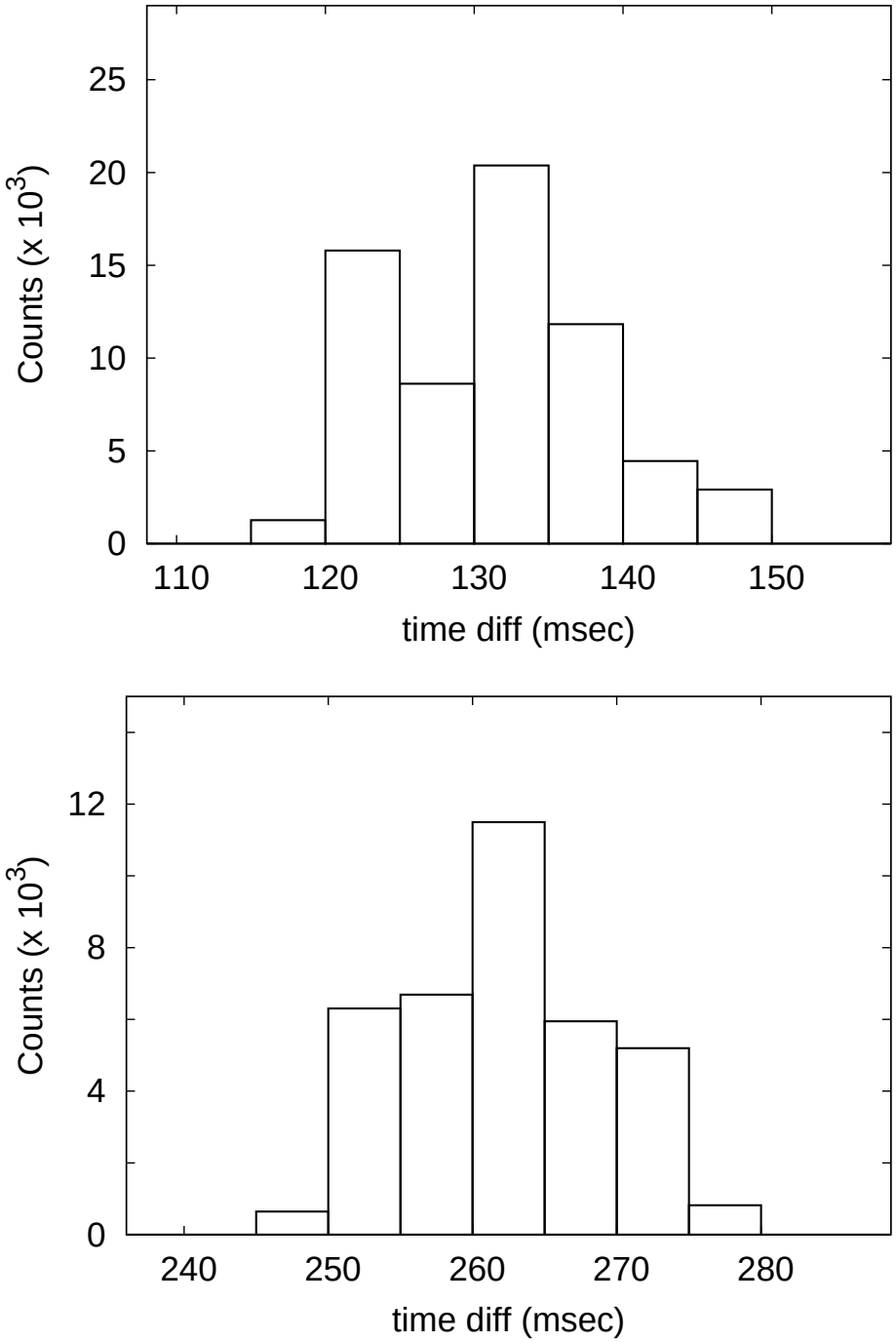

Figure 2.9 The time difference between adjacent time stamps were determined for two different observations with 128 msec mode of GHB (top) and 256 msec mode of GHB (bottom) and histogram of the time integrations were generated as shown. The histograms show very little spread indicating the absence of any time leakages.

was entirely due to leakage of the signal from the on-pulse time bins to the off-pulse bins we estimated the required leakage for a spurious detection of the observed off-pulse. In this experiment we investigated the consequence of such a correlation on the noise data. In the next level we will further these studies by introducing a narrow, clean pulse into the GMRT receiver system to directly measure such a leakage.

As a first step, we ran simulations to estimate the auto-correlation function for noise in the presence of leakage sufficient to generate the observed off-pulse, i.e. we generated a noise data series and smeared each data point into subsequent data points according to a particular time profiles like constant leakage or linearly decreasing leakage in subsequent time bins. We then recorded 6×10 minute scans of noise data (128 msec mode of GHB) but with Front-End termination which sealed the telescope at the antenna feeds ensuring that no temporally continuous external source (cosmic sources and RFI), which would be correlated across the entire observing session, was present in the noise data.

The auto-correlation for each baseline-channel (435×120) data was separately calculated for each scan. The median autocorrelation profile and the scatter are shown in Figure 2.10 (left panel). The worst data are at the 0.1 per cent level but the median is only about 0.04 per cent. The profile does not fall to zero at large time lags, indicating non stationarity of the noise signal. We obtained a similar behaviour by introducing a time varying mean level into the noise in our simulations. This time variation in the mean level may reflect the system gain variations as well, which would have been corrected to a certain extent by self calibration process during imaging. Therefore the profile is a firm upper limit to the contribution of temporal leaking of signals to an off-pulse detection.

Interferometric imaging is an excellent filter of bad data and a compact point source like the detected off-pulse would require most of the baselines to show high temporal auto correlation. A few bad baselines with high auto correlation would only result in noisy ripples across the image and not a localized point source in or near the field center. Therefore the median line is a more accurate measure of the leakage for our study than the extreme points in the scatter. We note that non-stationarity and gain fluctuation only occur at the 0.05 per cent level in the GMRT and would

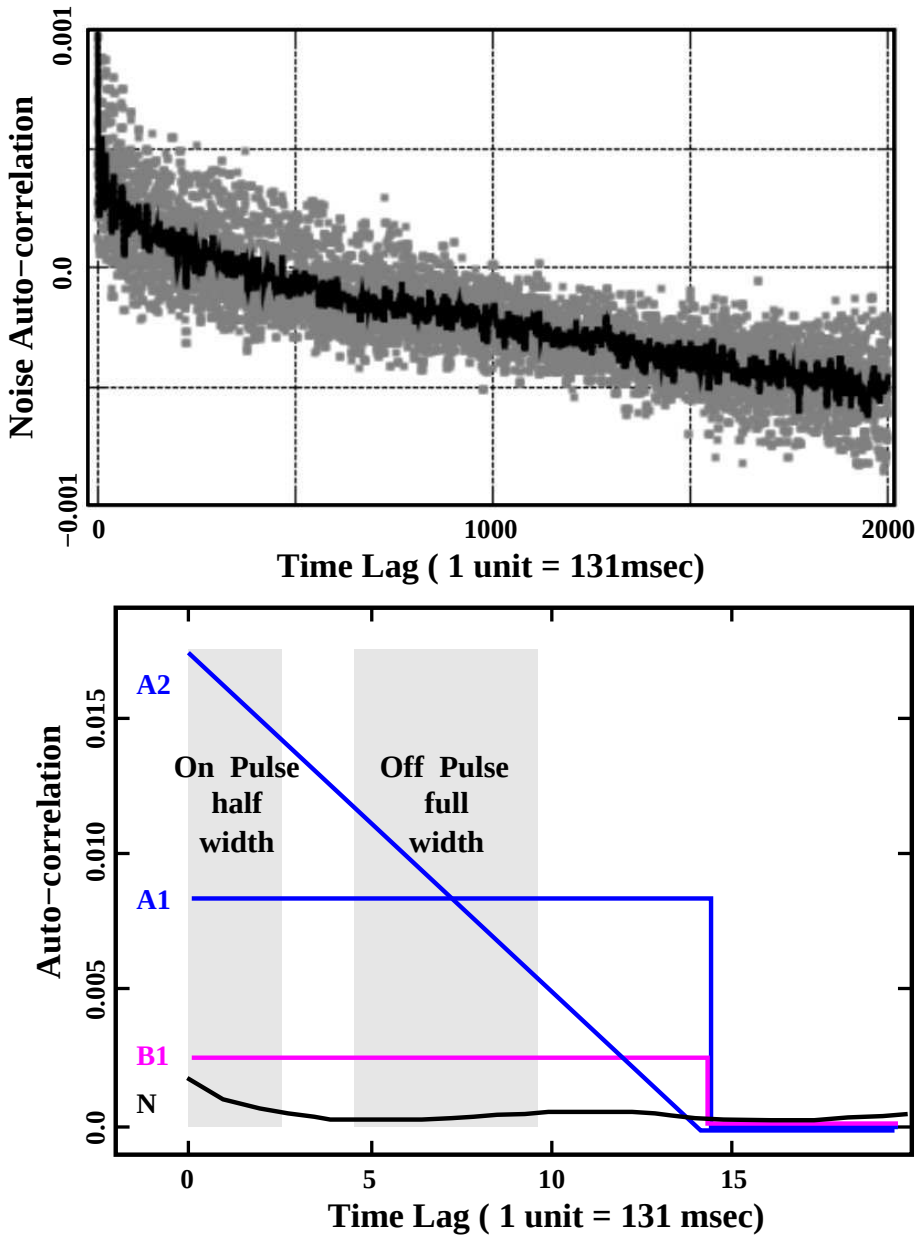

Figure 2.10 The figure shows the auto-correlation profile for frontend terminated GMRT noise data (top). The scatter plot is for each baseline, channel over the observing time while the black line is the median profile from the scatter. The non-zero value even at large lags is indicative of non-stationary noise signal and system gain variation. An expanded view is also shown (bottom) which also includes the required levels of noise correlation for various time profiles and off-pulse levels which is consistently above measured correlation level.

not have a discernible effect for most imaging exercises.

The Figure 2.10 (right panel) also show a magnified representation of the relevant part of the noise auto correlation plot. A1, A2 (for one particular off-pulse level, pulsar B0525+21 at 325 MHz) and B1 (The weakest detection so far) indicate the required noise auto correlation if the detected off-pulse were due to the leaking of the signal from the on-pulse bin. The simulation recipe keeping in mind pulsar B0525+21 with 14 bins across the period is as follows:

1. The pulsar period includes 14 time bins with the on and off-pulse fluxes measured over 5 time bins being 80.2 and 3.9 mJy, respectively. Higher time resolution observations (Gould & Lyne 1998) show that the main-pulse is narrower than the extent of the bins.

2. A leakage of 0.9 per cent of the pulse flux from the first bin into each of the next 13 bins will explain the observed off-pulse. This corresponds to an auto correlation level of 0.0087. The auto-correlation profile calculated for GMRT noise (the lowest curve 'N' in figure 2.10, right panel), is smaller than the required amount by a factor of at least 20.

3. A temporally reducing leakage is more likely. A linearly reducing leakage (curve A2) requires a similar average auto-correlation in the off-pulse region and a higher correlation at short lags.

4. We conclude that temporal leaking of the signal is incapable of explaining the detected level of off-pulse emission.

All the off-pulse emission detected in our studies are sufficiently above the levels of auto correlation expected from the above exercise. In addition it is worth reiterating that the correlation level determined is a generous upper limit as there is possibility of systematics and correlated gain variations which will affect these values rather than an actual leakage across bins.

2.4.4 Leakage in Signal Chain: Pulsed Noise Source

The above experiment did not account for temporal leakages due to a strong pulsed

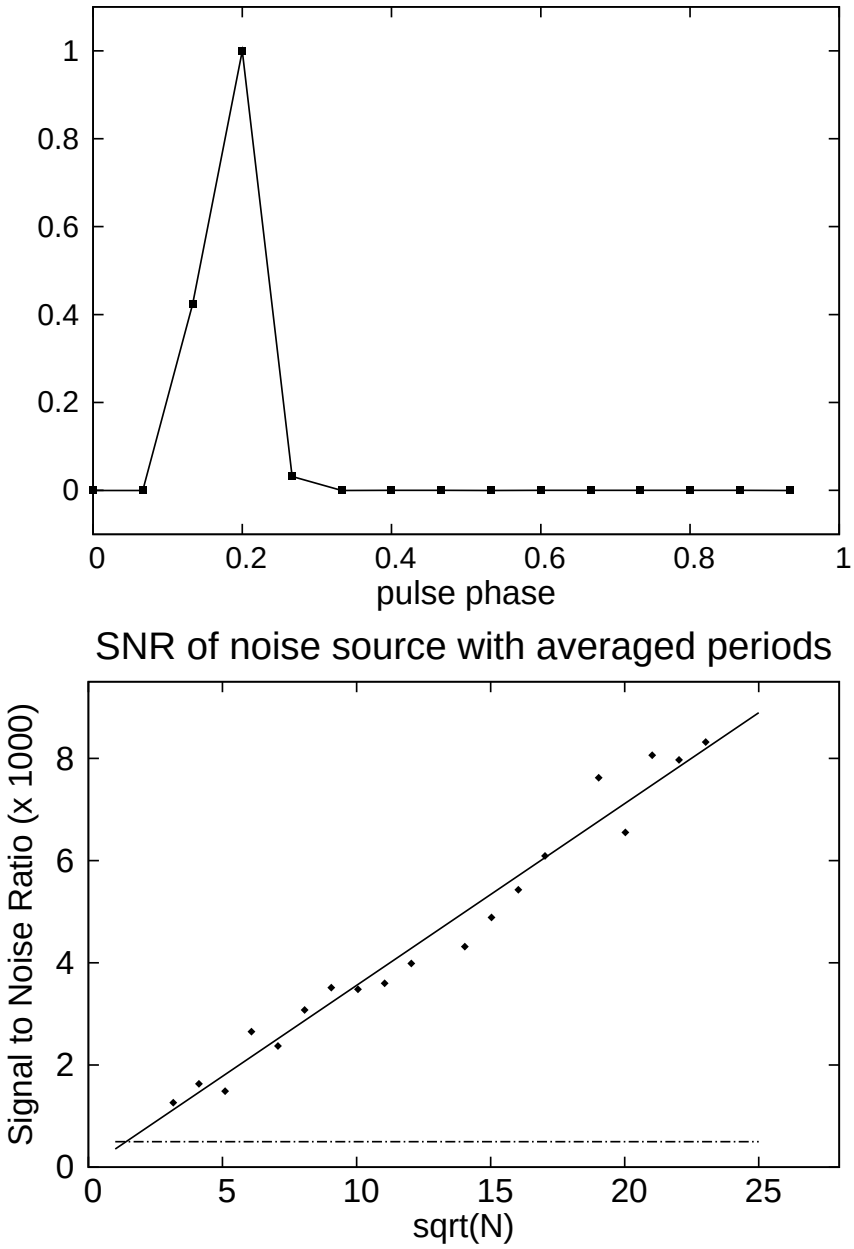

Figure 2.11 The pulsed noise source as observed with the interferometer (top), with 565 folded periods of 4 sec and a time resolution of 251 msec. The change in signal to noise ratio of the pulsed signal with increasing number of folded periods (N) from 10 periods to 565 periods (bottom). The dark solid lines represent a linear increase of SNR with $\sqrt{N}$ indicating the baseline to be noise like. The dot dashed horizontal line is the level at which the SNR was expected to saturate if temporal leakage was the source of off-pulse emission.

signal as seen in pulsars. In order to investigate this effect a series of narrow single pulses with no off-pulse emission was required to be introduced in the receiver system. A broad-band pulsed noise source with a period of 4 seconds and a duty cycle of 32 millisecond was developed for this purpose. The power of the on-pulse signal was -5 dbm and the signal was down by 30 db in the off-state, which was significantly below the detected off-pulse emission. The noise source was radiated from an antenna in the central square of the GMRT. Interferometric data was recorded using the 256 msec mode of the GSB for about half an hour with the noise source switched on. Since the noise source was in the near field, the geometrical delay calculations were vastly complicated (it is a function of the distance of the individual antennas from the pulsed noise source). We did not correct for any geometrical delay in the correlator chain. This implied that only for a handful of cases (10 baselines) the antennas were close enough for the coherence condition to hold and these baselines were used for the subsequent analysis as discussed below.

If there was no leakage of the pulsed signal in time, the folded profile with increasing number of periods averaged together, for any baseline, would show a decrease in the off-pulse noise and an increase in the signal to noise ratio (SNR) by a factor $\sqrt{N}$, where N is the number of folded periods. The interferometer measures the correlation between the voltages recorded by the individual elements (Thompson et al. 1986).

$$r(\tau) = \frac{1}{2T} \int_{-T}^{T} V_1(t) \times V_2(t-\tau)\ dt \tag{2.4}$$

where the quantity $r(\tau)$ is related to the intensity of the incident signal and 2T is the temporal resolution (251 msec).

We assume that the system introduces a constant fractional leakage ϵ into the adjacent time bin (this is the most likely situation, besides any other situation will lead to a lower SNR). The correlation in the adjacent bin in such a scenario is given as:

$$r'(\tau) = \epsilon^2 \frac{1}{2T} \int_{-T}^{T} V_1(t) \times V_2(t-\tau)\ dt, \quad \epsilon < 1 \tag{2.5}$$

The statistics of the bins adjacent to the pulsed source is characterized by a mean(μ)

and rms (σ) given as:

$$\mu = \epsilon^{2n} \frac{1-\epsilon^{2N}}{N\ (1-\epsilon^2)} \times r(\tau) \tag{2.6}$$

$$\sigma \sim \frac{\epsilon^{2n}}{(1-\epsilon^2)} \sqrt{\frac{1}{N}\frac{1-\epsilon^{2N}}{1+\epsilon^2}} \times r(\tau) \tag{2.7}$$

Here the first bin is the n^{th} bin from the pulsed source with N bins used for statistics; $r(\tau)$ is the correlation in the pulsed source bin. The statistics of the adjacent bins will be governed by a combination of gaussian statistics due to random noise and the constant leakage into adjacent bins. However for sufficient long averaging the effect of random noise will be overshadowed by the leakage term and the SNR for the pulsed source would saturate at a constant level.

The interferometric data from the pulsed noise source were folded with a periodicity of 4 seconds to determine the profile (see fig 2.11). A large number of profiles of the noise source were generated by folding an increasing number of periods. The SNR for each of these profiles were calculated, by dividing the total signal in the noise bin with the rms fluctuation in the adjacent bins. In figure 2.11 we plot the SNR as a function of the square root of the number of periods (points) along with the best fit (dark solid line).

We have detected off-pulse emission in pulsars at a level of 0.5 – 1 % of the on-pulse flux. The off-pulse region in our studies are 5 bins (n=5) from the on-pulse and we can calculate the leakage (ϵ) required using equation 2.6 and 2.7 to explain the detected off-pulse. This would lead to a SNR $\sim$ 500, as represented by the dot dashed horizontal line in figure 2.11. However the bins adjacent to the noise source continue to follow gaussian statistics at SNR $\sim$ 8000 as seen in figure 2.11. This implies that the temporal leakage can only lead to a off-pulse emission which is less than 0.03% of the on-pulse flux. Hence the detected off-pulse emission cannot originate as a result of temporal leakage of the on-pulse signal into adjacent time bins.

The unprecedented detection of off-pulse emission makes it imperative to exhaust all possibilities of spurious detection. We have detected of off-pulse emission in multiple epochs and frequencies using different correlator systems and also ruled out spurious detection that can result due to temporal leakage. We have established

that the off-pulse emission is genuine and not a result of systematic anomaly. We now look ahead to determining the nature of off-pulse emission and report a detailed descriptions of our results and their implications.

Chapter 3

Off-pulse Emission

3.1 Sample Selection

The time resolution of the interferometric data puts a natural lower limit to the periodicity of the pulsar that can be used for our studies. The main pulse signal is usually spread between three time bins and ensuring one bin on either side for secure separation of the on and off-pulse regions there is the least requirement of six bins in the pulsar period for the 'Gating' process. The minimum resolution of the interferometer is around 128 milliseconds which implies that we can study pulsars in excess of 0.8 seconds. In order to ensure proper signal to noise for the off-pulse detection we restricted our studies to periods > 1.25 seconds, ensuring at least 3 bins per period in the off-pulse data. To ensure proper upper limits for off-pulse detections we restricted our studies to nearby pulsars with relatively high flux values (> 15 mJy) at low frequencies (400 MHz). This restricted the number of pulsars that could be used for our studies. We selected six well known pulsars B0525+21, B2045–16, B0834+06, B1237+25, B0834+06, B0320+39 and J2144–3933 for our studies, the basic properties of which are listed in table 3.1. The pulsars were selected to cover a varied period range from 1.27 seconds to 8.5 seconds. In addition the pulsars did not conform to any special geometries, like aligned rotators with wide profiles or orthogonal rotators with interpulse, and did not exhibit any other pulsed emission component away from the main pulse like precursors.

Table 3.1 Properties of Pulsars selected for our studies.

Pulsar	Period	DM	Distance	τ_c	$\dot{E}$	V_{trans}	$Flux_{400}$
	seconds	cm^{-3} pc	kpc	year	erg s^{-1}	km s^{-1}	mJy
B0525+21	3.746	50.937	2.28	1.48×10^{6}	3.0×10^{31}	229	57
B2045–16	1.962	11.456	0.95	2.84×10^{6}	5.7×10^{31}	510	116
B1237+25	1.382	9.242	0.84	2.28×10^{7}	1.4×10^{31}	460	110
B0834+06	1.274	12.889	0.72	2.97×10^{6}	1.3×10^{32}	174	89
B0320+39	3.032	26.01	1.49	7.56×10^{7}	9.0×10^{29}	240	34
J2144–3933	8.510	3.35	0.16	2.72×10^{8}	3.2×10^{28}	126	16

The data presented in this table was obtained from the ATNF database which is freely available at: www.atnf.csiro.au/people/pulsar/psrcat/ and Manchester et al. (2005)

3.2 Observations & Results

In this section we report the observations carried out to detect off-pulse emission from long period pulsars. We have observed the six pulsars at 325 MHz and 610 MHz frequency bands of GMRT. The observations were carried out between January 2010 and August, 2011 (see table 3.2) using specialized interferometric high time resolution modes (128/256 msec modes) supported by the GMRT correlator system. During the early months of 2011 the GMRT correlator system was upgraded from the previously existing Hardware backend (GHB) to a Software backend (GSB) which is currently the default system. The GHB was operated at both the 128 and 256 msec modes with bandwidth of 16 MHz split into 128 channels. The GSB initially could only operate at 256 msec mode over a 16 MHz bandwidth spread across 32 channels. The GSB was ultimately extended to operate at 128 msec mode with 16 MHz bandwidth split into 256 channels. All these modes were used during the span of our observations.

The table 3.2 documents the details of observations for our off-pulse studies including date of observation (column 1); frequency band and channels (column 3); the telescope observing time on each source excluding calibration times (column 4); the time resolution of the interferometer (column 5); the correlator system used (column 6); the angular resolution (column 7); the on-pulse flux averaged over the pulsar pe-

Table 3.2 Observational details

Date	Pulsar	freq(chan) MHz	Time mins	time res msec	Corr	res ″×″	On flux(rms) mJy	Off flux(rms) mJy	Off/On
18 Jan, 2010	B0525+21	325(128)	160	261	GHB	9.5×6.5	30.0±2.1(0.55)	3.9±0.5(0.45)	0.130±0.026
08 Jul, 2011	B0525+21	325(32)	240	251	GSB	8.3×6.7	44.5±2.4(0.65)	6.6±0.5(0.4)	0.148±0.019
09 Jul, 2011	B0525+21	325(32)	120	251	GSB	10.0×7.4	48.2±2.6(0.7)	6.5±0.6(0.5)	0.135±0.020
15 Feb, 2011	B0525+21	610(32)	330	251	GSB	4.8×4.0	21.1±1.5(0.45)	3.6±0.3(0.13)	0.171±0.026
22 Jul, 2011	B0525+21	610(32)	240	251	GSB	5.4×3.7	20.0±1.2(0.65)	2.8±0.2(0.13)	0.140±0.018
16 Jan, 2010	B2045–16	325(128)	180	131	GHB	11.9×7.2	110.5±7.9(2.1)	4.3±1.1(0.65)	0.039±0.013
03 Aug, 2011	B2045–16	325(256)	200	125	GSB	10.2×7.7	57.5±3.2(0.35)	6.8±0.4(0.2)	0.118±0.014
14 Feb, 2011	B2045–16	610(128)	180	131	GHB	5.8×4.3	23.9±1.7(1.0)	1.1±0.2(0.13)	0.046±0.012
25 Aug, 2011	B2045–16	610(256)	140	125	GSB	4.9×4.3	43.2±3.1(0.45)	4.6±0.3(0.11)	0.106±0.015
27 Apr, 2010	B1237+25	325(128)	270	131	GHB	8.8×8.0	233.3±12.8(6.2)	3.4±0.6(0.53)	0.015±0.003
13 Aug, 2011	B1237+25	610(256)	325	125	GSB	5.9×5.3	70.0±4.2(1.23)	7.6±0.5(0.12)	0.109±0.009
26 Apr, 2010	B0834+06	325(128)	310	131	GHB	11.5×6.2	168.3±9.1(6.2)	3.2±0.6(0.55)	0.019±0.004
27 Aug, 2011	B0834+06	610(256)	315	125	GSB	6.3×4.9	27.0±1.9(0.34)	3.4±0.3(0.13)	0.125±0.014
25 Aug, 2011	B0320+39	325(32)	315	251	GSB	10.5×6.2	39.4±2.1(0.39)	4.7±0.3(0.18)	0.120±0.010
12 Aug, 2011	B0320+39	610(32)	360	251	GSB	5.3×4.3	9.9±0.6(0.12)	1.1±0.1(0.06)	0.107±0.011
15 Aug, 2011	J2144–3933	325(32)	335	251	GSB	11.2×7.5	4.1±0.3(0.52)	ND	-
25 Jul, 2011	J2144–3933	610(32)	270	251	GSB	6.4×3.6	2.6±0.2(0.40)	ND	-

riod along with the noise rms in the map (column 8); the detected off-pulse flux with the noise rms in map (column 9); the off-pulse to on-pulse flux ratio (column 10).

The folded profile for each pulsar and the on and off-pulse gates are shown in figure 3.1. We briefly describe the basic results for each pulsar below:

B0525+21 was the first pulsar where off-pulse emission was detected, as shown in figure 3.2, and have been observed multiple times at both 325 MHz (thrice) and 610 MHz (twice). The off-pulse emission have been detected at about 15% level of the integrated flux which is less than 1% with respect to peak flux. The off-pulse emission was detected with sufficient significance in all the images ($> 5\sigma$, see table 3.2). The field contained the extremely strong and extended crab nebula $\sim 1.5^{\circ}$ away. In order to reduce the effect of ripples due to uncorrected phase errors of the extended source at the position of the pulsar a uv cutoff of 1.5 kλ was used to image the 325 MHz data (the crab nebula was towards the edge of the primary beam at this frequency).

B2045–16 was also one of the initial pulsars in our sample where off-pulse emission was detected as shown in figure 3.3 and like the previous case have been observed multiple times at 325 MHz and 610 MHz (twice at each frequency). The off-pulse flux for this pulsar showed large variations over the observing sessions and we would carry out a detailed investigation in a later section. In one of the observations on 16^{th} January, 2010 the pulsar was inadvertently observed $\sim 35'$ away from the phase center (roughly 60% of antenna efficiency), however off-pulse emission was detected during this observation as well.

B1237+25 was one of the shorter period pulsars observed in our sample. The off-pulse emission was detected at both the observing frequencies as shown in figure 3.4. The off-pulse had different detection strengths at the two frequencies with detection levels of $\sim 1.5\%$ at 325 MHz (6σ detection) and $\sim 10\%$ at 610 MHz with respect to the period averaged on-pulse flux.

B0834+06 was the shortest period pulsar observed in our sample. The off-pulse emission was detected at both the observing frequencies as shown in figure 3.5. The off-pulse had different detection strengths at the two frequencies with detection levels of $\sim 2\%$ at 325 MHz (5.8σ detection) and $\sim 10\%$ at 610 MHz with respect to the period averaged on-pulse flux. The off-pulse detection was especially challenging

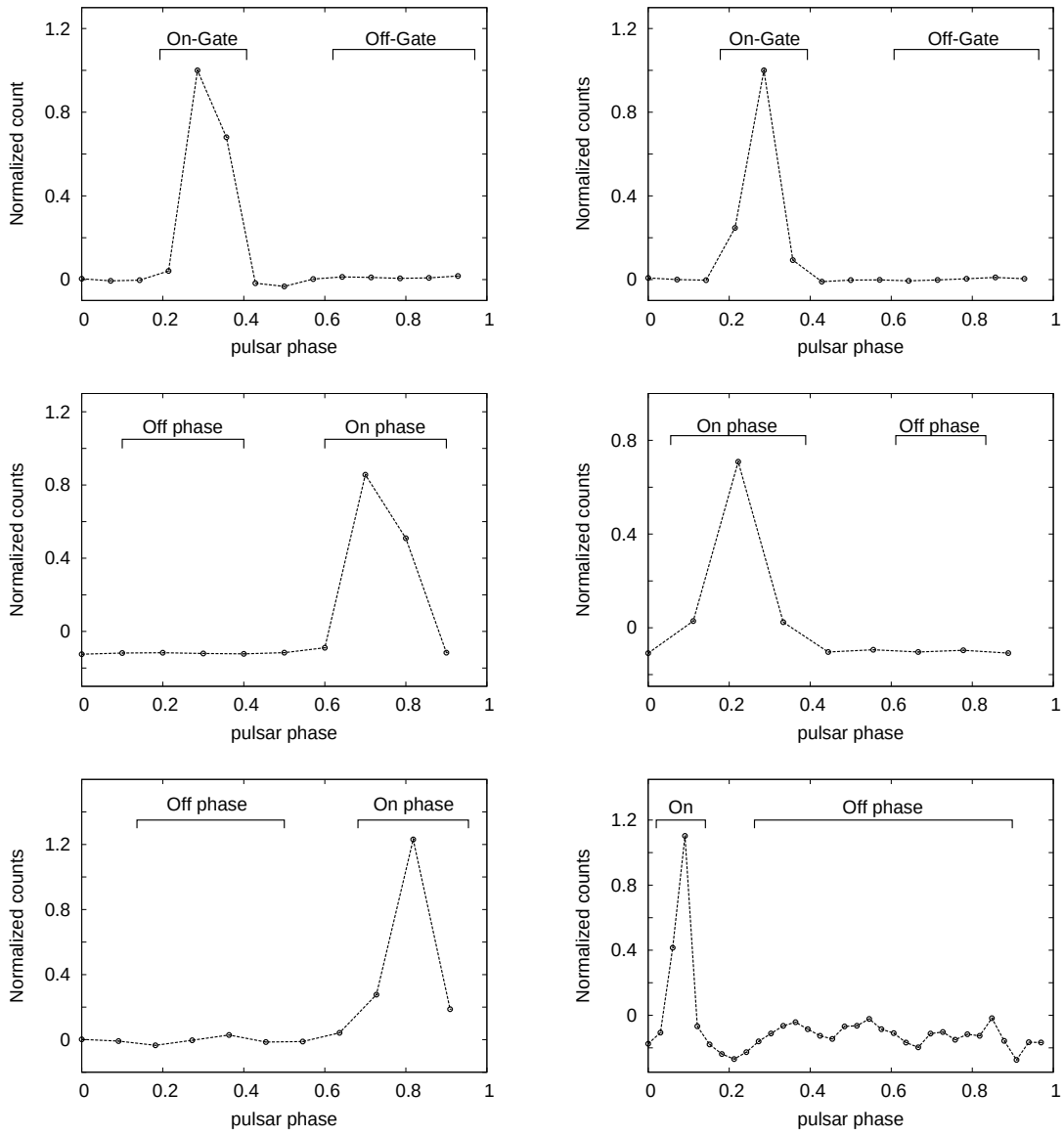

Figure 3.1 The figure shows the folded profile for the six pulsars B0525+21 (top left), B2045–16 (top right), B1237+25 (middle left), B0834+06 (middle right), B0320+39 (bottom left) and J2144–3933 (bottom right). The profiles were obtained folding the auto correlation data and the number of bins in each profile is determined by the periodicity of the pulsars and the time resolution of the interferometer. The figure also shows the phases of the On-pulse and Off-pulse gates in each pulsar used for our studies.

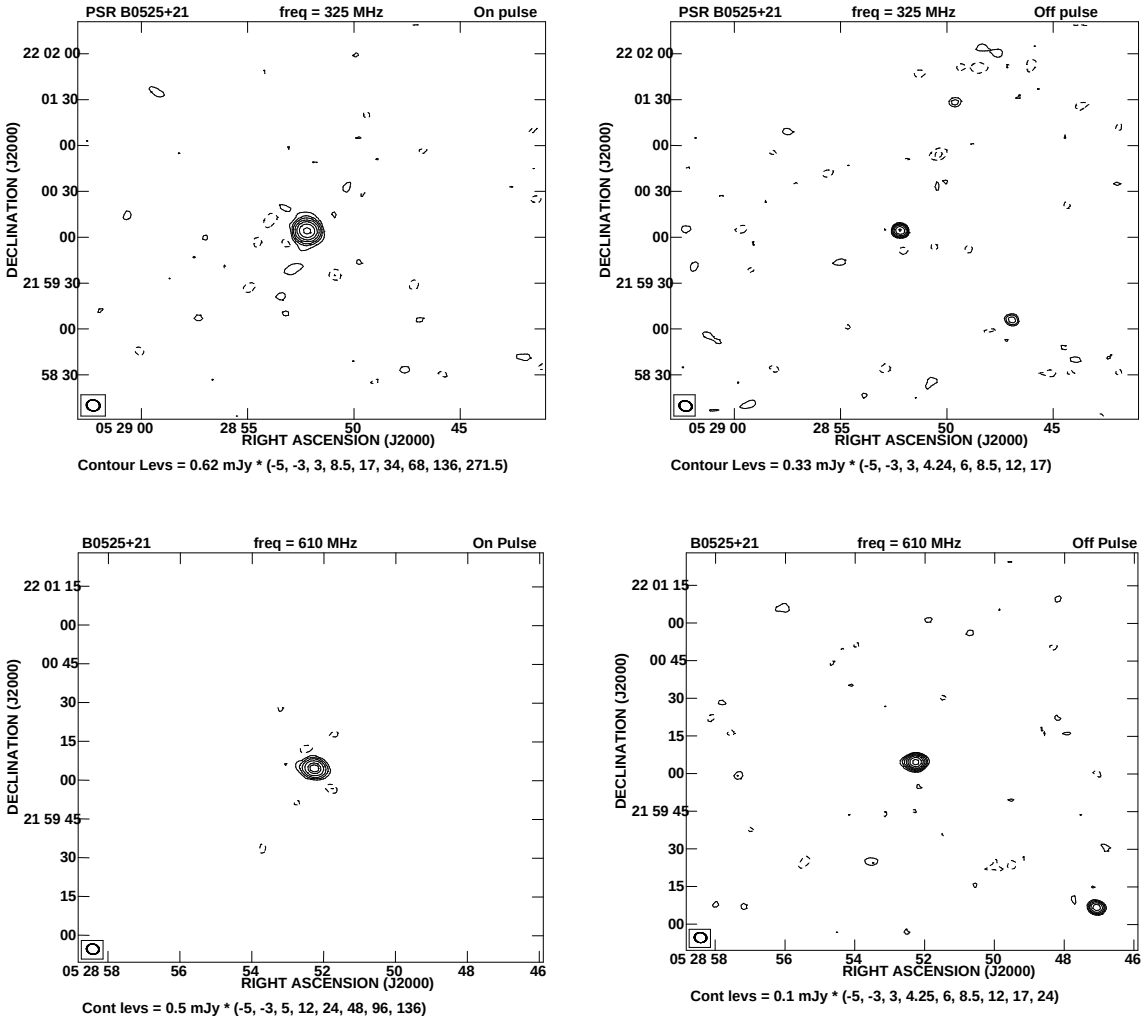

Figure 3.2 The figure show the contour maps for the on pulse (left panel) and off pulse (right panel) detections for the pulsar B0525+21. The top panel show the detections at 325 MHz for the observations on 8^{th} July, 2011. The bottom panel show the detections at 610 MHz for the observations on 15^{th} February, 2011.

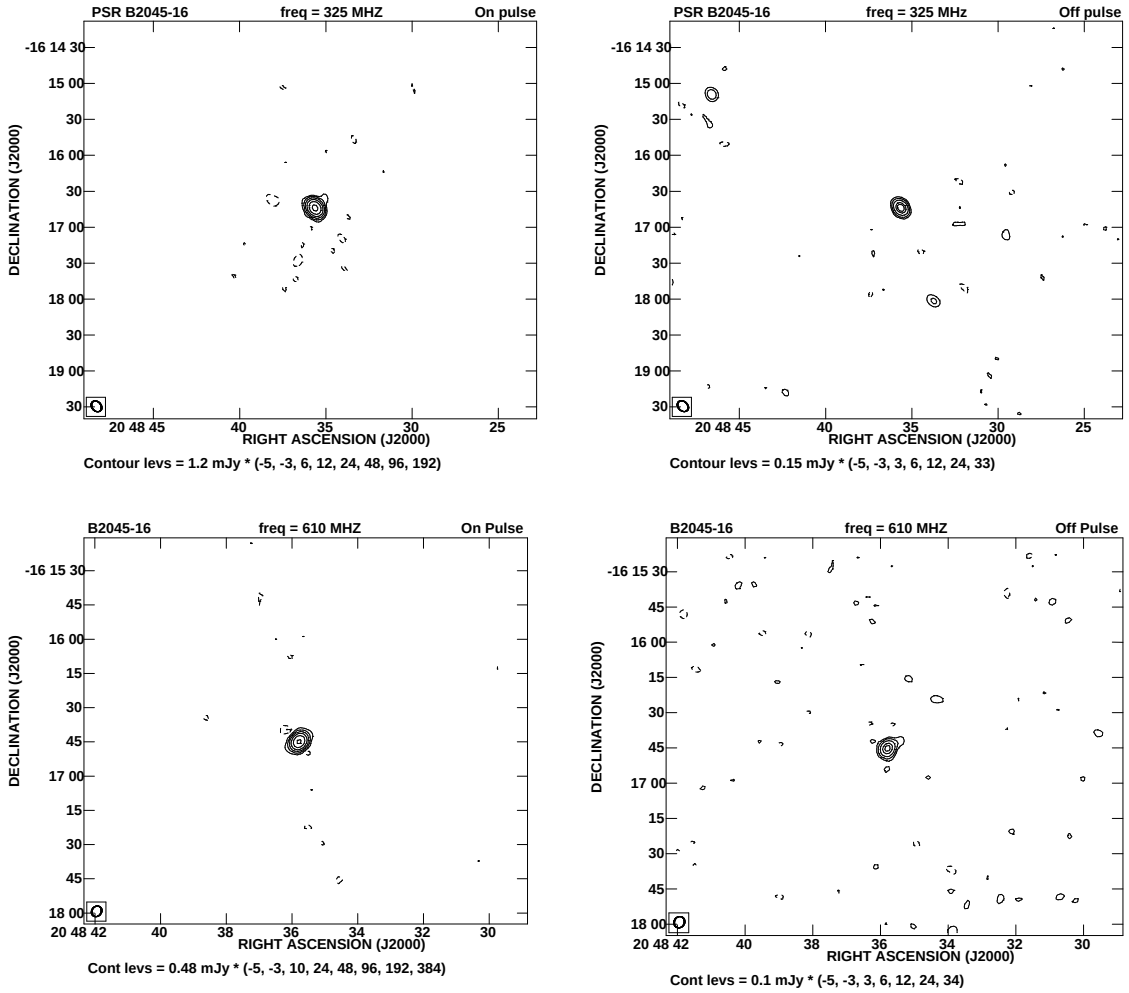

Figure 3.3 The figure show the contour maps for the on pulse (left panel) and off pulse (right panel) detections for the pulsar B2045–16. The top panel show the detections at 325 MHz for the observations on 3^{rd} August, 2011. The bottom panel show the detections at 610 MHz for the observations on 25^{th} August, 2011.

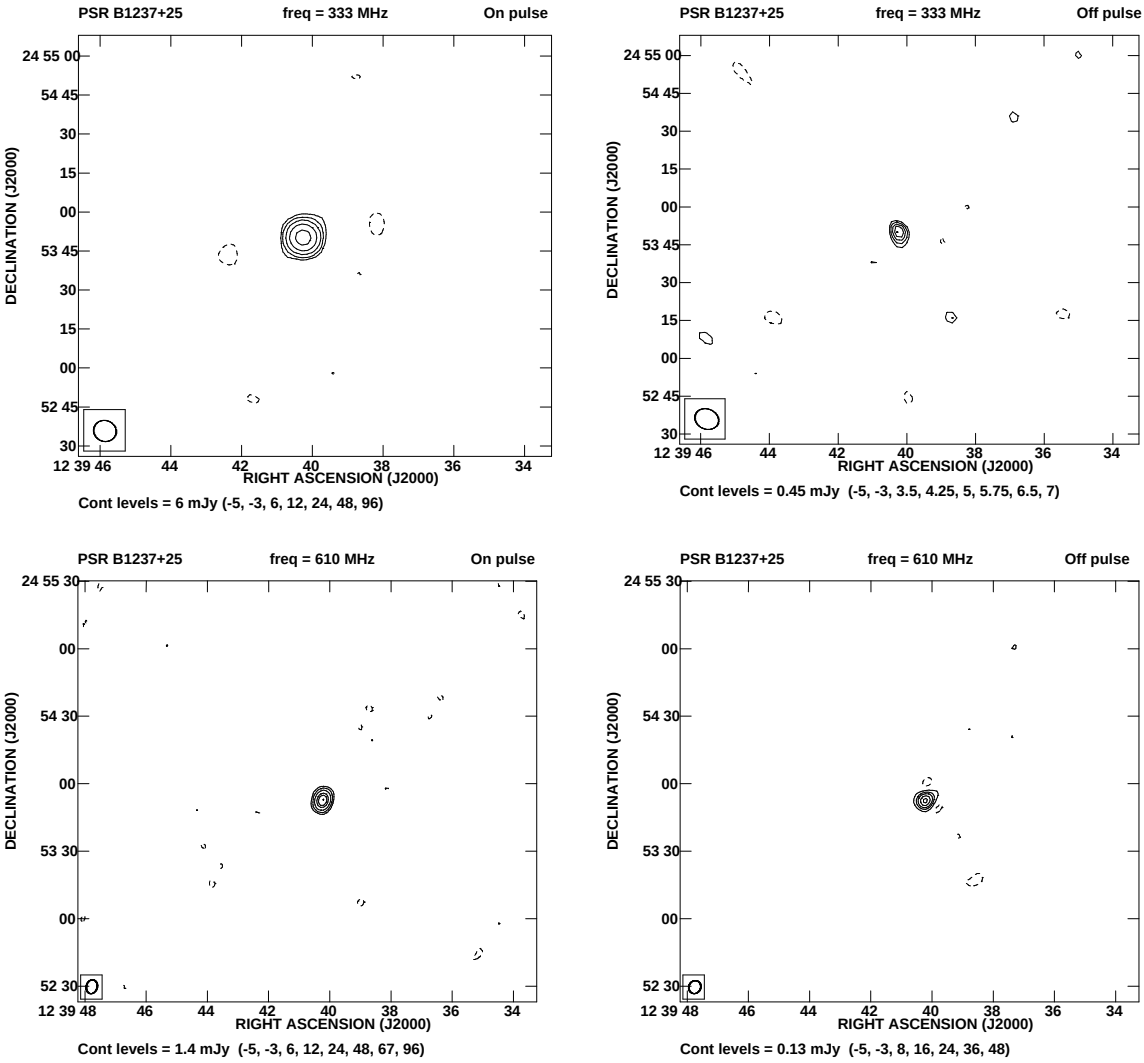

Figure 3.4 The figure show the contour maps for the on pulse (left panel) and off pulse (right panel) detections for the pulsar B1237+25. The top panel show the detections at 325 MHz for the observations on 27^{th} April, 2010. The bottom panel show the detections at 610 MHz for the observations on 13^{th} August, 2011.

particularly at 325 MHz due to the presence of a strong source of ~ 1 Jy and located around $5'$ to the south of the pulsar. We resorted to the technique of 'PEELING' to remove the strong source and reach sufficiently deep noise levels to detect the off-pulse emission at 325 MHz.

B0320+39 was a relatively long period pulsar and the off-pulse emission was once again observed at both observing frequencies as seen in figure 3.6. The detected off-pulse was about 10% level of the period averaged on-pulse flux at both 325 MHz and 610 MHz. The on-pulse flux was relatively weak at 610 MHz but this did not affect the detection of the off-pulse emission with sufficient significance ($> 15\sigma$).

J2144–3933 was the longest period pulsar in our sample and was the only case where we did not detect any off-pulse emission as shown in figure 3.7. The pulsar was also the weakest one in our sample but we reached sufficiently deep noise levels in the images to have identified the off-pulse emission at the level of the other detections. We conclude that the off-pulse emission in this pulsar is either much weaker than those detected in other pulsars or completely absent.

3.3 Physical Characteristics of off-pulse emission

In chapter 2 we have discussed conditions where the detected off-pulse emission arise due to anomaly in the telescope system and demonstrated their unfeasibility in the context of our detections. We have also seen that the off-pulse emission just like the main pulse emission from pulsars is an unresolved point source in the map. This implies that at a distance of 1 kpc (the typical distance of the sources, see table 3.1) and our telescope resolutions of $5/10''$, any astronomical source smaller than 0.02/0.04 pc will be unresolved. This leaves two possibilities, either the off-pulse emission is due to a Pulsar Wind Nebulae (PWNe) or it originates within the pulsar magnetosphere due to a specialized emission mechanism.

The radio emission in PWNe is due to relativistic charged particles producing synchrotron emission in the ambient ISM magnetic field. The typical size of PWNe is between 0.1–1 parsec due to expansion of the pulsar wind in the surrounding ISM (Gaensler & Slane 2006). If the off-pulse emission can be constrained to several

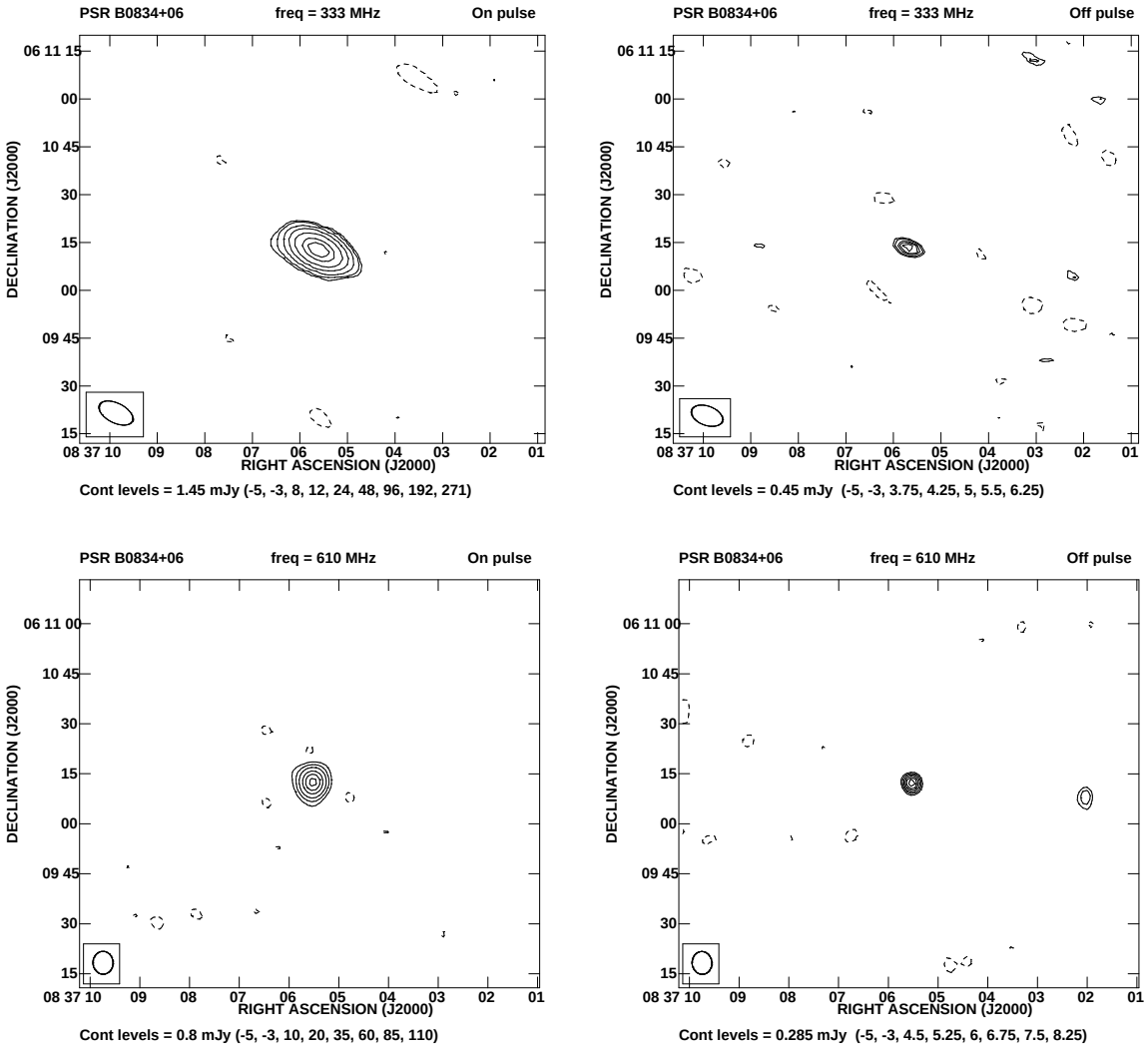

Figure 3.5 The figure show the contour maps for the on pulse (left panel) and off pulse (right panel) detections for the pulsar B0834+06. The top panel show the detections at 325 MHz for the observations on 26^{th} April, 2010. The bottom panel show the detections at 610 MHz for the observations on 27^{th} August, 2011.

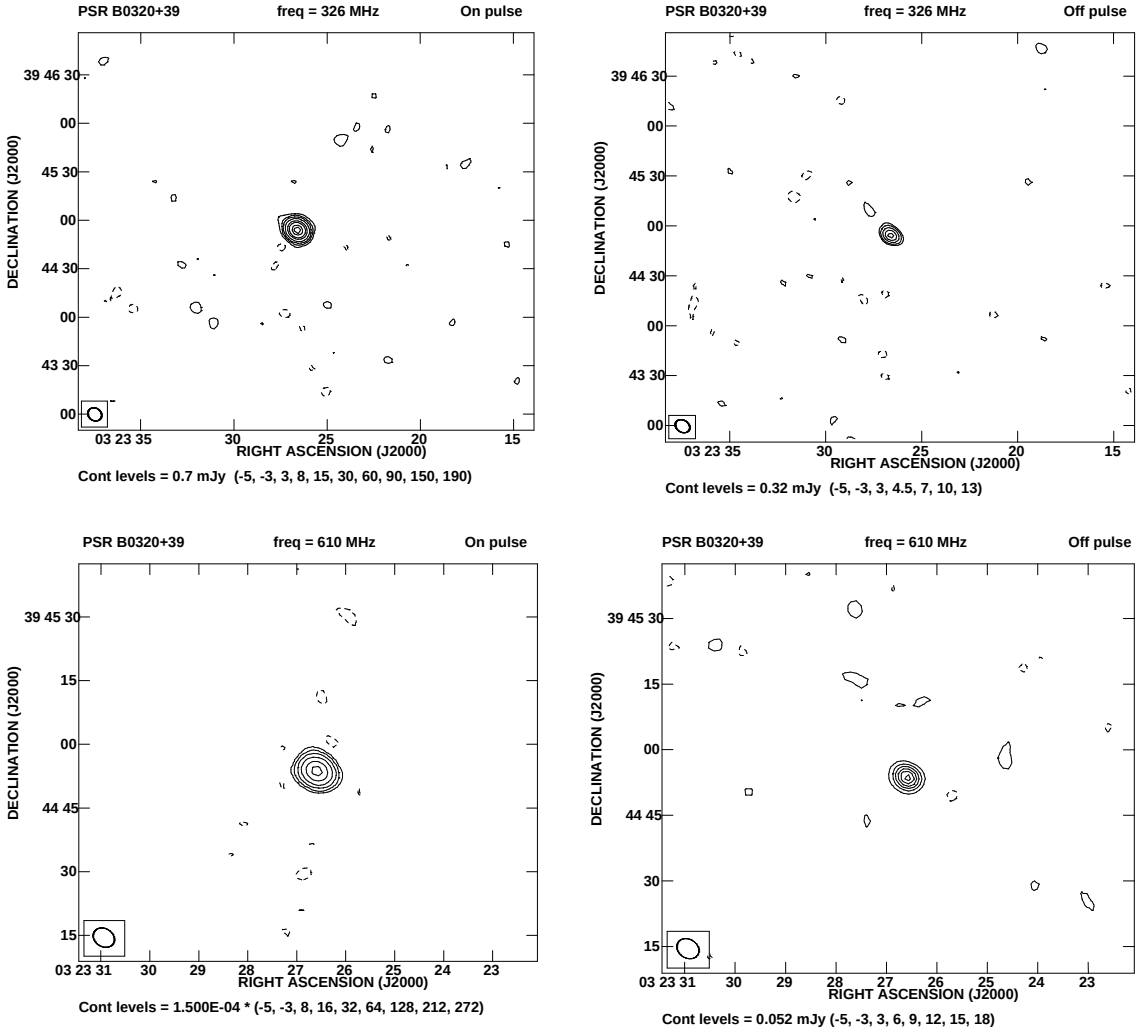

Figure 3.6 The figure show the contour maps for the on pulse (left panel) and off pulse (right panel) detections for the pulsar B0320+39. The top panel show the detections at 325 MHz for the observations on 25^{th} August, 2011. The bottom panel show the detections at 610 MHz for the observations on 12^{th} August, 2011.

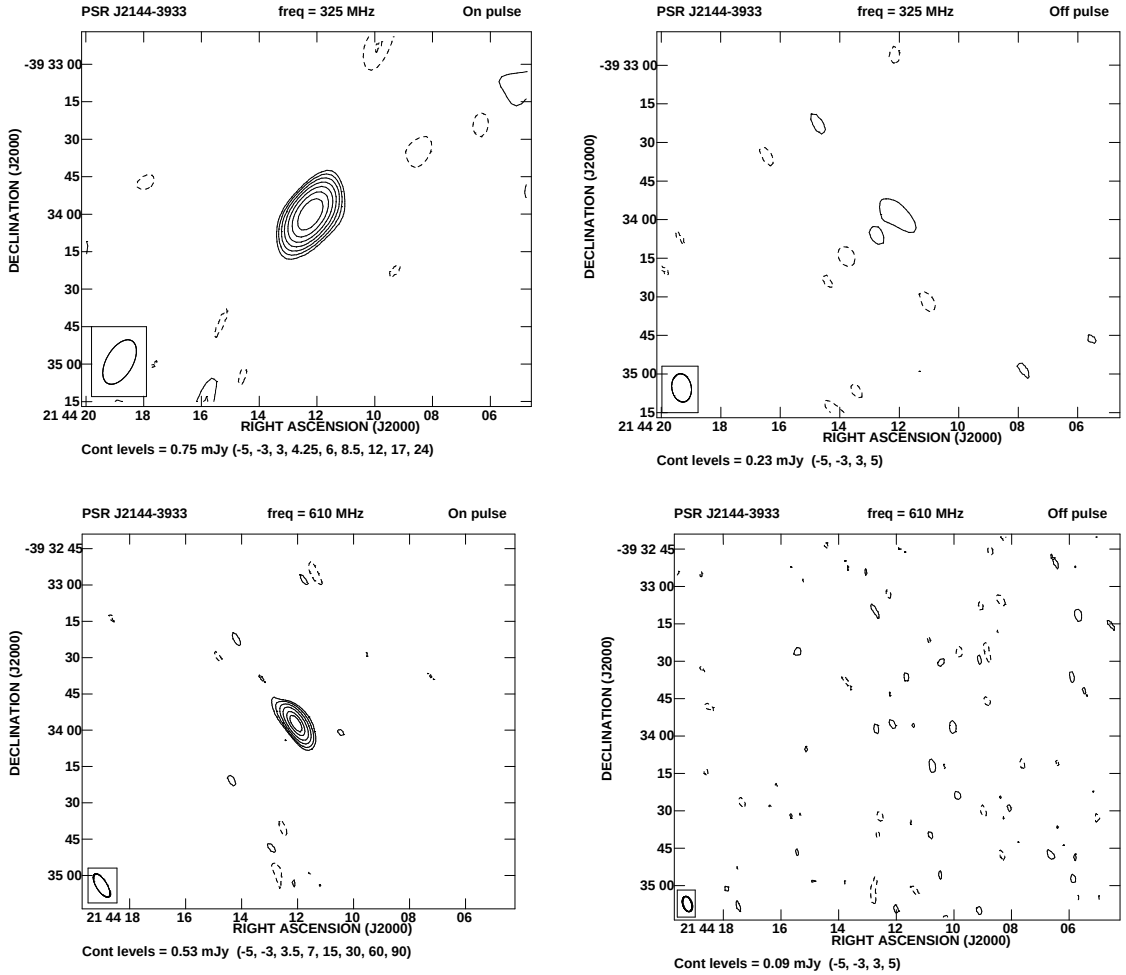

Figure 3.7 The figure show the contour maps for the on pulse (left panel) and off pulse (right panel) maps for the pulsar J2144–3933. The top panel show the observations at 325 MHz carried out on 15^{th} August, 2011. The bottom panel show the corresponding observations at 610 MHz on the 25^{th} of July, 2011. As is evident from the off-pulse images there is no discernible emission making this pulsar the only one in our sample without detected off-pulse emission.

orders of magnitude lower than the typical PWN sizes, a PWN origin can be discounted. Further a wide range of studies (Weiler & Sramek 1988) suggest that PWNe observed in the radio frequencies between 100 MHz to 10 GHz, are usually characterized by a flat radio spectral index α in the range $0 > \alpha >$ -0.5 (where $S \sim \nu^{\alpha}$). The spectrum presumably reflects the energy distribution of the injected particles from the pulsar. In some older PWNe the spectrum might steepen somewhat, like in PWNe DA495 (Kothes et al. 2008) where the spectrum steepen to $\alpha = -0.87$ above 1.3 GHz as a result of synchrotron aging. In contrast to PWNe the pulsed emission is the coherent radio emission arising due to relativistically streaming charged particles in strong magnetic field with the observed average $\alpha \sim$ –1.8 (Maron et al. 2000). Although in some examples the spectra might show breaks and turnovers (like GPS pulsars with turn over in spectra at GHz frequency range, see Kijak et al. (2011), also see spectra of B2045–16, figure 3.14), mostly they are consistent with a steep power law spectra and a very low frequency turnover (around 100 MHz and below). Based on our current understanding, any emission originating close to the pulsar magnetosphere and with spectral index which is not an inverted power law with relatively flat spectral index ($\alpha \geq$ -0.5) is unlikely to be due to PWNe.

3.3.1 Particle densities in PWNe

The confinement of the relativistic wind from pulsars generates PWNe which are luminous across the electromagnetic spectrum in synchrotron, inverse compton, and optical line emission from the shocked regions. All known PWNe seen around radio pulsars have spin-down luminosities $\dot{E} \geq 10^{34}$ erg s^{-1}. They all appear to be young and, with the exception of PSR B0906–49 (Gaensler et al. 1998), are associated with Supernova Remnant (SNR). Two classes of PWNe can be formed in the absence of associated SNR: one, where the pulsar wind is confined by the density of the ISM, known as static PWN; and the other, where the wind is confined by the ram pressure of motion of the pulsar through the ISM, called bow-shock nebula. The pulsars in our sample are not associated with SNRs.

The efficiency factor ϵ_R is defined as the ratio of the radio bolometric luminosity

(L_R) of a PWN to the spin-down energy ($\dot{E}$) of the pulsar $L_R = \epsilon_R \dot{E}$. If we assume a typical PWNe spectral index of $\alpha \sim$ –0.3 its radio luminosity between 10 MHz and 10 GHz is given by $L_R = 3.06 \times 10^{28}\ d_{kpc}^2 S_{mJy}$ erg s^{-1}, where d_{kpc} is the distance to the PWN in kpc and S_{mJy} is the integrated flux of PWN at 325 MHz in mJy. Using the measured flux density (table 3.2), source distance and the spin down energies (table 3.1) we calculate efficiency factors for the off-pulse emission in our sample to be: 2×10^{-2} for B0525+21, 2×10^{-3} for B2045–16, 5×10^{-3} for B1237+25, 4×10^{-4} for B0834+06 and 0.35 for B0320+39. These ϵ_R values are much higher than those of previously known PWNe (typical $\epsilon_R \leq 10^{-4}$; see Frail & Scharringhausen (1997); Gaensler et al. (2000) for a discussion).

Static PWN The relativistic particles and Poynting flux emanating from the pulsar, at rest relative to the ISM, will drive through the ambient medium a shock of radius R_s given by (Arons 1983)

$$R_s = \left(\frac{\dot{E}}{4\pi\rho_o}\right)^{1/5} t^{3/5} \tag{3.1}$$

The velocity of the shock front is given by

$$\dot{R}_s = \frac{3}{5}\left(\frac{\dot{E}}{4\pi\rho_o t^2}\right)^{1/5} = 3.3\left(\frac{\dot{E}_{31}}{t_6^2 n_{0.01}}\right)^{1/5} \text{ km s}^{-1} \tag{3.2}$$

Here $\rho_o = m_H n$, where m_H is the proton mass and n is the particle density of the ISM. Using eq.(3.1) the required particle density for a PWN is

$$n = 5.35 \times 10^{11}\left(\frac{\dot{E}_{31} t_6^3}{R_{0.01}^5}\right) \text{ cm}^{-3} \tag{3.3}$$

where $\dot{E}_{31}$ is the spindown power in units of 10^{31} erg s^{-1}, t_6 is the age in units of 10^6 yr, $R_{0.01}$ is the radius of PWN in units of 0.01 pc and $n_{0.01}$ is the ISM density in units of 0.01 cm^{-3}. In the present exercise the size upper limit of PWNe in our targets is specified by the synthesized beam (telescope resolution $\sim$ 0.02 pc) since the off-pulse emission is unresolved in all the pulsars. Using eq.(3.3) and values in tables 3.1 we determined the ISM density required to drive a PWN as: $\sim 3 \times 10^9$ cm^{-3} for B0525+21, $\sim 10^{12}$ cm^{-3} for B2045–16, $\sim 2 \times 10^{13}$ cm^{-3} for B1237+25, $\sim 9 \times 10^{11}$

cm^{-3} for B0834+06 and $\sim 3 \times 10^{12}$ cm^{-3} for B0320+39. The particle densities are much higher than typical ISM densities of ~ 0.03 cm^{-3}, suggesting that these pulsars are too weak and old to power a static PWN through the ISM. Since our estimate of the sizes of the nebulae are upper limits the particle density estimates are lower limits.

Bow Shock PWN This requires the shock velocity ($\dot{R}_s$) to be much smaller than the pulsar transverse velocity (V_{PSR}). The typical ISM density of 0.03 cm^{-3} in equation (3.2) yields $\dot{R}_s$ values for the pulsars to be: ~ 2.8 km s^{-1} for B0525+21, ~ 2.5 km s^{-1} for B2045–16, ~ 0.8 km s^{-1} for B1237+25, ~ 2.9 km s^{-1} for B0834+06 and ~ 0.3 km s^{-1} for B0320+39. The $\dot{R}_s$ values are indeed much smaller than the V_{PSR} listed in table 3.1. The radius of the shock is given by (Frail & Scharringhausen 1997)

$$R_{BS} = \left(\frac{\dot{E}}{4\pi c \rho_o V_{PSR}^2} \right)^{1/2} \tag{3.4}$$

From equation 3.4 the particle density required to sustain a bow shock PWN is

$$n = 1.67 \times 10^{-4} \left(\frac{\dot{E}_{31}}{R_{0.01}^2 V_{100}^2} \right) \text{cm}^{-3} \tag{3.5}$$

where $\dot{E}_{31}$ is the spin-down power in units of 10^{31} erg s^{-1}, $R_{0.01}$ is the radius of PWN in units of 0.01 pc and V_{100} is the velocity of the pulsar through the ISM in units of 100 km s^{-1}. The required ISM densities for the pulsars are: $\sim 5{\times}10^{-6}$ cm^{-3} for B0525+21, $\sim 8{\times}10^{-6}$ cm^{-3} for B2045–16, $\sim 10^{-6}$ cm^{-3} for B1237+25, $\sim 9{\times}10^{-5}$ cm^{-3} for B0834+06 and $\sim 7{\times}10^{-8}$ cm^{-3} for B0320+39. These values are 2–4 orders of magnitude lower than the typical ISM density. This implies that the pulsars are too weak to drive a bow shock nebula of the size corresponding to the telescope resolution. However, a bow shock interpretation can be salvaged if the nebulae are 1–2 orders of magnitude smaller.

We conclude from the above studies that identifying the detected off-pulse emission with PWNe results in unrealistic values of the ISM particle density. This is not surprising since the selected sample consists of middle aged and old pulsars which are not known to be associated with PWNe.

3.3.2 Pulsar Flux Variation

We are interested in determining the spectral index of off-pulse emission based on our observations at 325 and 610 MHz. Spectral index determination requires robust flux estimates which is often difficult for pulsars. The measured pulsar flux is time variant due to both intrinsic and extraneous effects. The intrinsic variations occur in timescales of microseconds to several minutes manifesting as microstructures in single pulses, drifting subpulses, nulling, mode changing, etc. However the profile of a pulsar obtained averaging 2500–3000 pulses is relatively stable (Rathnasree & Rankin 1995). The pulsar flux is also affected by the inhomogeneities in the ISM leading to diffractive interstellar scintillations (DISS) and refractive interstellar scintillations (RISS). The DISS manifests as temporal flux variations with diffraction timescales (T_d) ranging from seconds to minutes and also as decorrelation of flux with frequency known as decorrelation bandwidth ($\Delta\nu_d$). The RISS shows variations at timescales (T_r) of days to years with a flux modulation index (m_r). These quantities scale with dispersion measure and frequency of observation typically as $T_d \propto \nu^{1.2}$, $\Delta\nu_d \propto \nu^{4.4}$, $T_r \propto \nu^{-2.2}$ and $m_r \propto \nu^{0.58}$ (Stinebring & Condon 1990). In order to determine the spectral index of the off-pulse emission it is imperative we understand its short and long term flux variations at each frequency.

PSR B0525+21 has a dispersion measure of 50.9 pc cm^{-3} and its flux has been monitored at different frequencies for several years as reported in Lorimer et al. (1995) and Stinebring et al. (2000) (see fig 3.14 for the flux at low frequencies). The long term averaging results in reduced contribution of RISS and DISS to the pulsar flux. Stinebring et al. (2000) quotes the scintillation parameters at our observing frequency 610 MHz as $T_d \sim 70$ seconds, $\Delta\nu_d \sim 230$ KHz, $m_r \sim 0.32$, $T_r \sim 4$ days. Using the scaling relations the equivalent quantities at 325 MHz are $T_d \sim 33$ seconds, $\Delta\nu_d \sim 15$ KHz, $m_r \sim 0.22$, $T_r \sim 16$ days.

Each of the GMRT observations for B0525+21 extends for about 6 to 8 hours and 16 MHz bandwidth at both 325 and 610 MHz. Any flux variations due to DISS will be greatly reduced over these scales. Due to RISS one expects 5% and 10% variation

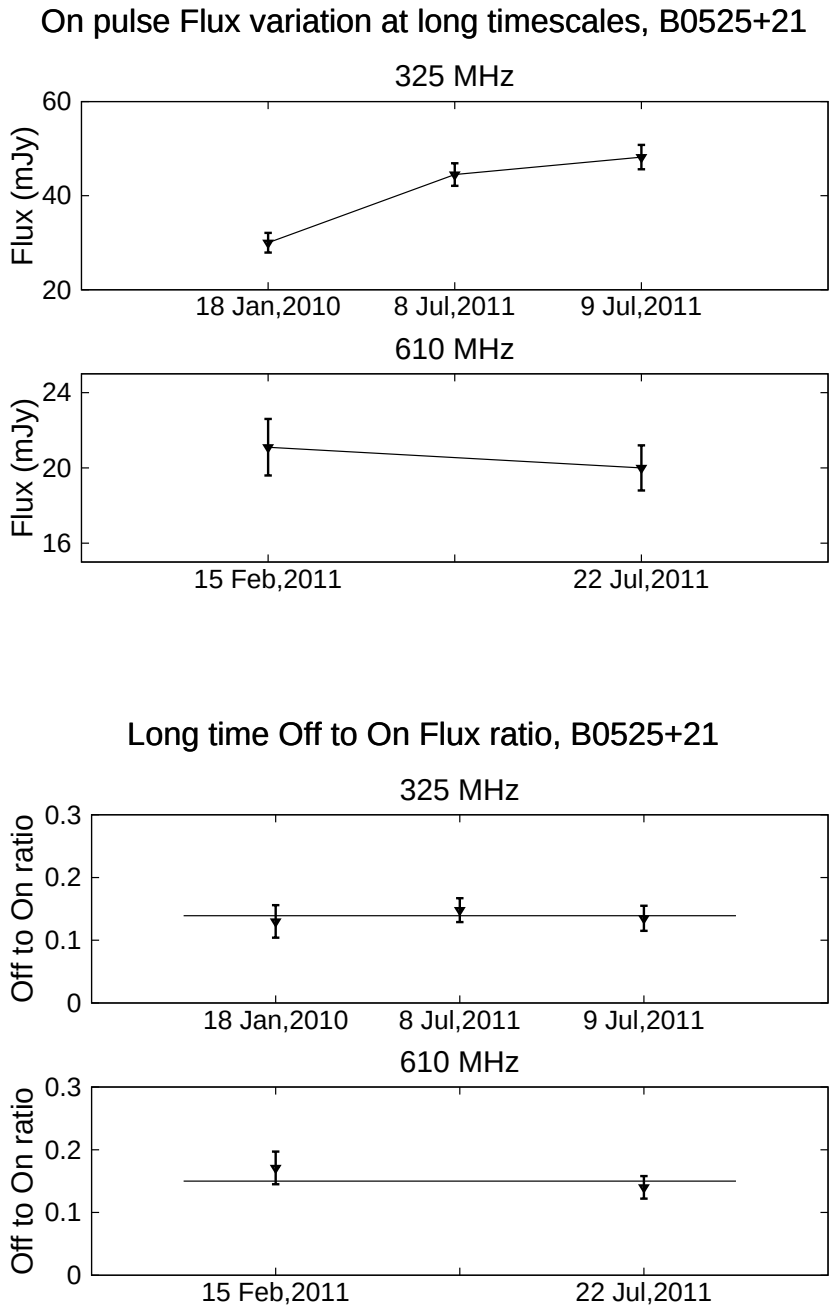

Figure 3.8 The figure show variations in the on-pulse flux and the off-pulse to on-pulse flux ratio at large timescales for PSR B0525+21 across multiple observing sessions. Each point in the plots is obtained averaging a single observing run lasting a few hours with the observations being separated by several days to months. The pulsar show a constancy in the Off-pulse to On pulse flux ratio over these timescales.

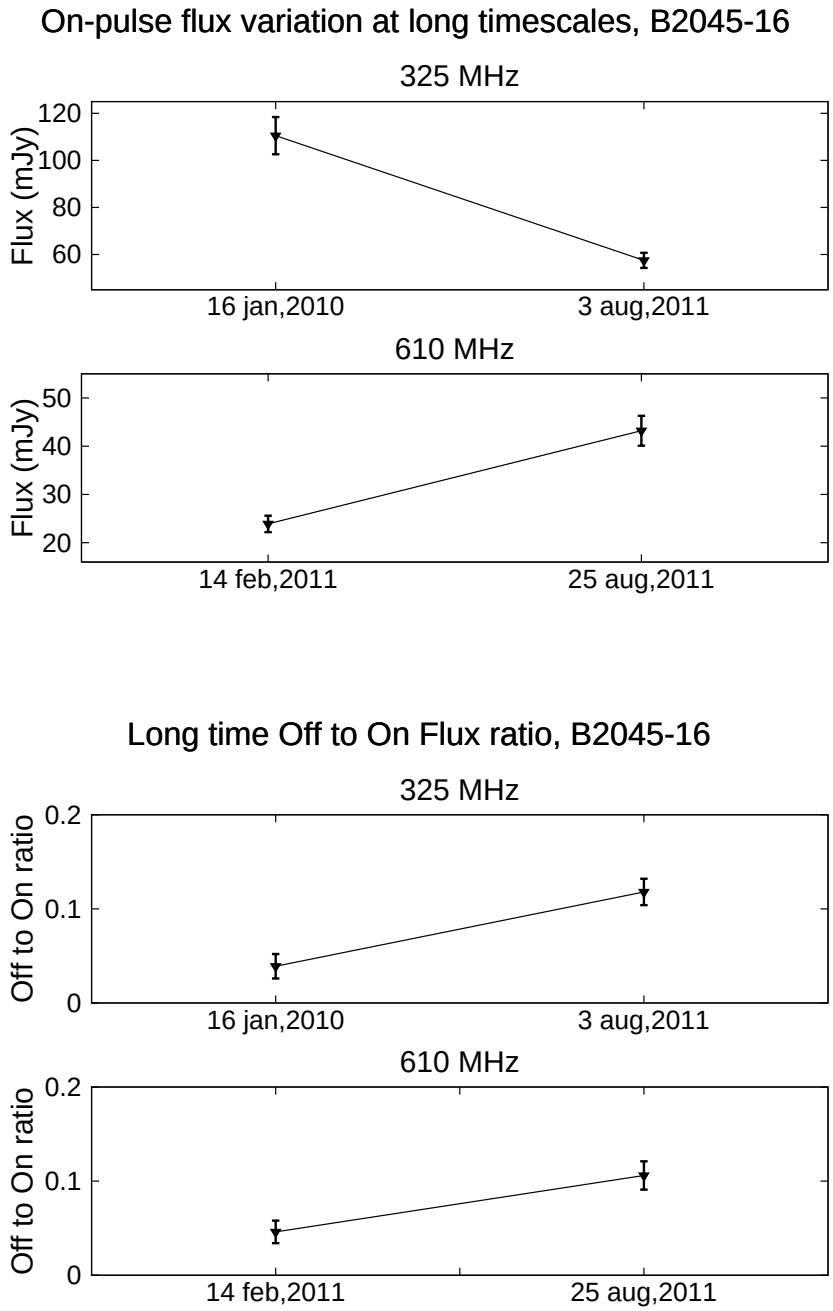

Figure 3.9 The figure show variations in the on-pulse flux and the off-pulse to on-pulse flux ratio at large timescales for PSR B2045–16 across multiple observing sessions. Each point in the plots is obtained averaging a single observing run lasting a few hours with the observations being separated by several days to months. The pulsar show an apparent variation in the Off-pulse to On pulse flux ratio.

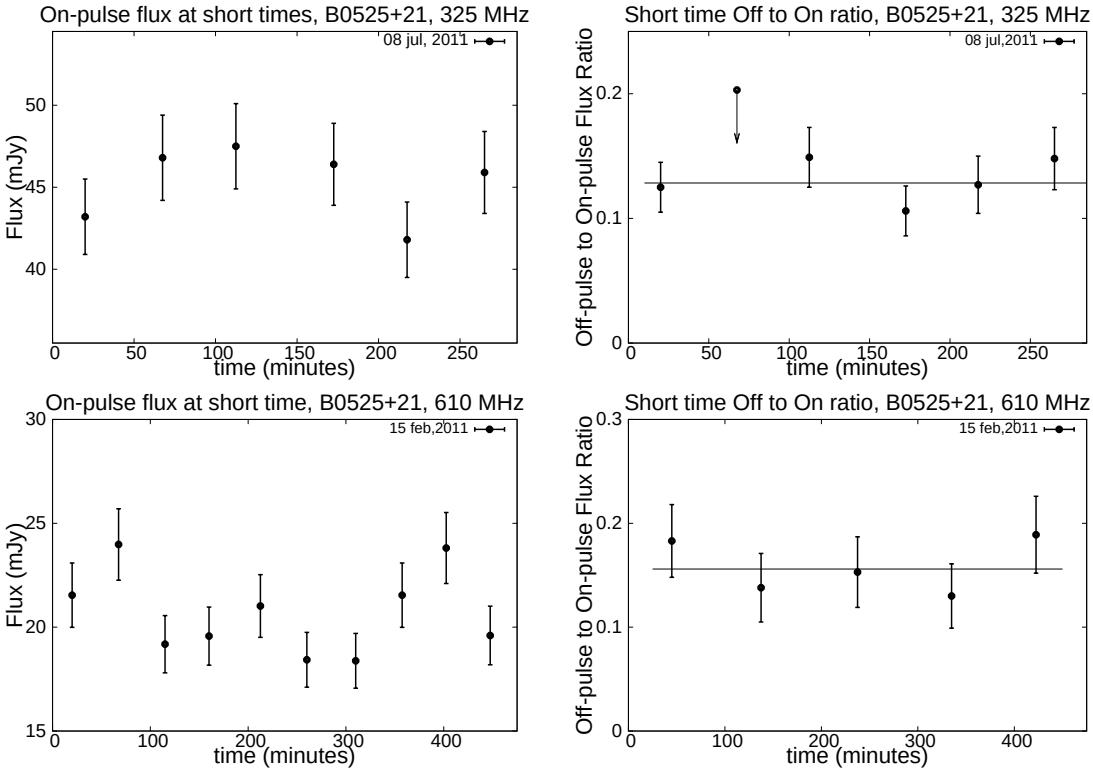

Figure 3.10 The figure show variation of the on-pulse flux (left panel) and the off-pulse to on-pulse flux ratio (right panel) at short timescales for pulsar B0525+21 at 325 MHz (top panel) and 610 MHz (bottom panel). The duration of a single observation spans several hours and the on and off-pulse fluxes were determined averaging 0.5 –1 hour at a time within a single observation. The on-pulse flux varied at short timescales (several hours) within errors of measurements and the on-pulse to off-pulse ratio remained constant at these timescales.

in flux over a single observing run at 325 MHz and 610 MHz respectively (these are comparable to the error in flux measurements and hence undetectable). In table 3.2 the average on and off-pulse flux and the off-pulse to on-pulse flux ratio during each observing session is reported. The long term flux change (about 55%) seen at 325 MHz (figure 3.8, top panel on left) is due to RISS, however the off-pulse to on-pulse flux ratio remain constant both at 325 and 610 MHz (see figure 3.8, bottom panel on left). The short term flux variations were determined by dividing a single observing session into shorter intervals (0.5 to 1 hour) and making images for each case. The on and off-pulse flux was measured for each interval and the off-pulse to on-pulse flux ratio was calculated (see figure 3.10). The short timescale flux variations were within the errors of measurement, as expected, and the off-pulse to on-pulse flux ratio was also constant.

PSR B2045–16 has a dispersion measure of 11.5 pc cm^{-3} and its long term flux has been monitored at multiple frequencies by Stinebring & Condon (1990) and Lorimer et al. (1995). Based on daily flux measurements for 43 days Stinebring & Condon (1990) quotes the scintillation parameters at 310 MHz (near our observing frequency of 325 MHz) as $T_d \sim 63$ seconds, $\Delta\nu_d \sim 288$ KHz, $m_r \sim 0.60$ and $T_r \sim 1.5$ days. Using the scaling relations the equivalent quantities at 610 MHz are $T_d \sim 134$ seconds, $\Delta\nu_d \sim 4$ MHz, $m_r \sim 0.85$ and $T_r \sim 0.5$ days.

The observations extended for 3 to 5 hours over 16 MHz bandwidth at both 325 and 610 MHz for each observing run. Any DISS related flux variations is expected to reduce due to averaging over time and frequency. However due to RISS we expect large flux variations of 110% and 40% over a single observing run at 610 and 325 MHz respectively. In table 3.2 the average on and off-pulse flux measurements and the off-pulse to on-pulse flux ratios for each observation is quoted. The long term flux variations and off-pulse to on-pulse flux ratio is shown in figure 3.9 (right panel). The pulsar flux show variation in the flux values which are expected due to RISS, however the off-pulse to on-pulse flux ratio also showed large variations at long timescales. The short timescale flux values were determined once again by dividing a single observing session into shorter intervals (0.5 to 1 hour) and making images for each

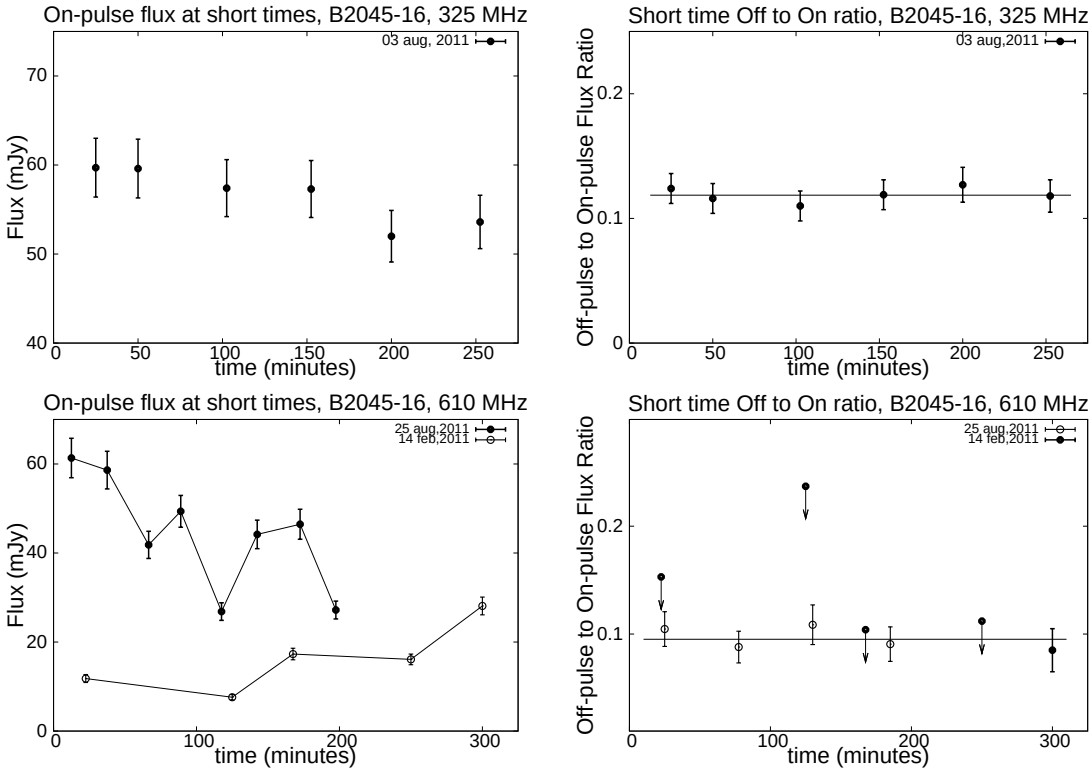

Figure 3.11 The figure show variation of the on-pulse flux (left panel) and the off-pulse to on-pulse flux ratio (right panel) at short timescales for pulsar B2045–16 at 325 MHz (top panel) and 610 MHz (bottom panel). The duration of a single observation spans several hours and the on and off-pulse fluxes were determined averaging 0.5–1 hour at a time within a single observation. The on-pulse flux variations were once again within errors at 325 MHz with the off-pulse to on-pulse flux ratio remaining constant. At 610 MHz the on-pulse flux showed large variations, however the off-pulse to on-pulse flux ratio once again remained constant at short timescales for both the observations even though they go below detection level sometimes (arrows pointing downwards show upper limit of detection). This demonstrated both the long and short timescale constancy of the off-pulse to on-pulse flux ratio for B2045–16 at 610 MHz.

case. The on-pulse flux at 610 MHz showed large variations in excess of 100% (see figure 3.11, bottom panel to the left), however the off-pulse to on-pulse flux ratio, when detected, remained at constant level for the two observations separated by months (see figure 3.11, bottom panel on right). The apparent variation of the off-pulse to on-pulse flux ratio at large timescales can be attributed to the fact that the off-pulse was below detection limit for a large fraction of the observing run resulting in under estimation of the average off-pulse flux over the entire observing run. At 325 MHz the short timescale measurements once again showed constant level of off-pulse to on-pulse flux ratio for the observation on 3 august, 2011 (see figure 3.11, top panel on right). The observation on 16 January, 2010 was affected by the telescope pointing $35'$ away from the pulsar resulting in increased noise levels at pulsar position thereby making the short interval studies impossible (the off-pulse was undetected for the short interval studies due to higher noise levels). We conclude that despite the large variation of the on-pulse flux and the apparent variation of off-pulse to on-pulse flux ratio at large timescales, the off-pulse to on-pulse flux ratios remain constant at all timescales for this pulsar.

PSR B1237+25 has a dispersion measure of 9.242 pc cm^{-3} and its long term flux has been monitored at multiple frequencies by Lorimer et al. (1995). This pulsar was monitored on 9 separate occasions within a duration of four months by Bhat et al. (1999) at 327 MHz; the studies were not greatly accurate but we use their results nonetheless to obtain indicative estimates for our observations. The scintillation parameters were $T_d \sim 439$ seconds, $\Delta\nu_d \sim 1828$ KHz, $m_r \sim 0.69$ and $T_r \sim 1.8$ days. Using the scaling relations the equivalent quantities at 610 MHz are $T_d \sim 928$ seconds, $\Delta\nu_d \sim 28$ MHz, $m_r \sim 1.0$ and $T_r \sim 0.45$ days.

This pulsar was only observed for a single session at both the frequencies thereby making it impossible to carry out long term variation analysis. In addition the off-pulse detections were very weak at 325 MHz and we were unable to detect the off-pulse emission at short intervals. However the on-pulse flux for this pulsar was sufficiently above the long time average pulsar flux (see fig 3.14), indicating the off-pulse level to be intrinsically weak at 325 MHz. We have carried out the short time flux variation

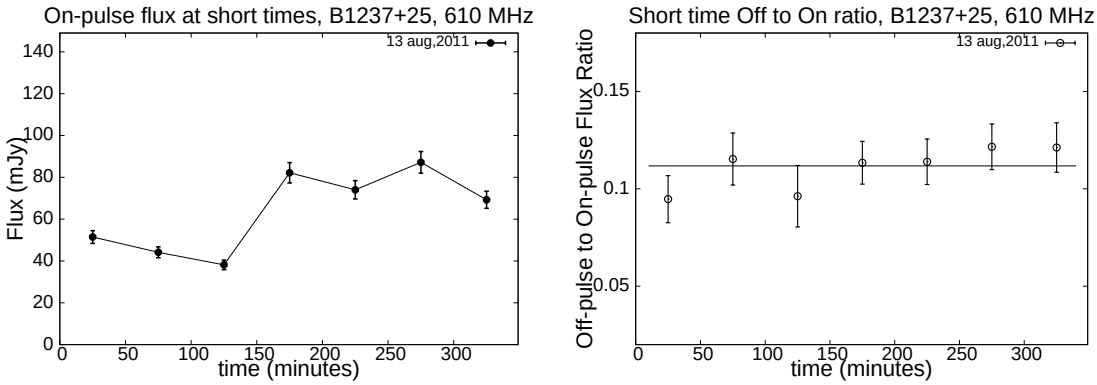

Figure 3.12 The figure show variation of the on-pulse flux (left panel) and the off-pulse to on-pulse flux ratio (right panel) at short timescales for pulsar B1237+25 at 610 MHz. The duration of a single observation spans several hours and the on and off-pulse fluxes were determined averaging $\sim$ 1 hour at a time within a single observation. The on-pulse flux showed large variations, however the off-pulse to on-pulse flux ratio once again remained constant at short timescales.

exercise at 610 MHz as shown in figure 3.12. The on-pulse flux measured for a duration of 6 hours, undergoes a large variation by a factor of 2 which is within the expected levels of variation due to RISS. The off-pulse to on-pulse flux ratio once again remain constant for the duration of the observation.

PSR B0834+06 has a dispersion measure of 12.889 pc cm^{-3} and its long term flux has been monitored at multiple frequencies by Lorimer et al. (1995). This pulsar was monitored on 93 separate occasions within a duration of two and half years by Bhat et al. (1999) at 327 MHz. The scintillation parameters obtained were $T_d \sim$ 390 seconds, $\Delta\nu_d \sim$ 454 KHz, $m_r \sim 0.40$ and $T_r \sim$ 3.9–6.6 days. Using the scaling relations the equivalent quantities at 610 MHz are $T_d \sim$ 824 seconds, $\Delta\nu_d \sim$ 7 MHz, $m_r \sim 0.57$ and $T_r \sim$ 1.0–1.7 days.

As in the previous case the pulsar was only observed for a single session at both the frequencies thereby making it impossible to carry out long term variation analysis. The off-pulse detections were once again very weak at 325 MHz to undertake short interval studies. However the on-pulse flux for this pulsar was also sufficiently above

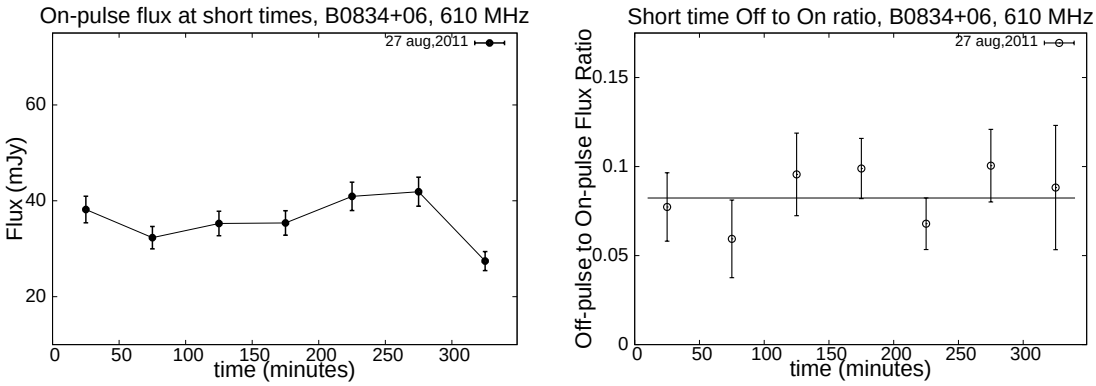

Figure 3.13 The figure show variation of the on-pulse flux (left panel) and the off-pulse to on-pulse flux ratio (right panel) at short timescales for pulsar B0834+06 at 610 MHz. The duration of a single observation spans several hours and the on and off-pulse fluxes were determined averaging $\sim$ 1 hour at a time within a single observation. The on-pulse flux showed significant changes, however the off-pulse to on-pulse flux ratio once again remained constant at short timescales.

the long time average pulsar flux (see fig 3.14), indicating the off-pulse level to be intrinsically weak at 325 MHz. We have carried out the short time flux variation exercise at 610 MHz as shown in figure 3.13. The on-pulse flux measured for a duration of 5.5 hours, undergoes large variations within expectations from RISS. The off-pulse to on-pulse flux ratio once again remain constant for the duration of the observation.

PSR B0320+39 The off-pulse emission detected in this pulsar were too weak to carry out short time interval analysis. However, the fraction of the off-pulse to on-pulse flux ratio for this pulsar were commensurate with the other pulsars indicating that the conclusions of the previous cases can be extended to this pulsar as well.

3.3.3 Upper Limits to Emission Heights of off-pulse

The off-pulse to on-pulse flux ratio as demonstrated above remains constant at all timescales for the pulsars in our sample. This signifies that the timescales of refractive scintillations for the off-pulse is similar to that of the main pulse, which readily puts

Table 3.3 Upper limits to emission region of off-pulse emission.

Pulsar	$Pc/2\pi$	D_r^{325}	D_r^{610}	θ_{max}^{325}	θ_{max}^{610}	R_{max}^{325}	R_{max}^{610}
	km	km	km	$''$	$''$	km	km
B0525+21	1.8×10^5	1.6×10^8	4.0×10^7	1.2×10^{-6}	2.5×10^{-6}	4.1×10^5	8.6×10^5
B2045–16	0.9×10^5	3.3×10^7	1.1×10^7	5.7×10^{-6}	9.3×10^{-6}	8.2×10^5	13.2×10^5
B1237+25	0.7×10^5	3.6×10^7	0.9×10^7	5.2×10^{-6}	1.1×10^{-5}	6.6×10^5	13.9×10^5
B0834+06	0.6×10^5	3.8×10^7	1.1×10^7	4.9×10^{-6}	9.4×10^{-6}	5.3×10^5	10.2×10^5

a constraint on the size of the emitting region of the off-pulse with respect to the on-pulse. If we assume a thin screen approximation, i.e, the refractive scintillations is due to a thin lens (0.1–1 % of the thickness of intervening medium) placed a fractional distance β ($\beta = D_s/D$, where D_s is separation between pulsar and lens and D the distance between pulsar and observer) from the pulsar, the refractive timescale is given as:

$$T_r = \frac{D_r}{V_{trans} \times (1-\beta)} \tag{3.6}$$

where D_r is the diameter of the lens and V_{trans} the transverse velocity of the pulsar in the sky plane with respect to observer. The similar refractive timescales imply the on-pulse and off-pulse emission is unresolved with respect to the lens putting an upper limit to the separation between the the on and off-pulse emitting regions with the maximum angular separation given as $\theta_{max} \sim \lambda/D_r$.

Using the known properties of the pulsars (table 3.1) and assuming the lens lies mid way between the pulsar and observer ($\beta = 0.5$) we calculate the diameter of the lens (D_r) for each pulsar using eq.(3.6). This is further used to determine the upper limits to the angular size of the emitting region (θ_{max}). Finally the physical size of the maximum emitting region (R_{max}) is calculated using θ_{max} and distance to the pulsars. The maximum emitting region (which is also the maximum separation between the on-pulse and off-pulse emitting regions) is constrained to be a few micro arcseconds (θ_{max}). This further implies that the off-pulse emission is constrained by the refractive scintillations to originate within an order of magnitude of the light cylinder radius ($Pc/2\pi$). The detailed estimates constraining the emission heights of off-pulse emission for the four pulsars B0525+21, B2045–16, B1237+25 and B0834+06

Table 3.4 The spectral index of off-pulse emission.

Pulsar	α_{ON}	$(\frac{Off}{On})_{325}$	$(\frac{Off}{On})_{610}$	α_{OFF}
B0525+21	-1.5 ±0.1	0.139±0.012	0.150±0.015	-1.38±0.28
B2045–16	-0.95±0.12	0.118±0.014	0.106±0.015	-1.12±0.33
B1237+25	-1.9 ±0.2	0.015±0.003	0.109±0.009	1.25±0.47
B0834+06	-3.3 ±0.6	0.019±0.004	0.125±0.014	-0.31±0.67
B0320+39	-2.9 ±0.1	0.120±0.010	0.107±0.011	-3.08±0.51

is shown in table 3.3. This is more than ten orders of magnitude lower than the typical size of a PWN. We use these empirical estimates as a strong indication of the off-pulse emission originating within the pulsar magnetosphere.

3.3.4 Spectral Index of off-pulse Emission

The off-pulse flux would vary with time due to effects of scintillations as discussed earlier and hence would require continuous monitoring over a long time to determine their average flux values. However, we have established that the off-pulse to on-pulse flux ratio remain constant at all timescales. This enables us to determine the off-pulse spectral index between 325 MHz and 610 MHz provided the on-pulse spectral index is known and both the emissions follow a power law spectrum. The off-pulse spectral index is given as:

$$\alpha_{OFF} = \alpha_{ON} + \frac{log(\rho_1/\rho_2)}{log(\nu_1/\nu_2)} \tag{3.7}$$

where α_{OFF} and α_{ON} are the off-pulse and on-pulse spectral indices respectively and ρ the off-pulse to on-pulse flux ratio at frequency ν. The error in α_{ON} is obtained from the error in fitting the on-pulse data while the error in α_{OFF} is determined using the error in estimating both α_{ON} and ρ.

B0525+21 The main pulse spectrum between 400 MHz and 1.6 GHz is well known (Lorimer et al. 1995) and shown in figure 3.14 (top panel on the left), which is well approximated by a single power law spectrum with spectral index –1.5 (linear fit in

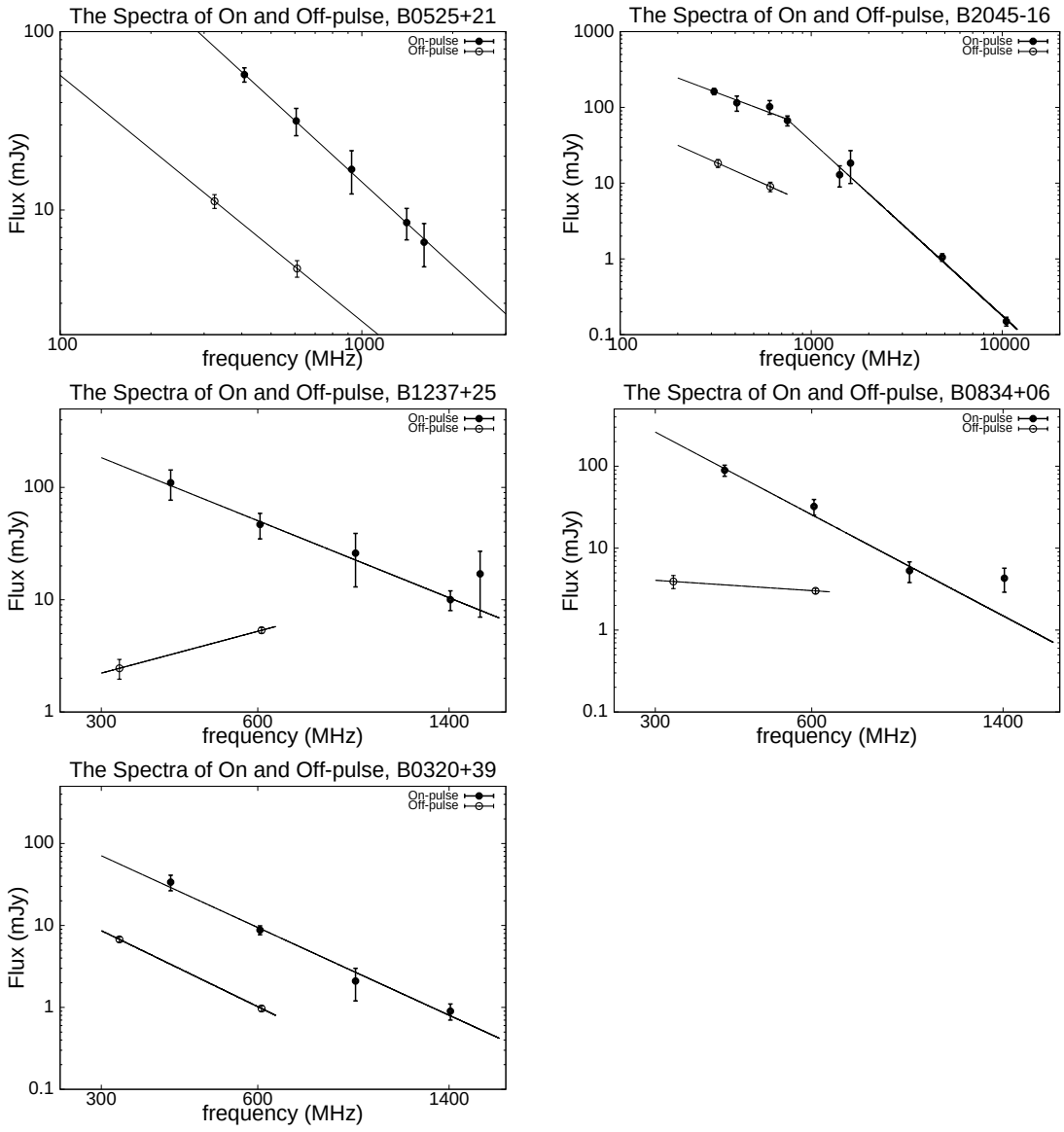

Figure 3.14 The figure show low frequency spectral nature of the on-pulse flux and the off-pulse spectra between 325 MHz and 610 MHz for the five pulsars B0525+21 (top left), B2045–16 (top right), B1237+25 (middle left), B0834+06 (middle right) and B0320+39 (bottom left)

fig 3.14). The off-pulse spectral index is calculated using eq.(3.7) and the off-pulse to on-pulse flux ratios given in table 3.4. The off-pulse spectral index turns out to be –1.4 which is pretty steep and comparable to the on-pulse spectra.

B2045–16 The spectrum for the on-pulse is determined from the literature (Lorimer et al. 1995; Maron et al. 2000) over the frequency range 300 MHz to 10 GHz. In this case however the entire spectral range is not approximated by a single power law, with a clear break in the spectrum seen around 750 MHz (see figure 3.14, top panel on the right). We determine the spectral index in this case by fitting two separate power laws above and below the break with spectral indices of –2.3 for the high frequency range and –0.95 for the low frequency regime. Our observations at 325 and 610 MHz lie in the low frequency range and we use this to calculate the spectral index of off-pulse emission using eq.(3.7) which turns out to be –1.1. The off-pulse spectra is steeper than the on-pulse spectra at the low frequency range.

B1237+25 The spectrum between 400 MHz and 1.6 GHz is once again determined using previously measured values (Lorimer et al. 1995) and is shown in figure 3.14 (middle panel on the right). The on-pulse spectra is well approximated by a single power law with a spectral index of –1.9. The off-pulse spectra on the other hand show a turnover between 325 MHz and 610 MHz with a spectral index of +1.25. This does not appear to be a result of the instrument unable to detect missing flux as mentioned earlier but an intrinsic nature of the off-pulse emission in this pulsar.

B0834+06 The spectrum of the pulsar between 400 MHz and 1.4 GHz was determined using flux values from literature (Lorimer et al. 1995). However, the low frequency spectra was not well determined with large spread in the flux values and hence large errors in the fitted spectral index. The on-pulse spectra determined was very steep with a spectral index of –3.3. The off-pulse spectra was vastly different from the on-pulse spectra with a spectral index of –0.3. Due to the large error in the on-pulse spectra it was difficult to say whether there was a turn over in the off-pulse spectra. However, it is clear that the off-pulse spectra show considerable flattening

between 325 MHz and 610 MHz for this pulsar.

B0320+39 The spectrum of the pulsar between 400 MHz and 1.4 GHz was once again determined using available data (Lorimer et al. 1995). The on-pulse spectra with a single power law fit was relatively steep spectrum with spectral index of –2.9. The off-pulse spectra was also very steep and closely followed the on-pulse spectra with a spectral index of –3.1 which is the steepest spectra in our sample.

3.4 Discussion

We have discovered radio emission in the off-phase of long period pulsars, termed off-pulse emission, located far away from the typical main pulse in the pulsar profile. Unlike the main pulse emission which sticks out as a pulsed component, the off-pulse emission so far remains undetected as a temporal structure in the pulsar profile. The off-pulse emission have been detected by averaging a certain section of the pulsar profile away from the pulsed main pulse and measuring the flux value using deep interferometric imaging. The off-pulse emission seem to be a constant background emission in the temporal profile, however, a bin by bin imaging analysis needs to be implemented in order to uncover any temporal structure in the off-pulse and form part of our future endeavours in off-pulse studies.

We have observationally constrained the off-pulse emission to be originating within the pulsar magnetosphere using scintillation studies of on and off-pulse flux. The spectral index of off-pulse emission seem to be steep for the relatively longer period pulsars (B0525+21, B2045–16 and B0320+39) while it becomes flat spectrum (B0834+06) and even shows inversion (B1237+25) for the shorter period pulsars. At this stage we should desist from reading too much into this as we are yet to understand the location and nature of the off-pulse emission within the pulsar magnetosphere.

The off-pulse emission appear to be a completely new and hitherto undetected radio emission from pulsars. We have shown the off-pulse emission to be magnetospheric in origin and even if we assume the emission to originate at the outermost extremity of the magnetosphere, i.e, the light cylinder, the brightness temperature

is greater than 10^{18} K. This strongly suggests a coherent radio emission mechanism responsible for the off-pulse emission which leads to the next important question as to where and how does this off-pulse coherent emission originate in the pulsar magnetosphere? In most theories the radio emission is excited due to development of plasma instabilities in the outflowing plasma moving along dipolar magnetic fields as discussed in chapter 1. The location of off-pulse emission in the pulsar profile indicate the emission to originate higher up in the pulsar magnetosphere compared to the on-pulse which originate around heights of 500 km from the neutron star surface. In the next chapter we investigate a coherent emission mechanism which develops at the outer magnetosphere called the cyclotron-resonance instability and look at its compatibility with the detected off-pulse emission.

Chapter 4

Cyclotron Resonance Instability

4.1 Radio emission in pulsars

In this section we recapitulate the conditions in the pulsar magnetosphere leading to radio emission as introduced in chapter 1. The neutron star, radius $R_S = 10^6$ cm, is characterized by a strong magnetic field B_s, which is highly multipolar near the stellar surface (Mitra et al. 1999b). The dipole part of the surface magnetic field is given as $B_d = 3.2{\times}10^{19}(P\dot{P})^{1/2}$ G, here P and $\dot{P}$ are the rotation period and period derivative, respectively, $B_s = bB_d$ and $b \gg 1$. The rotating magnetic field gives rise to an electric field (E), and in order to maintain the force-free condition ($E.B = 0$) a corotating charge-separated magnetosphere, with density $n_{GJ} = -(\Omega.B)/2\pi ce$ (Goldreich & Julian 1969), surrounds the neutron star. The force-free condition breaks down at the light cylinder, $R_{LC} = c/\Omega \approx 4.8 \times 10^9 P$ cm, beyond which the charges no longer corotate. Above the polar regions there is an outflow of charges and the magnetosphere slowly recedes, resulting in a charge depleted vacuum gap with a large potential drop across it. In the gap region e^-e^+ pairs are created by pair production involving background γ-ray photons interacting with the high magnetic field. The pairs so created are accelerated in opposite directions to relativistic energies by the large potential difference across the gap. These highly energetic particles produced in the vacuum gap emit further γ-rays via curvature radiation and/or inverse comp-

ton scattering, giving rise to a cascade of e^-e^+ pairs which discharges the potential difference across the gap. The height of the gap region h stabilizes at the mean free path length of the γ-ray photons and is given by (Ruderman & Sutherland 1975) as:

$$h = 5 \times 10^3 \; b^{-4/7} \; P^{1/7} \dot{P}_{-15}^{-2/7} {\rho_6}^{2/7} \quad \text{cm} \tag{4.1}$$

Here $\rho_6 = \rho/10^6$ cm, where ρ is the radius of curvature of the multipolar field lines in the gap region. The potential difference across the vacuum gap is $\Delta V = \Omega B h^2/c$ which, according to (Ruderman & Sutherland 1975), reduces to:

$$\Delta V = 5 \times 10^9 \; b^{-1/7} P^{-3/14} \dot{P}_{-15}^{-1/14} {\rho_6}^{4/7} \quad \text{Volts.} \tag{4.2}$$

The discharge of the vacuum gap takes place through a series of sparks which deposit highly energetic singly charged primary particles beyond the gap region. According to the "sparking" model (Gil & Sendyk 2000) the typical diameters of the sparks are $\sim h$. The primary particles have maximum energies specified as $\gamma_b = e\Delta V/mc^2 \sim 3{\times}10^6$ for typical pulsar parameters. Due to partial shielding of the acceleration region by thermionic ions, the gap potental drops to $\Delta V = \eta \Delta V_{max}$ (Gil et al. 2003), and the particle densities are given as $n_b = \eta n_{GJ}$, where $0 < \eta < 1$ is the screening factor. Once outside the gap the primary particles cease to accelerate but continue emitting curvature radiation with characteristic photon energies given by $\hbar\omega_c = \frac{3}{2}\gamma_b^3 \hbar c/\rho$. The photons continue pair production resulting in a cloud of secondary e^-e^+ plasma with typical energies $\gamma_p = \hbar\omega_c/2mc^2 \sim$ 10-1000 and density $n_p = \chi n_{GJ}$, where $\chi \sim 10^4$ is the Sturrock multiplicative factor (Sturrock 1971). The spark discharge timescale in the vacuum gap is a few tens of μseconds, and this results in overlapping clouds of outflowing secondary plasma penetrated by the primary particles. Thus to summarize, the pulsar magnetosphere above the polar cap consists of a series of secondary plasma clouds, each corresponding to a "spark" in the vacuum gap, penetrated by primary particles, moving outward along the magnetic field.

The principal predicament in explaining the radio emission from pulsars is its coherent nature evidenced by high brightness temperatures. This presages the presence of a bunching mechanism resulting in a large number of charged particles radiating

simultaneously in phase. There are two possible regions where instabilities in the outflowing plasma can lead to charge bunching. In the first case particles of different momenta in the overlapping clouds undergo two stream instability giving rise to strong electrostatic Langmuir waves around heights of $\sim 50R_S$, here R_S is radius of neutron star. The Langmuir waves are modulationally unstable, and nonlinear plasma processes results in bunching of charge separated solitons (Melikidze et al. 2000). The radio emission from the main pulse originates around these heights (e.g. Cordes 1978; Blaskiewicz et al. 1991; Rankin 1993a; Kijak & Gil 1997, 2003; Malov & Suleimanova 1998; Mitra & Deshpande 1999; Gangadhara & Gupta 2001; Mitra & Li 2004; Krzeszowski et al. 2009) and is explained as curvature radiation from the charge separated solitons (Melikidze et al. 2000; Gil et al. 2004; Mitra et al. 2009). In the second case the naturally developing electromagnetic modes in the clouds of secondary plasma undergo negative absorption from the highly energetic primary paricles via the cyclotron resonance instability (Kazbegi et al. 1987, 1991; Lyutikov et al. 1999) with the possibility of coherent radio emission. Such an emission near the light cylinder will likely be spread out over a large part of the pulsar's rotation cycle and is a likely source of off-pulse emission. In the next sections we examine the conditions necessary for the development of the cyclotron resonance instability near the light cylinder and its viability in explaining the detected off-pulse emission.

4.2 Conditions for emission near the light cylinder

The magnetic field near the outer magnetosphere becomes strictly dipolar field due to the much faster decay of the higher multipoles. The magnetic field and plasma density, within the dipolar structure, decrease with distance R from neutron-star surface as $(R_S/R)^3$. The high magnetic field near the neutron star surface constrains the outflowing plasma to move along the field lines. This condition is relaxed near the light cylinder where the magnetic field is much weaker and the particles are able to exhibit drifting. Within the outflowing plasma various electromagnetic (EM) propagating modes can be generated. The extra-ordinary mode is one such example which is a transverse EM wave capable of propagating in the plasma and escaping

the plasma boundary. The dispersion relation for the extra-ordinary waves is given as (Kazbegi et al. 1991):

$$\omega = kc(1-\delta), \quad \delta = \frac{\omega_p^2}{4\omega_B^2\gamma_p^3} \tag{4.3}$$

Here ω_B is the cyclotron frequency and ω_p the plasma frequency.

$$\omega_B = \frac{eB}{m_e c}; \quad \omega_p = \left(\frac{4\pi n_p e^2}{m_e}\right)^{1/2} \tag{4.4}$$

The amplitude of the extra-ordinary wave should grow as it propagates through the plasma if it is to escape the plasma region. This amplification is provided by the high energy primary plasma through the cyclotron resonance instability. The primary particles near the light cylinder are capable of resonating with the extra-ordinary wave. The particles in addition also undergo curvature drift with a drift velocity u_d $= \gamma c^2/\omega_B\rho$, ρ being the radius of curvature of the field lines. The resonance condition for the instability is given as:

$$\omega(\mathbf{k}) - k_\parallel v_\parallel - k_\perp u_d + \frac{\omega_B}{\gamma} = 0. \tag{4.5}$$

Here $k_\parallel$ and $v_\parallel$ are the wave vector and particle velocity parallel to the field lines and $k_\perp$ the wave vector perpendicular to the field lines. The dispersion relation [eq.(4.3)] and the resonance condition [eq.(4.5)] gives the resonance frequency to be

$$\omega_0 = \frac{\omega_B}{\gamma_{res}\delta}. \tag{4.6}$$

Here $\gamma_{res} = \gamma_b$. In addition to the excitation of resonance frequency, another factor that is crucial for the emergence of the emission is the growth rate Γ specified as (Kazbegi et al. 1991):

$$\begin{aligned} \Gamma &= \pi\frac{\omega_{p,res}^2}{\omega_0\gamma_T} && u_d^2/2c^2\delta \ll 1 \\ \Gamma &= \pi\frac{\omega_{p,res}^2}{2\omega_0\gamma_T}\frac{u_d^2}{c^2\delta} && u_d^2/2c^2\delta \gg 1 \end{aligned} \tag{4.7}$$

γ_T is the thermal spread in the secondary plasma distribution. The necessary conditions for the electromagnetic emission due to the cyclotron resonance instability are:

1. The growth factor should be large $\Gamma\tau > 1$, where $\tau \sim R_{LC}/c = P/2\pi$ is the growth time, i.e. the duration before the waves escape the light cylinder.

2. The resonance frequency should not exceed the damping frequency, $\omega_0 < \omega_1 = 2\gamma_p\omega_B$.

4.2.1 Parametric representation

We assume the emission to manifest at the light cylinder, $R_{LC} = c/\Omega \approx 4.8\times10^9 P$ cm, ensuring maximum growth of the resonant waves. We determine a representation of the conditions explained above in terms of the basic parameters of the pulsar and the outflowing plasma. The magnetic field is given as:

$$\begin{aligned} B &\approx 10^{12}(P\dot{P}_{-15})^{1/2}(R_S/R)^3 \ \ G \\ &\approx 9\ (\dot{P}_{-15}/P^5)^{1/2} \ \ G \end{aligned} \tag{4.8}$$

Here $R_S \sim 10^6$ cm and B is represented at the light cylinder. The Goldreich-Julian density on the neutron star surface is given as

$$\begin{aligned} n_{GJ} &= -(\mathbf{\Omega}\cdot\mathbf{B})/2\pi ce \\ &\approx 6.9\times10^{10}\ (\dot{P}_{-15}/P)^{1/2} \ \ \mathrm{cm}^{-3} \end{aligned} \tag{4.9}$$

Using eq.(4.8) and (4.9) and appropriate distance scaling, the various plasma properties at the light cylinder are as follows.

$$\begin{aligned} \omega_p^2 &\approx 4.1\times10^9\ \chi\left(\frac{\dot{P}_{-15}}{P^7}\right)^{1/2} \\ \omega_{p,res}^2 &\approx 4.1\times10^9\ \eta\left(\frac{\dot{P}_{-15}}{P^7}\right)^{1/2} \\ \omega_B &\approx 3.3\times10^8\left(\frac{\dot{P}_{-15}}{P^5}\right)^{1/2} \\ \delta &\approx 9.6\times10^{-9}\left(\frac{\chi}{\gamma_p^3}\right)\left(\frac{P^3}{\dot{P}_{-15}}\right)^{1/2} \end{aligned} \tag{4.10}$$

The frequency of the emitted waves and the damping frequency follows from eq.(4.10).

$$\begin{aligned} \omega_0 &\approx 3.4 \times 10^{16} \left(\frac{\gamma_p^3}{\chi\gamma_{res}}\right)\left(\frac{\dot{P}_{-15}}{P^4}\right) \\ \omega_1 &\approx 6.5 \times 10^8 \ \gamma_p \left(\frac{\dot{P}_{-15}}{P^5}\right)^{1/2} \end{aligned} \tag{4.11}$$

In order to determine the growth condition we need to look into the relevance of the curvature drift. At the light cylinder $\rho \sim R_{LC}$, hence the drift velocity and drift condition are given as

$$\begin{aligned} u_d &\approx 5.7 \times 10^2 \ \gamma_{res} \left(\frac{P^3}{\dot{P}_{-15}}\right)^{1/2} \\ \frac{u_d^2}{2c^2\delta} &\approx 1.9 \times 10^{-8} \left(\frac{\gamma_{res}^2\gamma_p^3}{\chi}\right)\left(\frac{P^3}{\dot{P}_{-15}}\right)^{1/2} \end{aligned} \tag{4.12}$$

For typical pulsar parameters it can be shown that $u_d^2/c^2\delta \gg 1$, establishing the importance of curvature drift. The growth factor using the second part of eq.(4.7) is

$$\Gamma\tau \approx 1.2 \times 10^{-15} \left(\frac{\eta\gamma_{res}^3}{\gamma_T}\right)\left(\frac{P^3}{\dot{P}_{-15}}\right) \tag{4.13}$$

Finally the limits on frequency, $\omega_0 < \omega_1$, and growth factor, $\Gamma\tau > 1$, constrains the pulsar and plasma parameters.

$$\begin{aligned} \left(\frac{\chi\gamma_{res}}{\gamma_p^2}\right)\left(\frac{P^3}{\dot{P}_{-15}}\right)^{1/2} &> 5.2 \times 10^7 \\ \left(\frac{\eta\gamma_{res}^3}{\gamma_T}\right)\left(\frac{P^3}{\dot{P}_{-15}}\right) &> 8.3 \times 10^{14} \end{aligned} \tag{4.14}$$

The conditions for the emission are shown in Fig. 5.1 for the pulsar population in the $P\dot{P}$ diagram.

4.2.2 Application to off-pulse emission

We now look into the application of the parametric formulation for a specific set of pulsar parameters and apply them to two pulsars with detected off-pulse emission.

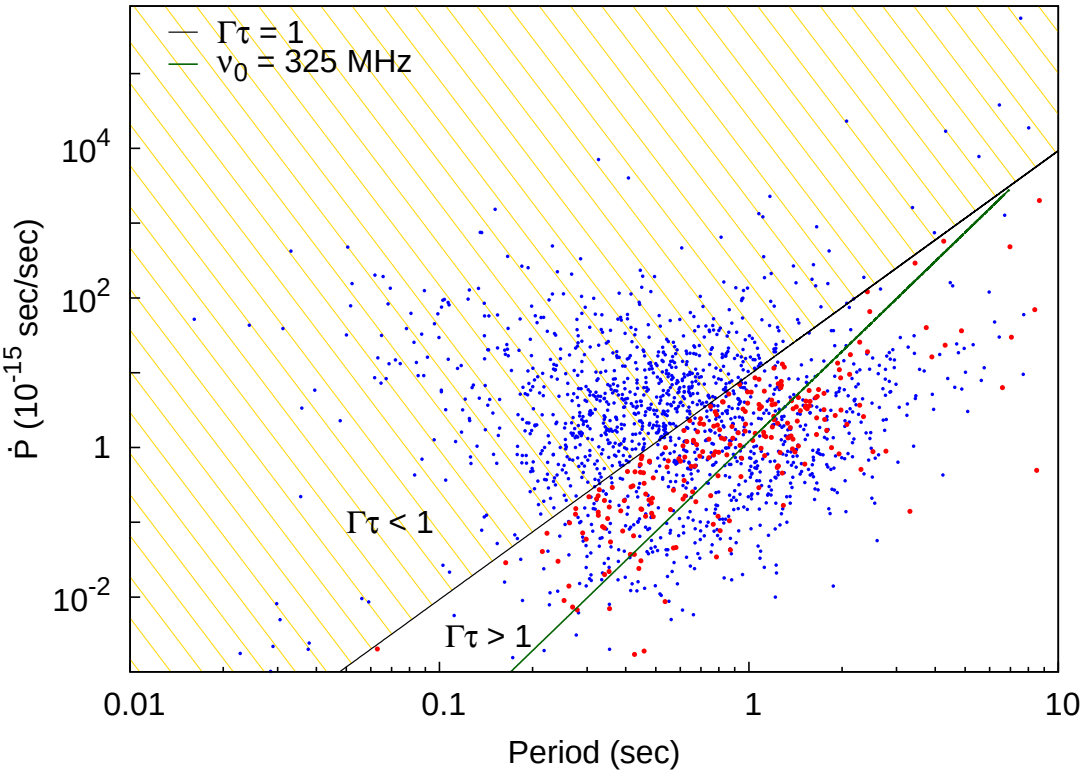

Figure 4.1 The condition for cyclotron resonance instability in the pulsar population (red and blue points) is represented in the $P\dot{P}$ diagram with the relevant pulsar parameters in the text. The solid black line corresponds to growth factor $\Gamma\tau = 1$ [eq.(4.18)]. The instability condition develops in the pulsar population where $\Gamma\tau > 1$ [eq.(4.18)]. The region where $\Gamma\tau < 1$ (shaded region) represents the pulsars (blue points in shaded region) where radio emission in outer magnetosphere cannot originate. The resonance frequency of emission at 325 MHz [eq.(4.16)] is shown as the green line. In addition to satisfying the instability condition (region where $\Gamma\tau > 1$) the possibility of detecting radio emission depends on the flux density and the efficiency of energy in the plasma being converted into radio emission. Using an upper detection limit of 1 mJy for current radio telescopes at the sub GHz range, we estimate the minimum observable luminosity L_{obs} for each pulsar using eq.(4.22). Assuming the efficiency of the emission mechanism to be about 5% of L_p [given by eq.(4.21)] we find a sub-sample (red points) where the emission mechanism presented here can give rise to detectable off-pulse emission (i.e. $0.05L_p > L_{obs}$ and $\Gamma\tau > 1$).

The pulsar parameters used for our studies are, $\gamma_p = 10$; $\chi = 10^4$; $\gamma_{res} = 2{\times}10^6$; $\gamma_T = 10^2$; $\eta = 10^{-1}$. We look at the various conditions as explained above.

$$\frac{u_d^2}{2c^2\delta} \approx 7.6 \times 10^2 \left(\frac{P^3}{\dot{P}_{-15}}\right)^{1/2} \tag{4.15}$$

$$\nu_0 = \omega_0/2\pi \approx 270 \left(\frac{\dot{P}_{-15}}{P^4}\right) \text{ MHz} \tag{4.16}$$

$$\nu_1 = \omega_1/2\pi \approx 1.03 \left(\frac{\dot{P}_{-15}}{P^5}\right)^{1/} \text{ GHz} \tag{4.17}$$

$$\Gamma\tau \approx 9.3 \left(\frac{P^3}{\dot{P}_{-15}}\right) \tag{4.18}$$

B0525+21: $P = 3.7455$ sec; $\dot{P}_{-15} = 40.05$;
The limits expressed in eq.(4.14) reduce to

$$\left(\frac{\chi\gamma_{res}}{\gamma_p^2}\right)\left(\frac{P^3}{\dot{P}_{-15}}\right)^{1/2} = 2.3 \times 10^8 > 5.2 \times 10^7$$
$$\left(\frac{\eta\gamma_{res}^3}{\gamma_T}\right)\left(\frac{P^3}{\dot{P}_{-15}}\right) = 1.05 \times 10^{16} > 8.3 \times 10^{14}$$

B2045–16: $P = 1.9616$ sec; $\dot{P}_{-15} = 10.96$;
The limits expressed in eq.(4.14) reduce to

$$\left(\frac{\chi\gamma_{res}}{\gamma_p^2}\right)\left(\frac{P^3}{\dot{P}_{-15}}\right)^{1/2} = 1.7 \times 10^8 > 5.2 \times 10^7$$
$$\left(\frac{\eta\gamma_{res}^3}{\gamma_T}\right)\left(\frac{P^3}{\dot{P}_{-15}}\right) = 5.5 \times 10^{15} > 8.3 \times 10^{14}$$

B1237+25: $P = 1.3824$ sec; $\dot{P}_{-15} = 0.96$;
The limits expressed in eq.(4.14) reduce to

$$\left(\frac{\chi\gamma_{res}}{\gamma_p^2}\right)\left(\frac{P^3}{\dot{P}_{-15}}\right)^{1/2} = 3.3 \times 10^8 > 5.2 \times 10^7$$
$$\left(\frac{\eta\gamma_{res}^3}{\gamma_T}\right)\left(\frac{P^3}{\dot{P}_{-15}}\right) = 2.2 \times 10^{16} > 8.3 \times 10^{14}$$

B0834+06: $P = 1.2738$ sec; $\dot{P}_{-15} = 6.8$;
The limits expressed in eq.(4.14) reduce to

$$\left(\frac{\chi\gamma_{res}}{\gamma_p^2}\right)\left(\frac{P^3}{\dot{P}_{-15}}\right)^{1/2} = 1.1 \times 10^8 > 5.2 \times 10^7$$
$$\left(\frac{\eta\gamma_{res}^3}{\gamma_T}\right)\left(\frac{P^3}{\dot{P}_{-15}}\right) = 2.4 \times 10^{15} > 8.3 \times 10^{14}$$

B0320+39: $P = 3.0321$ sec; $\dot{P}_{-15} = 0.64$;
The limits expressed in eq.(4.14) reduce to

$$\left(\frac{\chi\gamma_{res}}{\gamma_p^2}\right)\left(\frac{P^3}{\dot{P}_{-15}}\right)^{1/2} = 1.3 \times 10^9 > 5.2 \times 10^7$$
$$\left(\frac{\eta\gamma_{res}^3}{\gamma_T}\right)\left(\frac{P^3}{\dot{P}_{-15}}\right) = 3.5 \times 10^{17} > 8.3 \times 10^{14}$$

The pulsar parameters have been obtained from the publicly available ATNF pulsar database: http://www.atnf.csiro.au/research/pulsar/psrcat/ (Manchester et al. 2005).

In the analysis presented here we have made two basic assumptions that the resonance condition develops at the light cylinder and the secondary plasma is characterized by $\gamma_p = 10$. These assumptions, although they demonstrate the viability of the emission mechanism and constrain the parameter space, do not put strict limits on the secondary plasma energy or location of emission in the pulsar magnetosphere. In one scenario for the same pulsar it is possible for the resonance condition to originate at a different height for a slightly different secondary plasma energy, i.e, lower energy particles will emit the same resonance frequency at a lower height. In an alternate picture the same energy particles will satisfy the resonance condition at a different height for a different resonance frequency, i.e, the resonance frequency will be higher at a lower height. In a typical pulsar all these scenarios are likely to exist, which would account for not only the wide range of frequencies likely to be emitted but also the spread of the detected signal over a wide range in the pulsar profile. However the emission conditions can only develop in the outer magnetosphere near the light cylinder, which in conjunction with the damping frequency puts a limit on the maximum frequency that can be emitted to be around the GHz range.

4.3 Energetics

In this section we look into the total energy available in the plasma and its sufficiency in accounting for the detected off-pulse emission. The total available energy in the plasma when emitted as radio emission gives

$$L_p = \gamma_{res} m c^3 n_{res} \beta_p \quad \text{erg } s^{-1} \tag{4.19}$$

Here β_p represents the cross-section of the open field lines, $\beta_p = 6.6 \times 10^8 P^{-1} (R/R_s)^3$ cm^2. The luminosity of the off-pulse emission is given as:

$$L_{obs} = 4\pi D_L^2 S_\nu \Delta\nu \; \zeta^{-1} \quad \text{erg } s^{-1} \tag{4.20}$$

Here D_L is the distance to pulsar; S_ν the observed off-pulse flux; $\Delta\nu$ is the frequency range and ζ the fractional opening angle. Using γ_{res}=2×10^6; η=10^{-1}; S_ν=1 mJy; $\Delta\nu$=100 MHz; ζ=10^{-1} eq.(4.19) and (4.20) are expressed as

$$L_p \approx 2.2 \times 10^{29} \left(\frac{\dot{P}_{-15}}{P^3} \right)^{1/2} \tag{4.21}$$

$$L_{obs} \approx 1.2 \times 10^{27} D_{kpc}^2 \tag{4.22}$$

Applying the luminosity values to the two pulsars as in the previous section we look into the relevance of the mechanism.

B0525+21: $D_{kpc} = 2.28$. $L_p = 2.5{\times}10^{29}$; $L_{obs} = 6.2{\times}10^{27}$.

B2045–16: $D_{kpc} = 0.95$. $L_p = 1.8{\times}10^{29}$; $L_{obs} = 1.1{\times}10^{27}$.

B1237+25: $D_{kpc} = 0.84$. $L_p = 1.3{\times}10^{29}$; $L_{obs} = 8.5{\times}10^{26}$.

B0834+06: $D_{kpc} = 0.72$. $L_p = 4.0{\times}10^{29}$; $L_{obs} = 6.2{\times}10^{26}$.

B0320+39: $D_{kpc} = 1.49$. $L_p = 3.3{\times}10^{28}$; $L_{obs} = 2.7{\times}10^{27}$.

$L_p \gg L_{obs}$ for off-pulse emission in all the pulsars in our sample. It is clear that the cyclotron resonance instability is an energetically viable mechanism for off-pulse emission.

4.4 Discussion

In this chapter we have demonstrated the generation of radio emission due to the cyclotron resonance instability within the outer magnetosphere of pulsars making it a relevant candidate for off-pulse emission. The conditions for radio emission are dependent on the parameters of the plasma which are still poorly understood. The details of the calculations shown here will vary with changes in plasma parameters although the basic physical processes would still operate in pulsars. We can draw two primary conclusions about the nature and extent of the emission from these studies. Firstly, these conditions can only develop in a certain population of pulsars which have longer periods and/or smaller period derivatives. Secondly, there is an upper limit to the frequency that can be emitted constrained by the damping frequency. In addition we have also found an observational limit based on the detection capabilities of present day telescopes and energetics which show the emission from long period pulsars with very small period derivatives being too weak to be detected. The pulsars which follow the above criteria are shown as red points in Fig. 5.1 (see figure caption for details).

We have demonstrated the applicability of the conditions of cyclotron resonance instability by considering the physical parameters of the five pulsars where we have detected off-pulse emission. However, this should not be considered a comprehensive demonstration as we have only presented a rough outline of the mechanism. We are still to characterize the off-pulse emission including their location in the pulsar magnetosphere, the polarization characteristics of the emission, the kinematic effects like abberation and retardation, etc. These informations would be vital for obtaining a detailed model of the off-pulse emission which in its present form is inadequate for application on a case by case basis.

Chapter 5

Pre-Cursor Emission: A Morphological Viewpoint

5.1 Morphology of Main Pulse Emission

The radio emission from pulsars is seen as a series of periodic pulses with varying shape and intensity. The integrated profile obtained by averaging a number of such individual pulses (usually a few thousand) is a stable feature which show little variation over time. The pulsed emission is associated with a high degree of linear polarization with the polarization position angle showing a rotation across the profile resembling a S-shaped curve. The radio emission originates along the open field lines above the polar cap, centered around the magnetic axis, and is highly beamed. The plane containing the magnetic field lines and the rotation axis determines the polarization of the emitted radiation which traces the typical polarization position angle (PPA) as the line of sight traverses the emission region (Radhakrishnan & Cooke 1969). The pulsar profile is seen to consist of one or more individual components, known as subpulses, which show a large variety in shape and extent and also exhibit frequency evolution. The shape and polarization properties of pulsar profiles are useful for studying the emission mechanism of radio emission, the structure of the emission region, geometrical orientation of pulsars, etc (Lyne & Manchester 1988; Rankin 1983, 1990).

The radio emission is assumed to originate within an emission beam which exhibit frequency evolution, i.e. the lower frequency emission originates at higher altitudes in the pulsar magnetosphere signifying a wider opening angle or emission beam. The emission beam is populated by two distinct pulsed components the core and cone emission showing contrasting features. The core emission is located near the centre of the emission beam while conal emission is located towards the outer regions of the beam. The core emission show stable phases and no significant evolution of width with frequency while the cone emission component on the other hand exhibit phase modulation in the form of drifting subpulses and also exhibit significant evolution of width with frequency. Further, the the core emission component show a steep PPA sweep and show significant circular polarization, the conal component on the other hand show shallow PPA traverse and exhibit weak levels of sign changing circular polarization. Attempts have been made to understand the illumination of the emission beam with two principal models being the patchy beam proposed by Lyne & Manchester (1988) and the core-cone morphology postulated by Rankin (1983). The patchy beam model assumes the intensities from different parts of the beam to vary with only a portion of the beam visible. The radiation is also expected to exhibit a steady decrease in the spectral index as one moves from the peripheral regions to the center of the beam. The core-cone morphology on the other hand assumes the emission beam comprising of a central core component surrounded by two or more concentric rings filled with conal emission, the core components being associated with central field lines while the conal components with the outer field lines. A large number of studies over the years (see Rankin 1993a; Mitra & Deshpande 1999; Mitra & Rankin 2002, 2011) dealing with uncovering the nature of the emission beam have tended to favour the core-cone morphology. Mitra & Deshpande (1999) have analysed pulsars with conal components and found the cones to be in the form of nested rings with widths $\sim 20\%$ the beam radius. Mitra & Rankin (2011) have looked at pulsars with partial cones where supposedly one half of the conal components were missing and in most cases have found weak counterparts to the partial cones thereby strongly favouring the core-cone morphology. We believe the core-cone morphology to be at present the best description of the pulsar beam and will use their implications in our

analysis.

There are certain emission components known as pre/post-cursors (PPC) seen in a small sample of pulsars where the general model fails to explain their shape and origin. These emission components are seen either preceding or following the main pulse emission at considerable separation and are usually characterized by high degree of linear polarization and flat position angles. The presence of such emissions have been reported in pulsars B1822–09 and B0943+10 (Backus et al. 2010) and B1322+83 and B2224+65 (Mitra & Rankin 2011) where detailed analysis have revealed the main pulse to be consistent with the standard model. However, no studies have been conducted, to the best of our knowledge, aimed at characterizing the underlying shape and geometry of the PPC components. In our present studies we attempt to understand the underlying origin of the PPC components within the framework of the standard approach of pulsar emission beams as developed by Rankin (1993a); Mitra & Deshpande (1999); Mitra & Rankin (2002). We use archival data in the literature to study the frequency evolution of the PPC components present in the pulsars B1822–09 and B2224+65 over a wide frequency range and also for pulsars B0943+10 and B1322+83 over a smaller frequency regime.

5.2 Pulsar Emission: Structure & Location

The pulsar radio emission originates in the open dipolar field lines above the polar regions and hence the underlying geometry is determined by solving for a rotating magnetic dipole with emission beam directed towards observer. The geometry of the emission is characterized by the angle between the rotation and magnetic axis α and the angle between magnetic axis and observer's line of sight β. The rotating vector model (Radhakrishnan & Cooke 1969) gives an estimate of the polarization position angle (PPA), χ as a function of longitude φ:

$$\tan\chi = \frac{\sin\alpha \, \sin\varphi}{\cos\alpha \, \sin(\alpha+\beta) - \sin\alpha \, \cos(\alpha+\beta) \, \cos\varphi} \tag{5.1}$$

The rate of change of the PPA with respect to the longitude at the steepest gradient point is given as:

$$\left(\frac{d\chi}{d\varphi}\right)_{\rm max} = \frac{\sin\alpha}{\sin\beta} \tag{5.2}$$

It is possible to solve for the angles α and β from the above equations however they yield highly correlated values (Lyne & Manchester 1988). However an independent estimate of the angle α was formulated by Rankin (1990) who relates it to half power width of the core emission component.

$$\sin\alpha = 2.45^{\circ} P^{-0.5}/W_{core} \tag{5.3}$$

Once secure estimates of the angles α and β for a pulsar is available it is possible to estimate the beam opening angle ρ from the measured width of the pulsar profile ψ using spherical geometry (Gil et al. 1984).

$$\sin^2(\rho/2) = \sin^2(\beta/2) + \sin\alpha\,\sin(\alpha+\beta)\,\sin^2(\psi/4) \tag{5.4}$$

Considerable effort have been made to determine the beam opening angles of the conal emission especially in pulsars with associated core emission components. Rankin (1993a,b) estimated the conal emission to consist of a pair of inner and outer cones. The 1 GHz width of the inner and outer cones was given as:

$$\rho^{\rm inner}_{\rm GHz} = 4.33^{\circ}\ {\rm P}^{-0.5} \qquad \rho^{\rm outer}_{\rm GHz} = 5.75^{\circ}\ {\rm P}^{-0.5} \tag{5.5}$$

The $\rm P^{-0.5}$ dependence is once again an outcome of the dipolar fields where the radio emission originates. Mitra & Deshpande (1999) analyzed around forty pulsars at six different frequencies, with each frequency signifying a separate beam opening angle, and postulated the presence of three conal components in the pulsar beam. They estimated the frequency evolution of conal beams given as:

$$\rho^{\rm r}_{\rm MHz} = 4.8^{\circ} r(1 + 66\nu^{-1}_{\rm MHz})\ {\rm P}^{-0.5} \tag{5.6}$$

Here r = 0.8, 1.0, 1.3 respectively for the three conal components.

The radio emission height in the pulsar magnetosphere is proportional to the square of the opening angle of the emission beam in the dipolar field context. This provides

a direct estimate of the emission height taking into account the angular size of the polar cap and the radius of neutron star provided we have an estimate of the size of the outermost open field lines. The outermost field lines are assumed to be associated with the outer cone emission and the emission height is given as (Kijak & Gil 1998):

$$h = 10\mathrm{P}\left(\frac{\rho^{\mathrm{outer}}}{1.23^{\circ}}\right)^{2} \quad \mathrm{km} \tag{5.7}$$

Independent estimates of the emission heights have been obtained using the aberration-retardation effects, shifts in the pulsar profile as a result of relativistic beaming, and they are consistent with the heights estimated using the geometrical method (Krzeszowski et al. 2009).

5.3 Observational Results

We have mainly used archival data in order to study four pulsars with supposed PPC components B0943+10, B1322+83, B1822–09 and B2224+65. We have concentrated on the total power profiles of these pulsars and in addition to the archival data have used some unpublished GMRT data for our purpose. Two of the pulsars B1822–09 and B2224+65 showed the presence of the PPC components over a wide frequency range. In this section we collect the basic observational traits of the PPC components on a case by case basis.

5.3.1 Pre-cursor emission in B1822–09

The pulsar profile comprises of a pre-cursor emission and an interpulse in addition to the main pulse. A large number of studies have been devoted to understand the properties of this pulsar which revealed signatures of mode changing with the 'Q'-mode associated with the interpulse and the 'B'-mode showing the presence of the pre-cursor. The pulsar also show significant mode mixing where both the emission components are present (Latham et al. 2012). Gil et al. (1994) carried out multi frequency profile studies of this pulsar but failed to recognize the uniqueness of pre-cursor component. Backus et al. (2010) identified the leading component in

the pulsar as the pre-cursor emission and also identified the morphology of the main pulse comprising of inner cone along with the core component. We have carried out a detailed investigation of the profiles of this pulsar and determined the half power widths as well as the separation between the various components in the frequency range 0.24–10.5 GHz. The pre-cursor component becomes relatively weaker as frequency of observation decreases and becomes increasingly difficult to discern at low frequencies. Table 5.1 shows the component spacing, width and beam opening angles: column 4 shows the measured width of the main pulse at the half power point by fitting one and in some cases two gaussians; column 5 shows the measured half power width of the pre cursor component by fitting a gaussian; column 6 represents the separation between the peaks of the main pulse and precursor. The interpulse emission have been shown to be a much wider component by Backus et al. (2010) with 180° separation between its central point and the main pulse. But in most cases the interpulse is too weak to detect the entire emission and hence we resort to calculating the separation between the peaks of the main pulse and interpulse as shown in column 7. The geometry has been estimated by Mitra & Rankin (2011) with $\alpha = 86°$ and $\beta = 0°$. Using eq.(5.4) we determine the beam radius of the main pulse in column 8 and the pre-cursor component using the separation between the pre-cursor and the main pulse as half opening angle in column 9 with the errors calculated using estimates of Mitra & Rankin (2002) [eq.(4)therein]. In figure 5.1 we have plotted the beam radius of the pre-cursor and main pulse components for this pulsar.

5.3.2 Post-cursor emission in B2224+65

The pulsar consists of two gaussian like emission components with the trailing component exhibiting a high degree of linear polarization and flat position angle swing. Lyne & Manchester (1988) classified the pulsar as a partial cone with one half of the cone emission missing. However Mitra & Rankin (2011) identified the trailing component as a post-cursor emission component, despite the PPA fitting both the components very well, due to the large separation of the post-cursor component from the leading component and the missing half of the supposed conal component. We

Table 5.1 The component spacing, width and beam radius

Pulsar	Period sec	ν MHz	MP wid $^\circ$	PC wid $^\circ$	PC-MP $^\circ$	IP-MP $^\circ$	$\rho^{\rm MP}$ $^\circ$	$\rho^{\rm PC}$ $^\circ$
		243	8.1±0.4	3.9±0.6	14.4±0.3	-	4.0±0.2	14.4±0.3
		325	7.1±0.2	7.0±0.2	15.2±0.1	186.3±0.1	3.5±0.1	15.2±0.1
		408	6.7±0.4	4.1±0.2	14.8±0.1	185.7±0.2	3.3±0.2	14.8±0.1
		610	7.1±1.1	6.7±0.2	14.6±0.6	186.2±0.6	3.5±0.5	14.6±0.6
		800	6.8±0.1	7.4±0.3	14.5±0.1	185.7±0.2	3.4±0.1	14.5±0.1
		925	5.4±0.1	7.7±0.2	15.0±0.1	186.3±0.1	2.7±0.1	15.0±0.1
		1330	6.5±0.1	7.1±0.1	14.7±0.1	186.0±0.2	3.2±0.1	14.7±0.1
B1822–09	0.769	1408	5.2±0.1	6.0±0.1	14.7±0.1	186.0±0.1	2.6±0.1	14.7±0.1
		1408	5.5±0.2	5.4±0.1	14.6±0.1	187.2±0.1	2.7±0.1	14.6±0.1
		1410	6.1±0.3	5.6±0.2	13.6±0.1	187.0±0.1	3.0±0.2	13.6±0.1
		1640	5.7±0.3	6.4±1.0	14.9±0.4	-	2.8±0.2	14.9±0.4
		1642	6.0±1.1	5.6±0.1	14.3±0.8	186.7±1.1	3.0±0.5	14.3±0.8
		4750	5.9±0.7	5.1±0.1	14.1±0.4	186.8±0.4	2.9±0.3	14.1±0.4
		4850	4.9±0.1	5.6±0.1	13.9±0.04	-	2.4±0.1	13.9±0.04
		10450	3.0±0.2	5.5±0.5	14.3±0.2	-	1.5±0.1	14.3±0.2
		10550	3.6±0.1	6.3±0.3	14.3±0.1	-	1.8±0.1	14.3±0.1
		325	12.1±0.2	18.7±0.7	33.3±0.3	-	3.7±0.2	10.0±0.1
		400	12.0±0.2	15.1±0.7	32.1±0.3	-	3.7±0.2	9.7±0.1
		408	10.4±0.3	13.4±1.3	32.7±0.6	-	3.6±0.2	9.9±0.2
		610	11.3±0.2	10.9±0.3	31.2±0.1	-	3.7±0.2	9.5±0.1
B2224+65	0.683	800	12.0±0.5	10.1±0.4	30.5±0.3	-	3.7±0.2	9.3±0.1
		925	11.3±0.5	7.5±0.3	29.9±0.2	-	3.7±0.2	9.2±0.1
		1330	12.3±0.3	8.3±0.4	29.5±0.2	-	3.7±0.2	9.0±0.1
		1408	10.7±0.1	6.7±0.1	29.5±0.2	-	3.6±0.2	9.0±0.1
		1408	11.7±0.2	7.0±0.1	29.3±0.1	-	3.7±0.2	9.0±0.1
		1642	11.5±0.3	6.7±0.1	28.9±0.1	-	3.7±0.2	8.9±0.1
B0943+10	1.098	325	12.8±0.1	23.4±1.0	52.8±0.5	-	5.6±0.05	13.4±0.1
		610	13.2±0.2	14.4±1.2	51.7±0.6	-	5.6±0.05	13.2±0.1
B1322+83	0.670	325	9.8±0.2	17.1±1.0	42.9±0.6	-	5.3±0.1	12.9±0.1
		610	10.0±0.4	-	42.2±0.8	-	5.3±0.1	12.7±0.2

have carried out a detailed study of the frequency evolution of the pulsar profile with particular emphasis on the emission components of this pulsar in the frequency range 0.325 – 1.6 GHz. In Table 5.1 we calculate the component widths and separation of the main pulse and post-cursor components. The main pulse emission has been identified with the core emission component. The geometry has been estimated by Mitra & Rankin (2011) nd is specified by $\alpha = 27^\circ$ and $\beta = 4.9^\circ$. However, the core width was incompatible with the above geometry and using the average width 11.3° (4^{th} column in table 5.1), eq.(5.2) and (5.3) the geometry was estimated to be $\alpha = 15.2^\circ$. We used $(d\chi/d\varphi)_{\rm max}$ = -4.5 from Lyne & Manchester (1988) to determine $\beta = 3.3^\circ$. The beam radius has been calculated for the main pulse in the 8^{th} column. The 9^{th} column represents the beam radius with the separation between the main pulse and the trailing component peaks taken as half opening angle. The beam radii for the main pulse and the trailing component (plotted in blue points) are also shown in figure 5.1.

5.3.3 Pre-Cursor emission in B0943+10

The pulsar is known to exhibit mode changing with 'Q' and 'B' modes with the main pulse being a classic example of conal emission component. The pulsar show subpulse drifting phenomenon particularly in the 'B' mode. Backus et al. (2010) reported the presence of a faint emission component preceding the main pulse emission and far away from it which they identified as a pre-cursor emission. The pre-cursor component, characterized by high degree of linear polarization, was present only during the 'Q'-mode. The pulsar is particularly weak especially during the 'Q'-mode and lacks high quality data at high frequencies to carry out our analysis. We had access to 'Q'-mode pulsar profiles at 325 MHz and 610 MHz which were used for our studies. The geometry of this pulsar have been reported in Rankin (1993b) to be $\alpha = 11.5^\circ$and $\beta = 5.4^\circ$. We have determined the width of the main pulse, the pre-cursor component and the separation between peaks of the pre-cursor and main pulse in columns 4, 5 and 6 of table 5.1. The beam radius of the main pulse is calculated in column 8, using the pulsar geometry and eq.(5.4). In column 9 we represent the

beam radius with the separation between the main pulse and pre-cursor taken as half opening angles which are also depicted in figure 5.1.

5.3.4 Pre-Cursor emission in B1322+83

The pulsar was studied in great detail by Mitra & Rankin (2011) at 325 MHz who reported the presence of a weak leading component ahead of the main pulse emission. This emission component once again exhibited high linear polarization with a flat position angle swing and was identified as a pre-cursor component. The main pulse emission exhibit the properties of a conal single profile and the profile is similar to the 'Q'-mode of B0943+10. The main pulse emission also exhibit signatures of scattering with a scattering tail at the trailing end which made estimates of pulse widths difficult. The geometry of the pulsar have been determined by Mitra & Rankin (2011) as $\alpha = 14^{\circ}$ and $\beta = 5.1^{\circ}$. The pre-cursor component for this pulsar is particularly weak and hence have not been detected in most of the pulsar profiles at other frequencies apart from the profile at 610 MHz. However we have not been able to discern the width and extent of the pre-cursor component at 610 MHz due to the signal being very weak but we have managed to identify its peak value. The component widths and separation at 325 MHz and 610 MHz is shown in table 5.1 along with the radius of the beam determined from the geometry of the pulsar. The estimates of the radii of the main pulse and pre-cursor beam have been shown in figure 5.1.

5.4 Discussion

5.4.1 Outer Conal emission in B2224+65 and PPC emission

We have shown in figure 5.1 a clear demarcation between the PPC emission components and the main pulse emission. The boundary (Mitra & Deshpande 1999) of the outer conal emission in the figure shows the maximum extent of the main pulse beam opening angle. The pre-cursor components in B1822–09, B0943+10 and B1322+83 all lie well outside the conal boundary. The trailing component of B2224+65 however

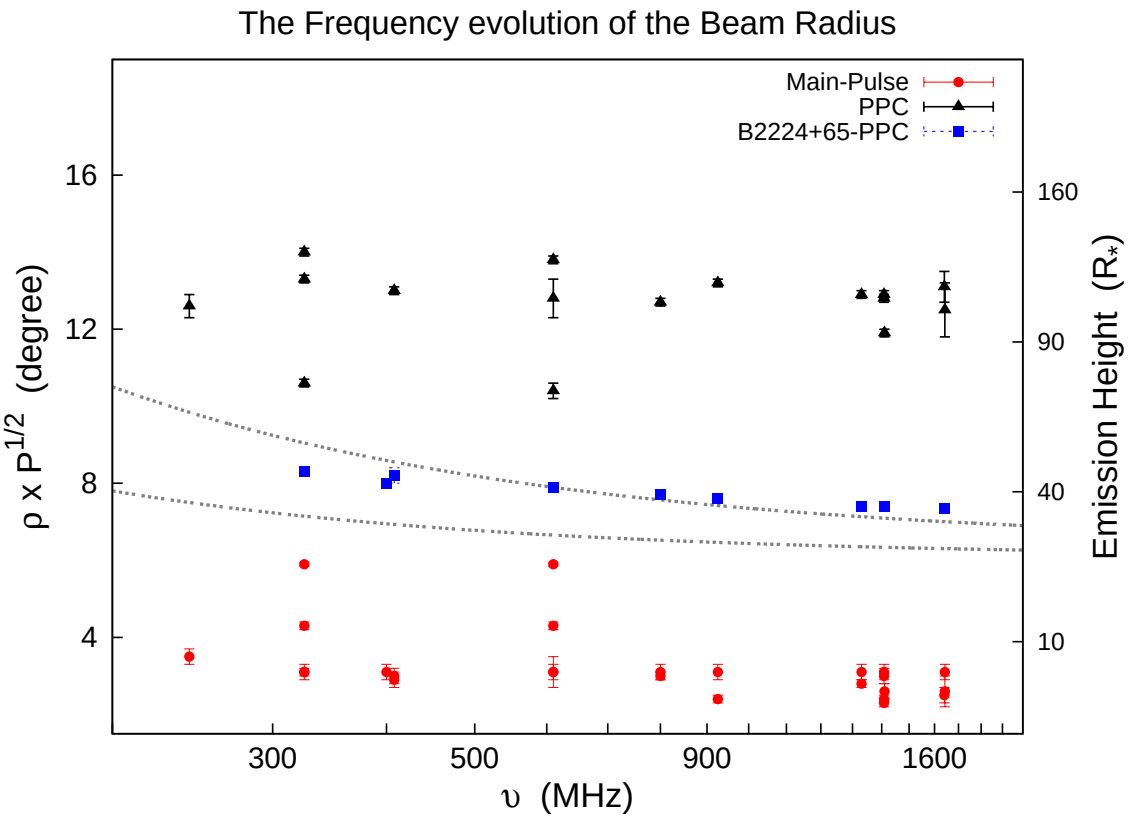

Figure 5.1 The figure shows the evolution of the radius of beam opening angle with frequency for the main pulse and the PPC components in the four pulsars B1822–09, B2224+65 (PPC shown separately in blue), B0943+10 and B1322+83. The dotted lines corresponds to the spread in the beam radius of the outermost conal components as determined by Mitra & Deshpande (1999) representing the maximum extent of the dipolar open field lines. The main pulse emission in all the four pulsars lie well within the pulsar beam corresponding to either the core or conal emission components. The post-cursor component in B2224+65 exhibit significant frequency evolution and can be identified with an extremely outer region of the beam and is therefore not a PPC component. The PPC components of the remaining three pulsars is not consistent with the core-cone morphology, show no frequency evolution and lies well outside the beam specified by the dipolar open field lines. In the right hand side we have shown the emission heights for the beam radius corresponding to the last open field lines which clearly demonstrate the pre-cursor components originating much higher up the pulsar magnetosphere compared to the main pulse emission.

lies within the boundary demonstrating that this emission component was erroneously identified as a post-cursor.

The frequency evolution of the trailing component in B2224+65 and the pre-cursor component of B1822–09 is quite informative about their different nature. The trailing component in B2224+65 clearly show a certain evolution with frequency which is consistent with the outer conal components and dipolar geometry. We conclude that the pulsar B2224+65 is a typical example of the partial cones of Lyne & Manchester (1988) with an observed one sided outer cone at the extreme boundaries of the emission beam leading to the confusion about its post-cursor nature. The pre-cursor emission component in B1822–09 however show no variation with frequency over the wide frequency range extending from 200 MHz to 10 GHz. The pre-cursor emission from pulsars and raises interesting questions about their underlying emission mechanism which we briefly explore in the next section. However, the studies carried out here have established the unique morphological and geometrical origin of the PPC emission from pulsars in addition to providing a suitable method of distinguishing the PPC components from the outer conal emission lying far away from the main pulse.

5.4.2 Emission Heights and origin of PPC emission

In figure 5.1 we have determined the emission heights on the right hand side using eq.(5.7) and assuming the beam radius to represent the last open field lines. The main pulse emission arises at heights of 20–50 R_*, where R_* is the radius of the neutron star, which is largely consistent with our estimates. The core and inner cone components in the figure appear to arise from lower heights as they originate from inner field lines and hence are underestimated. The pre-cursor emission on the other hand appears to originate much higher up the open field lines with lower limits between 100–150 R_*. In addition the PPC component in B1822–09 show no signatures of evolution over a wide frequency range. This indicates two possibilities about their origin, either the PPC components emanate from a region where the signatures of frequency evolution are not detectable like the inner field lines or the emission mechanism responsible for the PPC components give rise to different frequencies at similar altitudes.

The main pulse radio emission is expected to originate in the outflowing plasma generated in the inner vacuum gap above the magnetic poles. The plasma consists of relativistic charged particles with singly charged primary particles $\gamma_b \sim 10^6$ and secondary pair plasma with $\gamma_p \sim 10 - 1000$. The radio emission at heights of 10–50 R_* is believed to originate as a result of coherent curvature radiation from charged bunches developing in the secondary pair plasma with characteristic frequency $\omega_c \sim \gamma_p^3 c/R_C$, here R_C being the radius of curvature of the field lines (Ruderman & Sutherland 1975). The plasma generated in the inner vacuum gap is nonstationary with overlapping clouds which lead to two stream instability giving rise to electrostatic langmuir waves which are modulationally unstable. The linear growth rate for the langmuir waves in this context have been estimated by Asseo & Melikidze (1998) with the condition for instability development given as $(\gamma_p/100)^{-1.5}(r/50R_*)^{-1.5}(\dot{P}_{-15}/P)^{1/4} \gg 0.1$, where r is the emission height and $\dot{P}_{-15}$ is the period derivative in units of 10^{-15} sec/sec. The nonlinear processes in the plasma generates bunching in the form of solitons from these electrostatic langmuir waves. The energy distribution of the oppositely charged e^-e^+ particles in the secondary plasma is anisotropic in order to maintain the force free condition of screening the corotation electric field. The anisotropy in the particle distribution leads to charge separation in the solitons which emit curvature radiation (Melikidze et al. 2000; Gil et al. 2004). The soliton, whose size is larger than the wavelength of langmuir waves, is unable to radiate at wavelengths shorter than its longitudinal size and hence the emission frequency in the pulsar frame must be less than the frequency of plasma waves, i.e $\omega < 2\sqrt{\gamma_p}\omega_p$ where $\omega_p = (4\pi e^2 n/m_e)^2$ is the plasma frequency.

In the case of the pre-cursor emission with emission frequencies ranging from 200 MHz to 10 GHz and originating at heights of $r = 150$ R_* we look into the above mechanism for generating radio waves. The growth of the langmuir waves at these emission heights only becomes efficient for the lower energy region of the secondary plasma with $\gamma_p \leq 30$. The radius of curvature of dipolar field lines at the emission height may be approximated as $R_C \sim 10\ r$. Hence the frequency of radiation is given as $\omega \sim 20\ \gamma_p^3$ while the plasma frequency is estimated to be $\omega_p = 8.1 \times 10^8$ rad s^{-1}. It is clear that the plasma frequency is very low ($\nu_p \sim 130$ MHz) and

the radiation is possible for values of γ_p which is on the higher side of the available energy distribution of secondary plasma where the growth of the langmuir waves is not efficient. In addition the inequality condition ($\omega < 2\sqrt{\gamma_p}\omega_p$) puts an upper limit on the maximum $\gamma_p \leq 1100$ making high frequency emission in the GHz range unlikely. The inner vacuum gap with the nonstationary outflowing plasma along dipolar field lines and the soliton model for coherent radio emission is unlikely to account for the pre-cursor emission at heights of $150R_*$.

Another possible location of the pre-cursor emission is the outer magnetosphere where the cyclotron resonance mechanism for coherent radio emission can be a possible source of emission (Kazbegi et al. 1991; Lyutikov et al. 1999). In chapter 4 we have used this mechanism to explain the origin of off-pulse emission from long period pulsars. However, the mechanism suffers from similar concerns of upper frequency limits and fine tuning of plasma parameters as the mechanism for curvature radiation (see chapter 4 for details). This scenario would require explanation of the pulsed nature of the pre-cursor emission in addition to accounting for modifications in the pulse shape due to kinematic effects like aberration-retardation at these emission heights.

The pre-cursor emission in pulsars is distinct from the main pulse emission, with the location of the pre-cursor components much higher up in the magnetosphere compared to the main pulse. It seems likely that the coherent curvature radiation mechanism for the main pulse is inadequate for explaining their origin. Detailed studies are required to characterize the nature of the emission including identifying the location of the pre-cursor within the magnetosphere and also look into possible acceleration regions and/or emission mechanisms for explaining the pre-cursor emission in pulsars.

Chapter 6

Conclusion

A large number of models explaining the origin of the main pulse emission in normal long period pulsars predict the presence of an inner vacuum gap above the polar caps giving rise to a nonstationary, multi component, relativistic plasma with primary and secondary particles. The main pulse emission originates in the inner magnetosphere due to instabilities in the secondary plasma exciting coherent curvature radiation. In this physical model a natural outcome is the cyclotron resonance instability where resonant interaction of primary particles with the plasma waves in the secondary plasma may take place with the possibility of coherent radio emission in the outer magnetosphere far away from the main pulse. This thesis has been devoted to devising detection techniques and characterizing radio emission far away from the conventional main pulse emission in pulsars. In this final chapter we present the primary conclusions of our studies and also briefly discuss the possible limitations of our work and scope for future extensions.

a. We have demonstrated the technique of 'Offline-Gating' using high time resolution interferometric modes of GMRT. We have also devised several tests which have not revealed any irregularities in the telescope receiver system which can cause spurious detections. The gating technique was limited by the time resolution of the interferometer as a certain number of time bins are required to be accommodated in the pulsar period for secure gating and high signal to noise detections. The GMRT has

minimum time resolution around 128 milliseconds which makes these studies possible for older pulsars with periods $\geq$ 1.2 seconds. The pulsars used in our studies were relatively strong and hence our folding techniques were adequate for determining the on and off-pulse regions.

b. We have used the gating techniques to detect off-pulse emission in five pulsars B0525+21, B2045–16, B1237+25, B0834+06 and B0320+39. These were the first secure detections of weak baseline level emission from normal long period pulsars, to the best of our knowledge. The observations were carried out at two different frequencies 325 MHz and 610 MHz and in case of certain pulsars were repeated at multiple epochs. We established the off-pulse emission to be magnetospheric in origin by determining upper limits on their location from scintillation studies. This further enabled us to determine the brightness temperatures of the off-pulse emission which turned out to be very high, $T_B \geq 10^{18}$ K, which suggest the off-pulse emission to be coherent in nature. The spectra of the off-pulse emission turned out to be steep and comparable to the main pulse emission for the longer period pulsars (B0525+21, B2045-16 and B0320+39) however the spectra showed signs of flattening (B0834+06) and also turning over (B1237+25) for the shorter period pulsars. We failed to detect off-pulse emission at either 325 MHz or 610 MHz frequency bands for the pulsar J2144–3933, which was the longest period pulsar in our sample. Our studies at present can be best summarized as preliminary detections where we have achieved a glancing understanding of the nature of off-pulse emission. Future studies need to focus on extending the sample size of pulsars studied; carrying out a phase resolved study of the off-pulse emission by implementing bin by bin imaging to uncover temporal structures in off-pulse; uncovering polarization characteristics, spectral behaviour of off-pulse emission over a wider frequency range, etc, before inducing serious conclusions about the detailed nature of off-pulse emission and their implications on the physical characteristics of pulsars.

c. The radio emission originates in the outflowing plasma along the open dipolar field lines. The main pulse emission occupies a small part of the pulsar profile and

originates in the inner magnetosphere. The off-pulse emission on the other hand is presumably spread over a large part of the profile and located far away from the main pulse indicating their origin in the outer magnetosphere with wider opening angle of the dipolar field lines. The cyclotron resonance instability developing in the outer magnetosphere near the light cylinder is the only known source of coherent radio emission at these heights. The instability develops when the primary particles gyrating around the magnetic field lines resonate with the naturally occurring electromagnetic modes in the lower energy regime of the secondary pair plasma, resulting in the amplification of these plasma waves which detach at the plasma boundary and is emitted. We have investigated the growth rate and damping frequency limit of the instability condition in the wider pulsar population and based on the detection limit of present day telescopes have identified a subsample of $\sim$ 200 pulsars with detectable radio emission including the five pulsars in our sample. However, our studies yielded preliminary estimates with a broad overview of the emission. We need to exhaust the observational features of the off-pulse emission followed by detailed modelling, which include the modification of emission properties due to kinematical effects at the emission altitudes, before we can extend our studies to individual pulsars and test the efficacy of this mechanism.

d. The pre/post-cursor emission seen in a handful of pulsars is a pulsed emission component lying far away from the main pulse. We have investigated four pulsars B1822–09, B2224+65, B0943+10 and B1322+83 with signatures of pre/post-cursor emission components within the purview of the established geometrical picture. Our studies reveal that the post-cursor component in B2224+65 resembles an outer conal emission. The pre-cursor component in B1822–09, B1322+83 and B0943+10 seem to be distinct from the main pulse with their emission heights much higher up in the pulsar magnetosphere compared to the main pulse. In addition the pre-cursor do not show signatures of frequency evolution resembling the core or inner cone and quite unlike the outer conal emission. It seems likely that the coherent curvature radiation mechanism for the main pulse is inadequate for explaining their origin. Detailed studies are required to characterize the nature of the emission including identifying

the location of the pre-cursor within the magnetosphere and also look into possible acceleration regions and/or emission mechanisms for explaining the pre-cursor emission in pulsars.

In this thesis we have studied radio emission which originate far away from the main pulse emission in the pulsar profiles as off-pulse and pre-cursor emission. In the standard geometrical picture of pulsars we have demonstrated these emission components to originate higher up the pulsar magnetosphere. We have explored cyclotron resonance mechanism originating in the outer magnetosphere which is consistent with the off-pulse emission and may also be the source of pre-cursors. The radio emission seem to encompass two distinct regimes in pulsars, the conventional main pulse emission originating in the inner magnetosphere and the distinct class of off-pulse emission and pre-cursors which originate much higher up in the outer magnetosphere.

Appendix A

Images for off-pulse emission

In this appendix we present all the remaining images of the on and off-pulse emission for the five pulsars observed during our studies as mentioned in table 3.2. We also present the short time interval images used in 3.3.2.

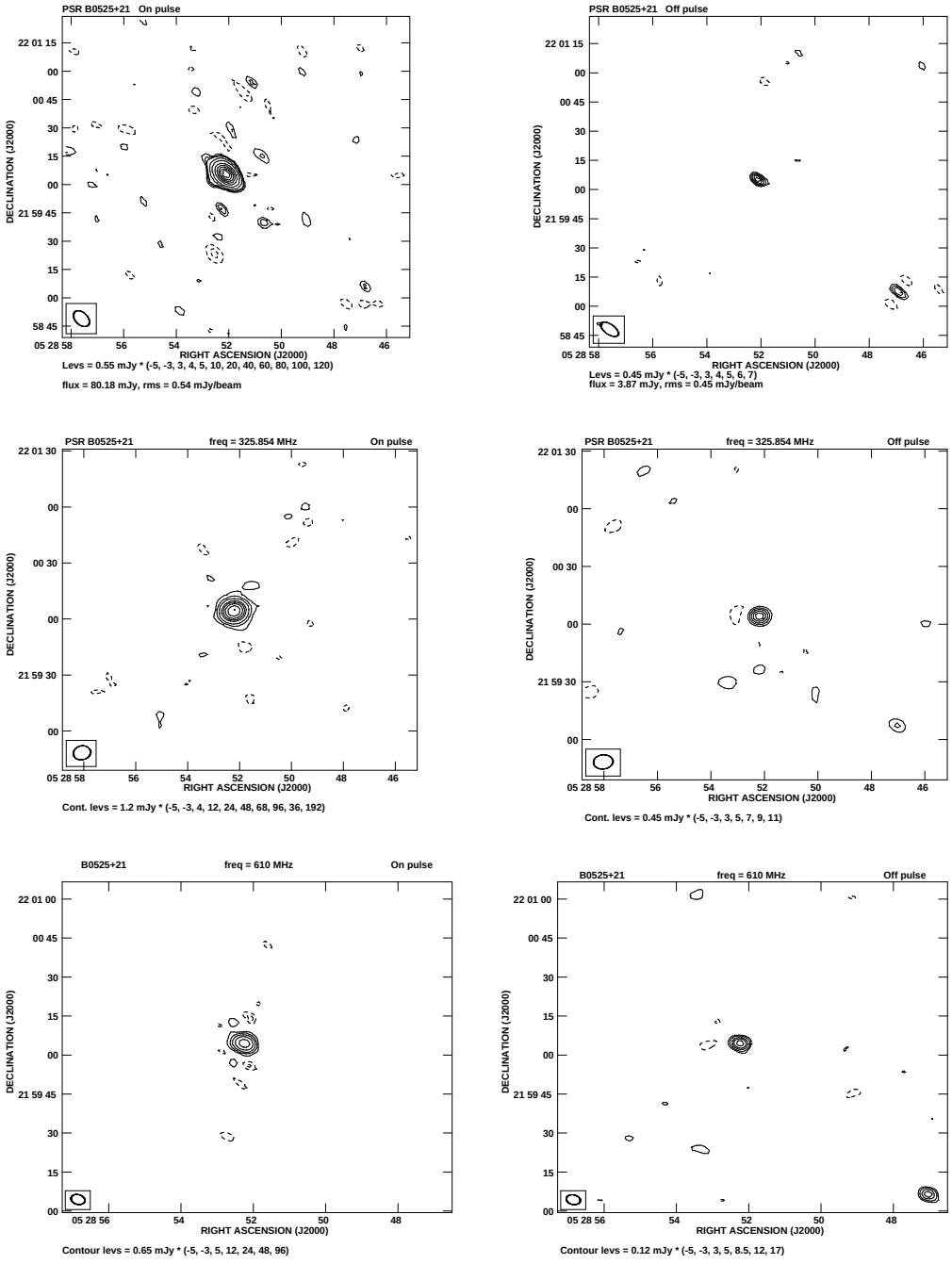

Figure A.1 The figure show the contour maps for the on pulse (left panel) and off pulse (right panel) detections for the pulsar B0525+21. The top panel show the detections for the observations on 18^{th} January, 2010 at 325 MHz. The middle panel show the detections for the observations on 9^{th} July, 2011 at 325 MHz. The bottom panel show the detections for the observations on 22^{nd} July, 2011 at 610 MHz.

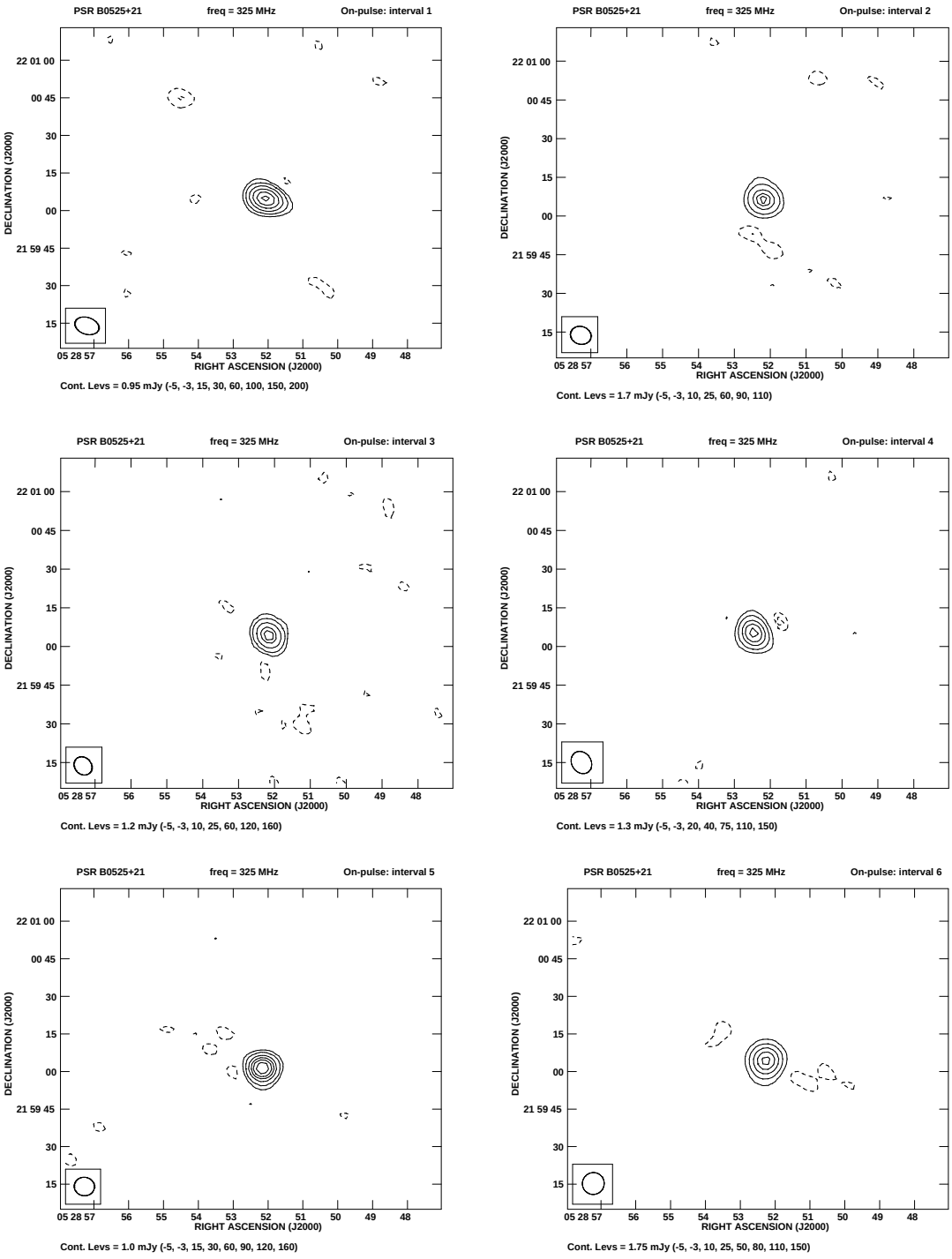

Figure A.2 The figure show the contour maps for the on-pulse emission for short time intervals 35-40 minutes each. The observations were carried out for the pulsar B0525+21 on 8^{th} July, 2011 at the 325 MHz frequency band.

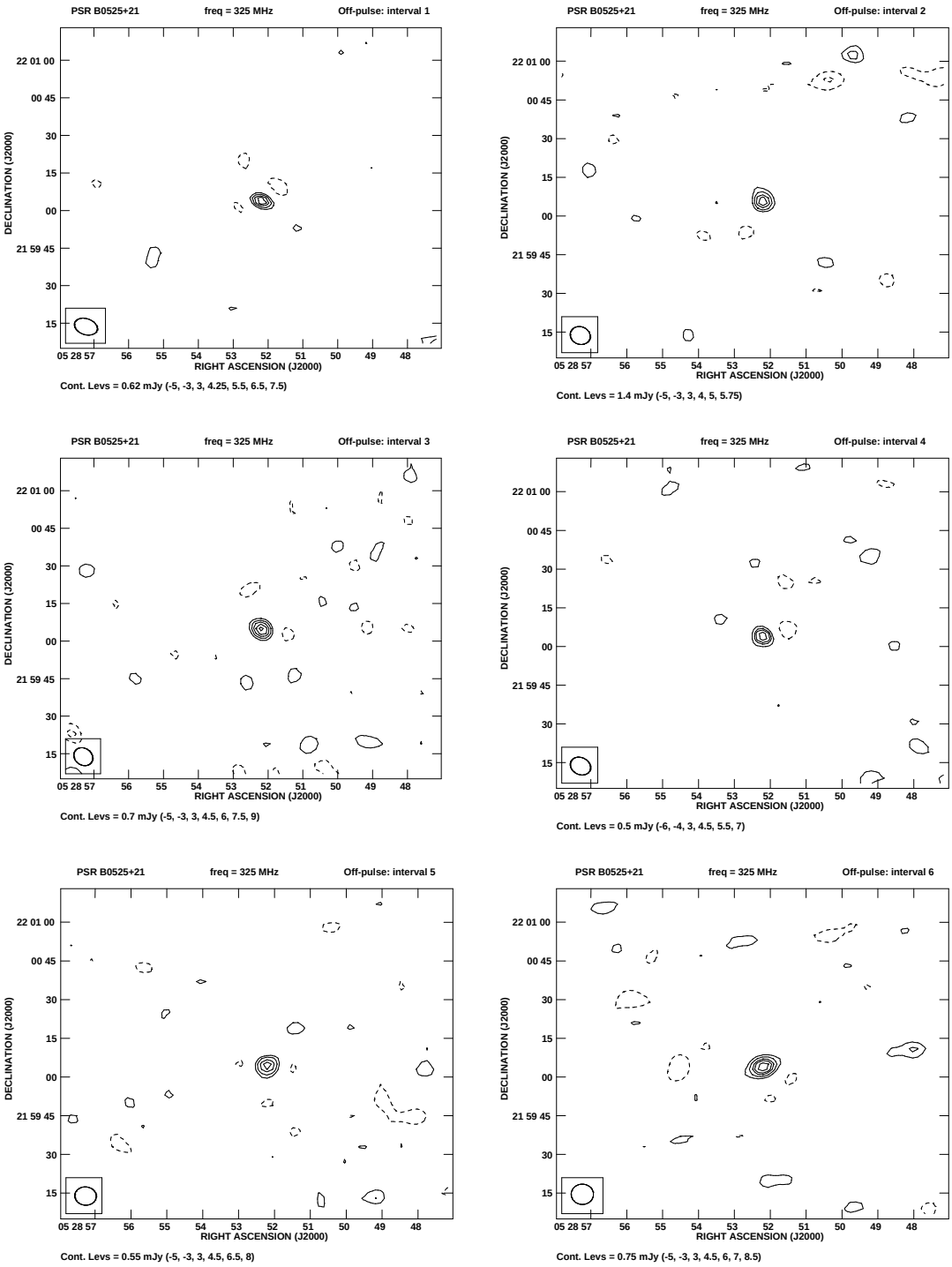

Figure A.3 The figure show the contour maps for the off-pulse emission for short time intervals 35-40 minutes each. The observations were carried out for the pulsar B0525+21 on 8^{th} July, 2011 at the 325 MHz frequency band.

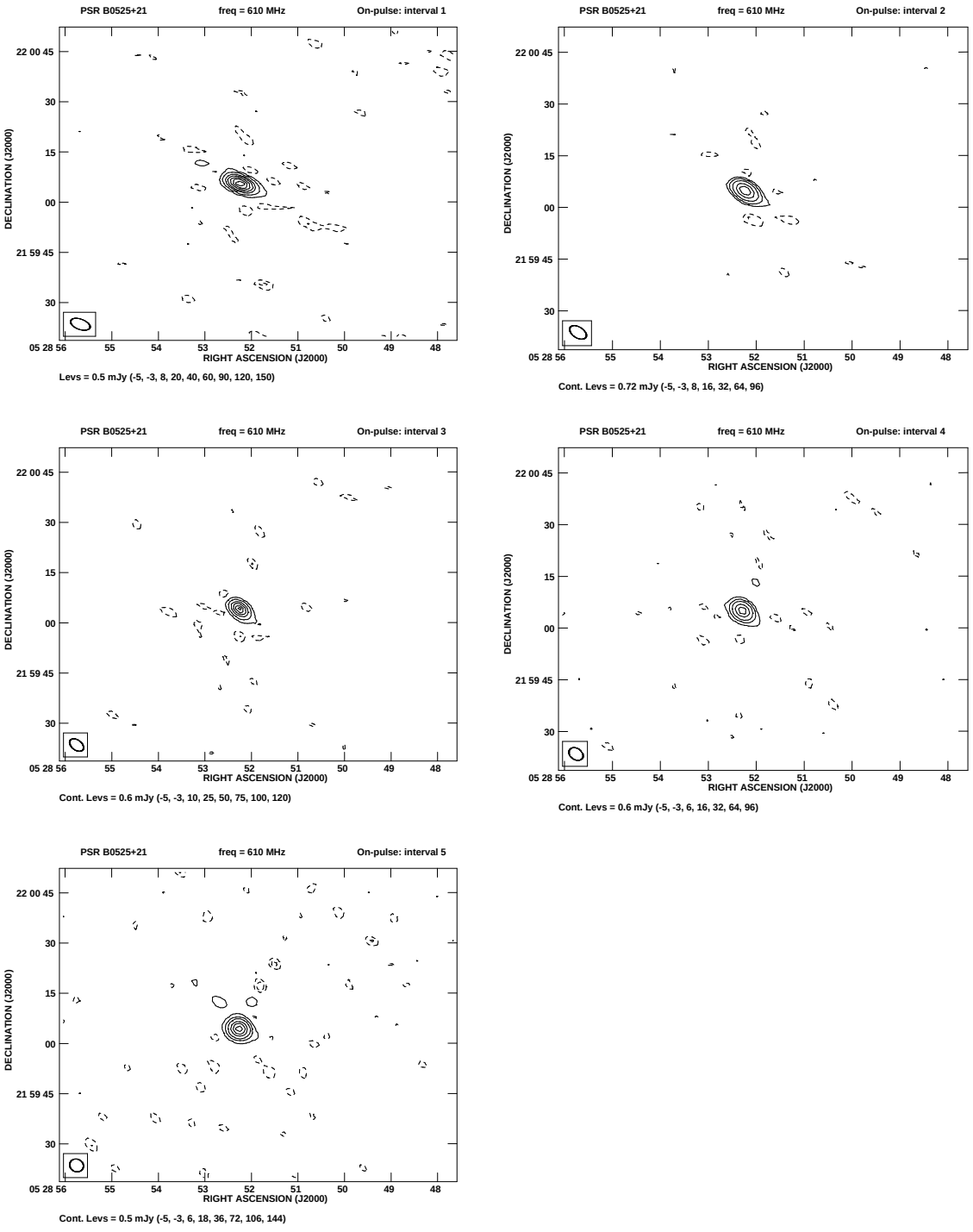

Figure A.4 The figure show the contour maps for the on-pulse emission of B0525+21 at short time intervals 25-30 minutes each. The observations were carried out on 15^{th} February, 2011 at the 610 MHz frequency band. The rest of the figures are shown in next page.

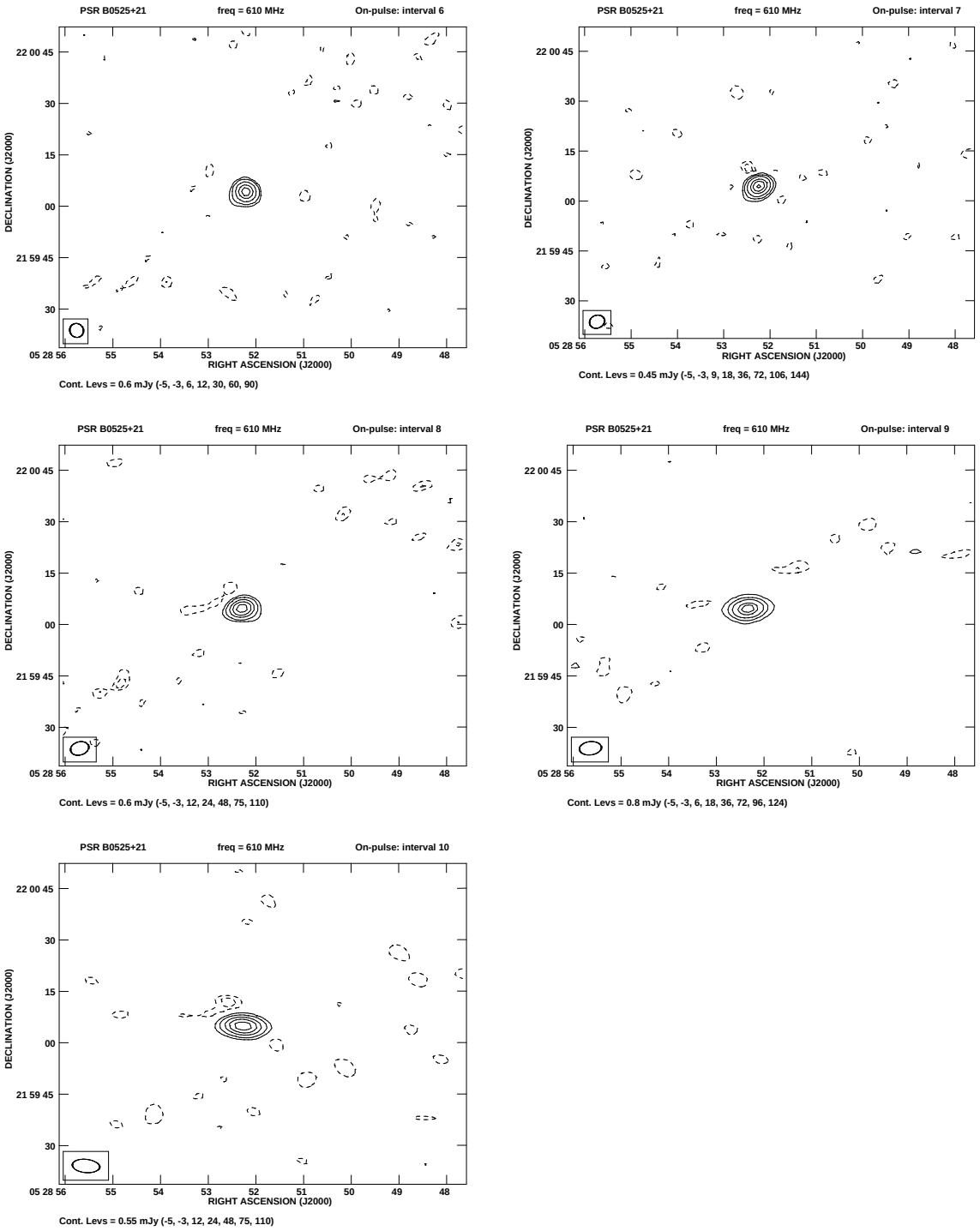

Figure A.5 Continued from previous page. The figure show the contour maps for the on-pulse emission of B0525+21 at short time intervals 25-30 minutes each. The observations were carried out on 15^{th} February, 2011 at the 610 MHz frequency band.

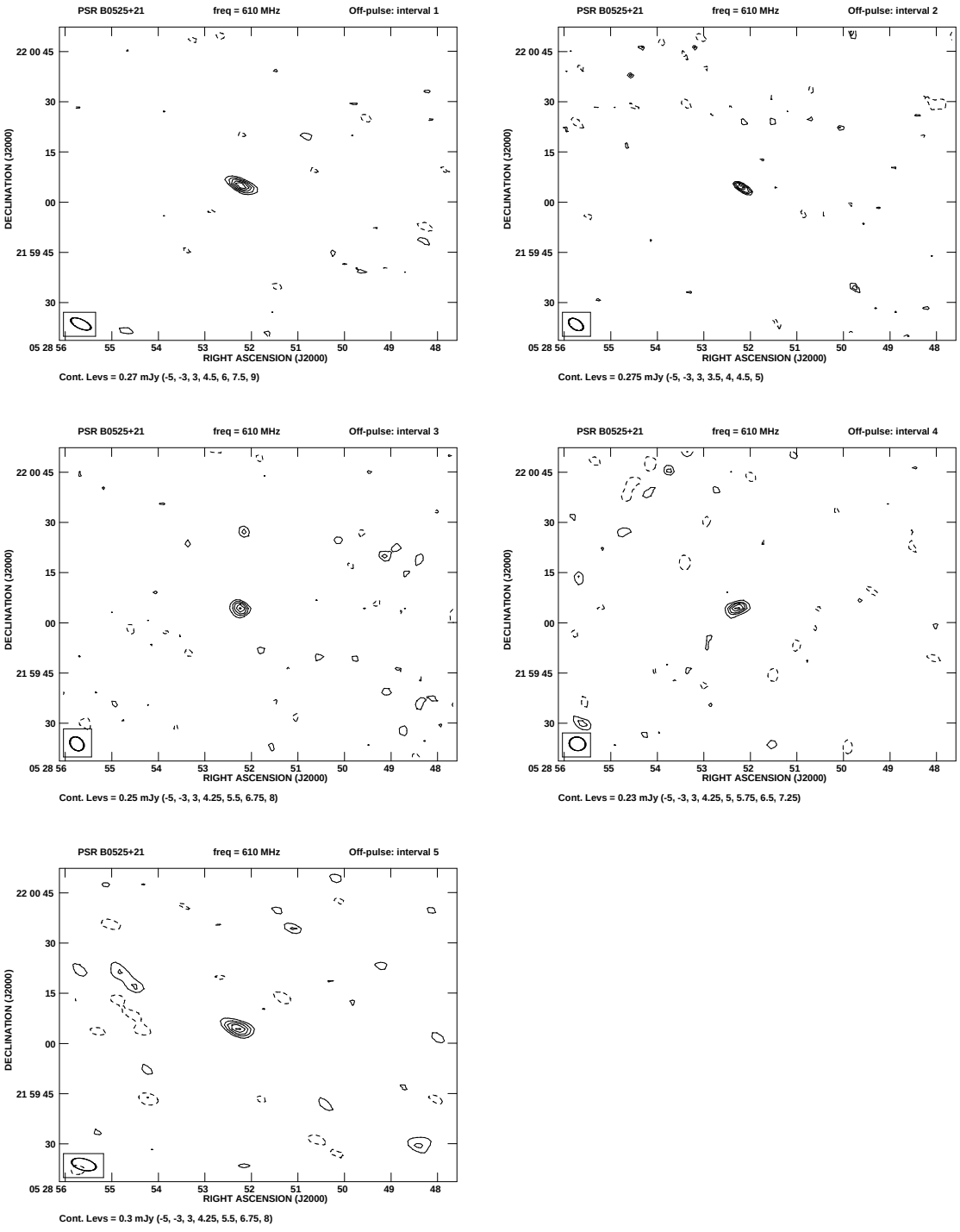

Figure A.6 The figure show the contour maps of the off-pulse emission for B0525+21 at short time intervals, 45-50 minutes each. The observations were carried out on 15^{th} February, 2011 at the 610 MHz frequency band.

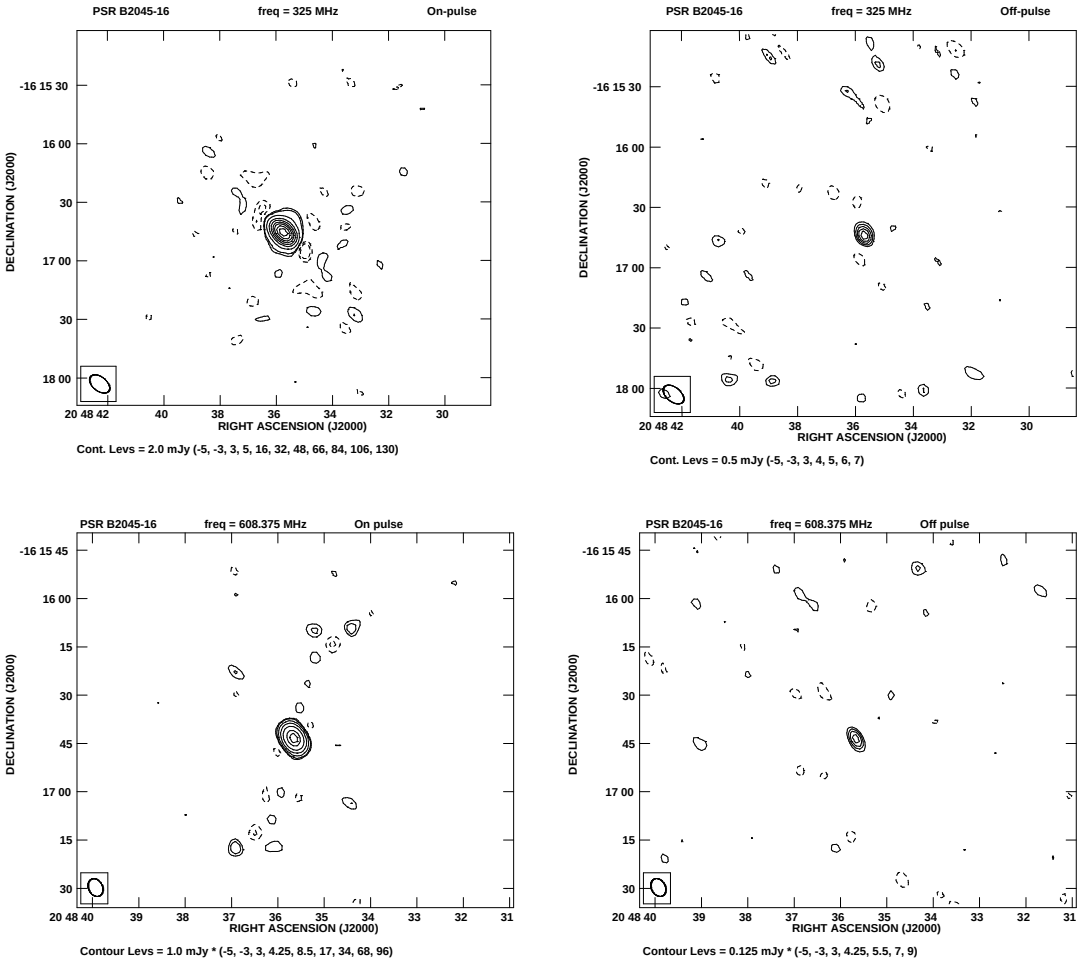

Figure A.7 The figure show the contour maps of the on-pulse (left panel) and off-pulse (right panel) detections for the pulsar B2045–16. The top panel show the detections for the observations on 16^{th} January, 2010 at 325 MHz. The bottom panel show the detections for the observations on 14^{th} February, 2011 at 610 MHz.

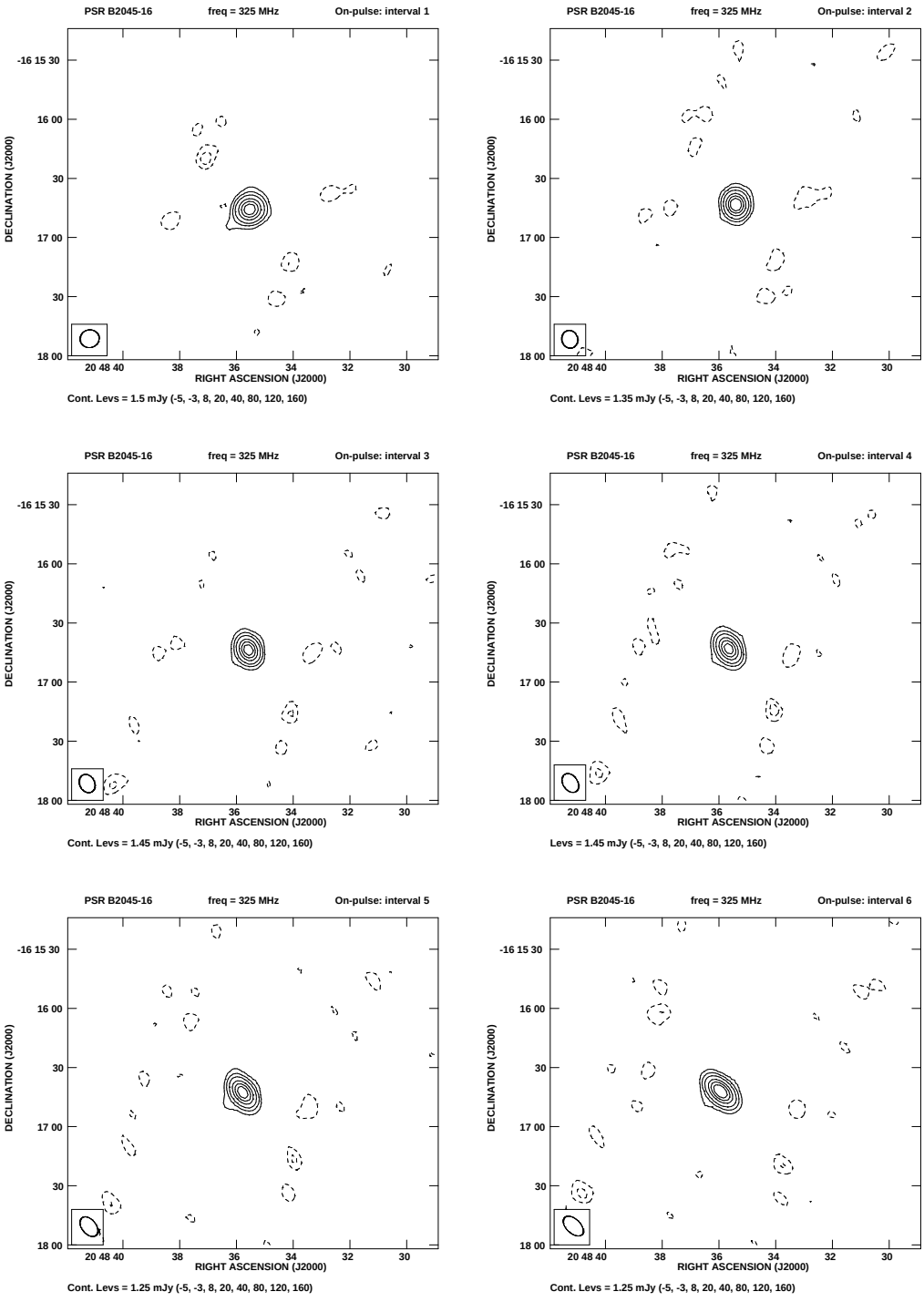

Figure A.8 The figure show the contour maps for the on-pulse emission of the pulsar B2045–16 at short time intervals 40-45 minutes each . The observations were carried out on 3^{rd} August, 2011 at the 325 MHz frequency band.

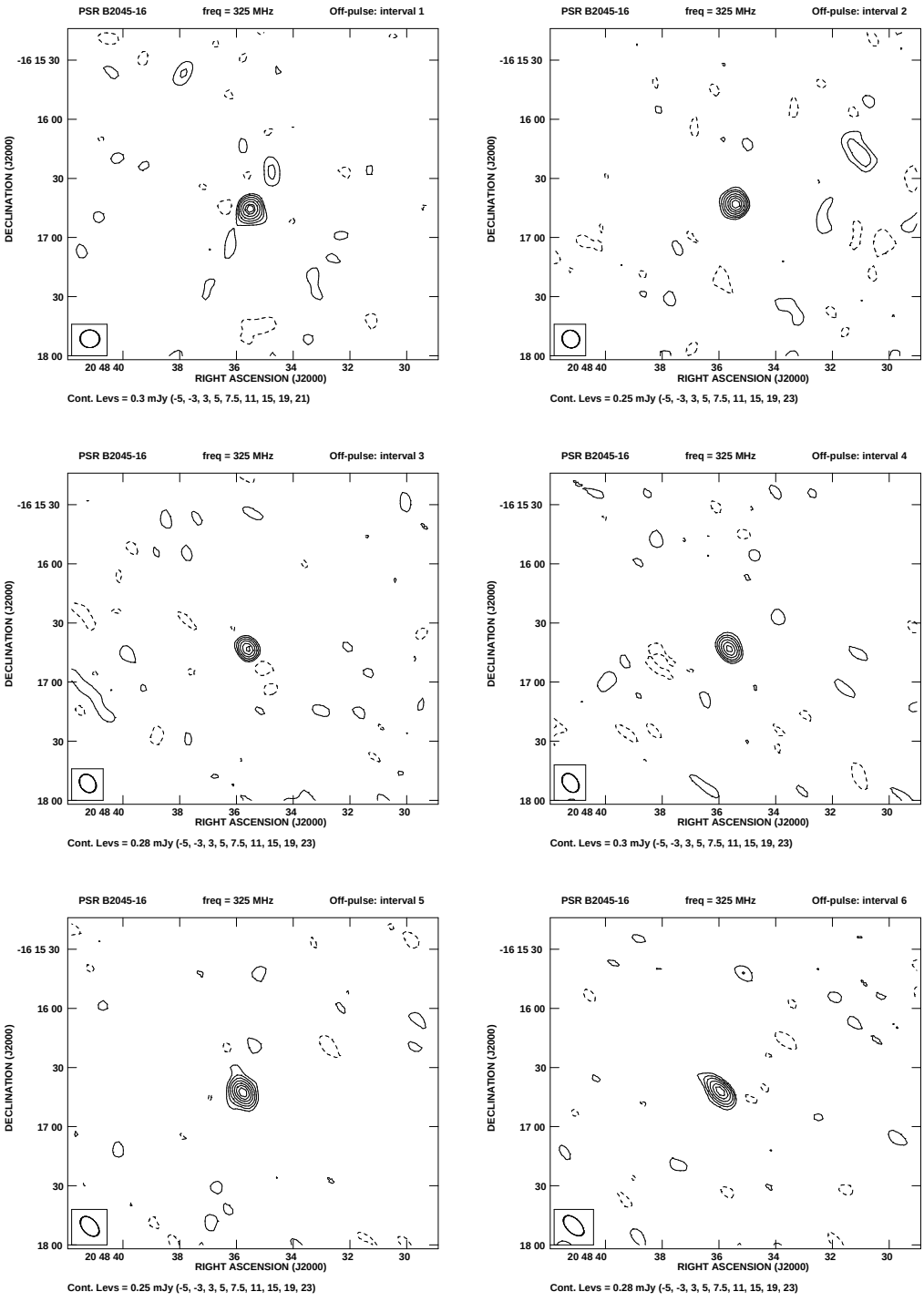

Figure A.9 The figure show the contour maps for the Off-pulse emission of the pulsar B2045–16 at short time intervals 40-45 minutes each. The observations were carried out on 3^{rd} August, 2011 at the 325 MHz frequency band.

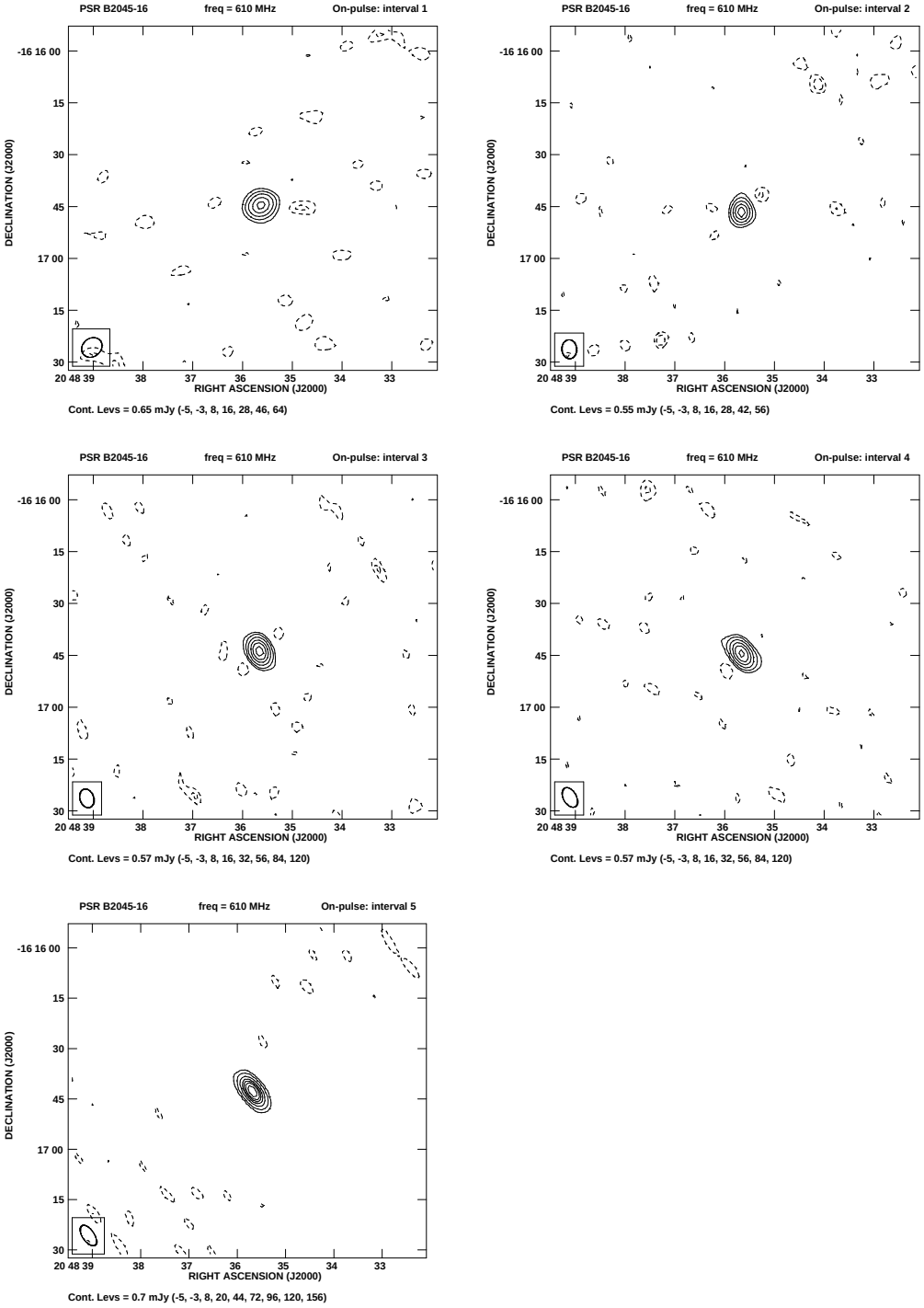

Figure A.10 The figure show the contour maps for the on-pulse emission of the pulsar B2045–16 at short time intervals 40-45 minutes each. The observations were carried out on 14^{th} February, 2011 at the 610 MHz frequency band.

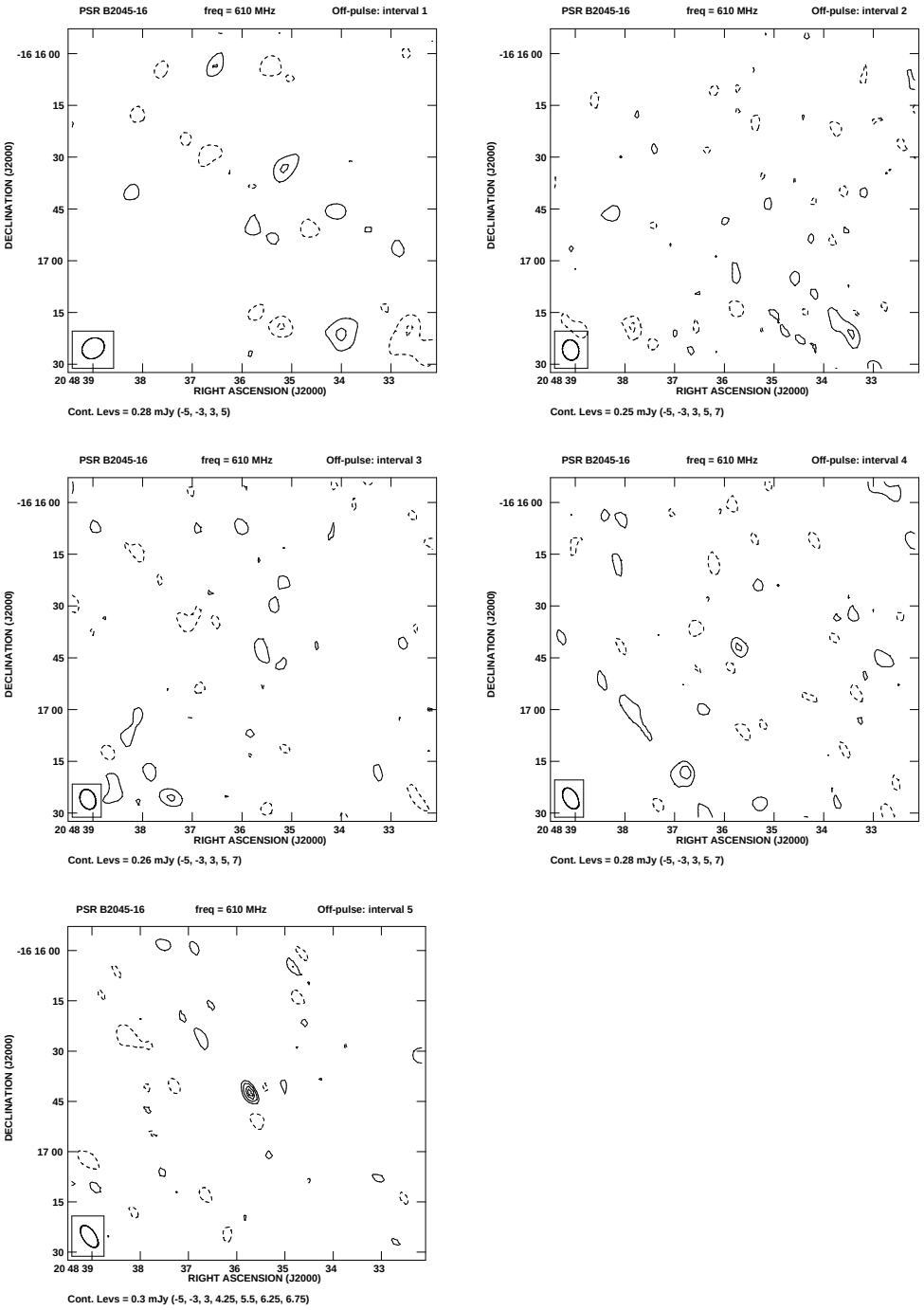

Figure A.11 The figure show the contour maps of off-pulse emission for the pulsar B2045–16 at short time intervals 40-45 minutes each. The observations were carried out on 14^{th} February, 2011 at the 610 MHz frequency band. The off-pulse is only detected in the last image (see section 3.3.2 for detail).

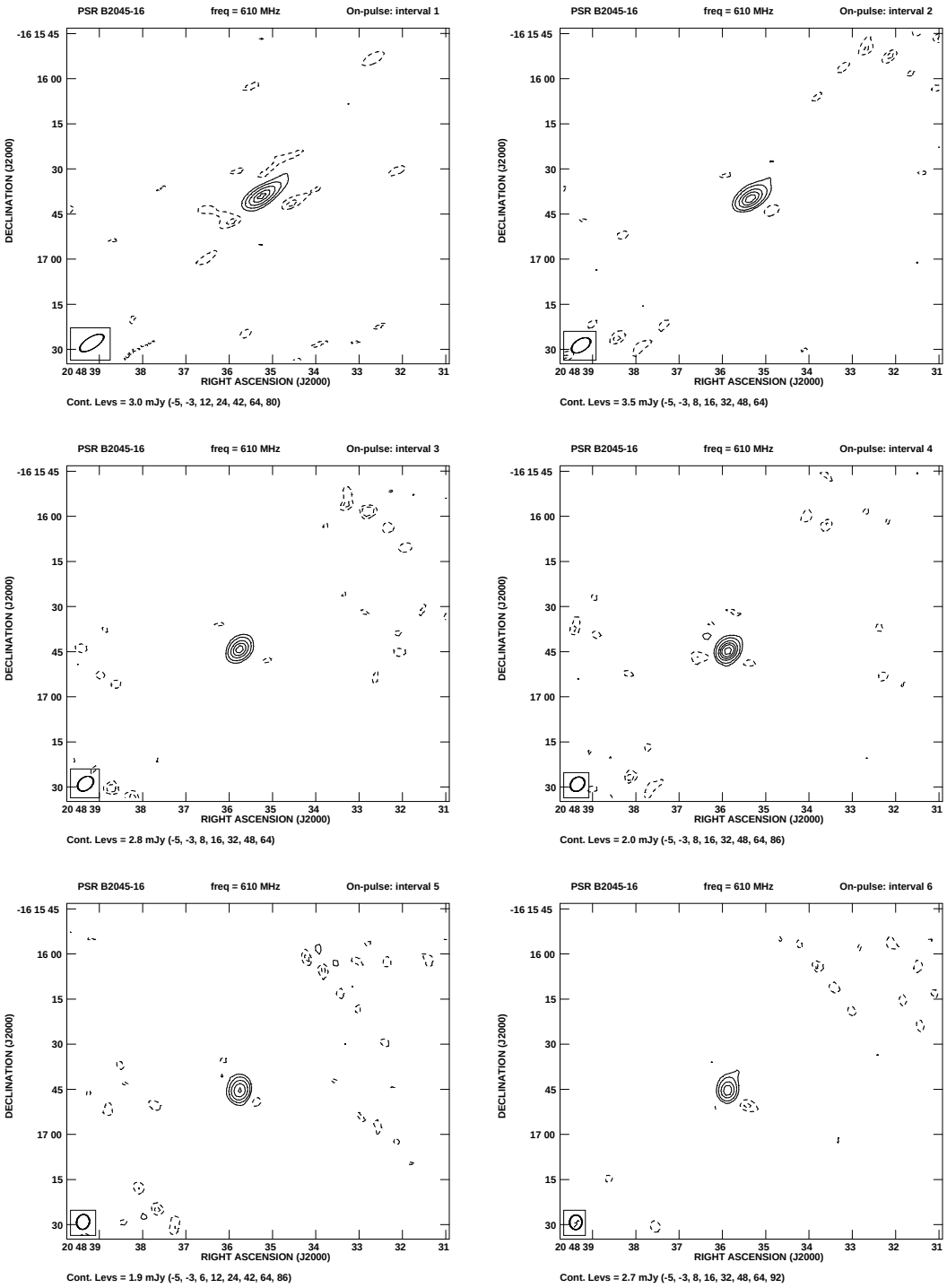

Figure A.12 The figure show the contour maps for the on-pulse emission of the pulsar B2045–16 at short time intervals 20-25 minutes each. The observations were carried out on 25^{th} August, 2011 at the 610 MHz frequency band.

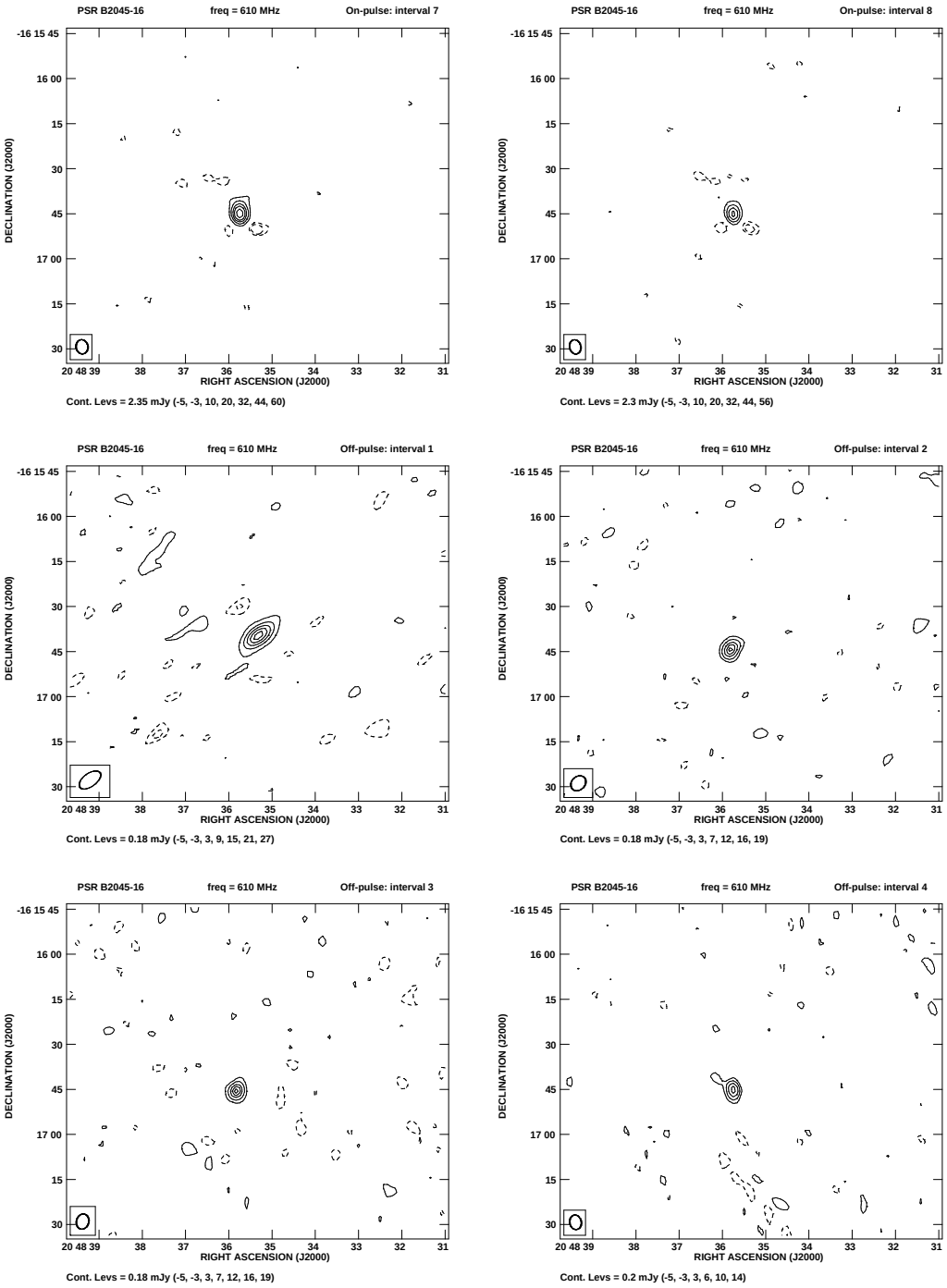

Figure A.13 The figure show the contour maps for the on-pulse (top panel) and off-pulse (middle and bottom panel) of the pulsar B2045–16 at short time intervals of 20-25 minutes each for on-pulse and 40-45 mins for off-pulse. The observations were carried out on 25^{th} August, 2011 at the 610 MHz frequency band.

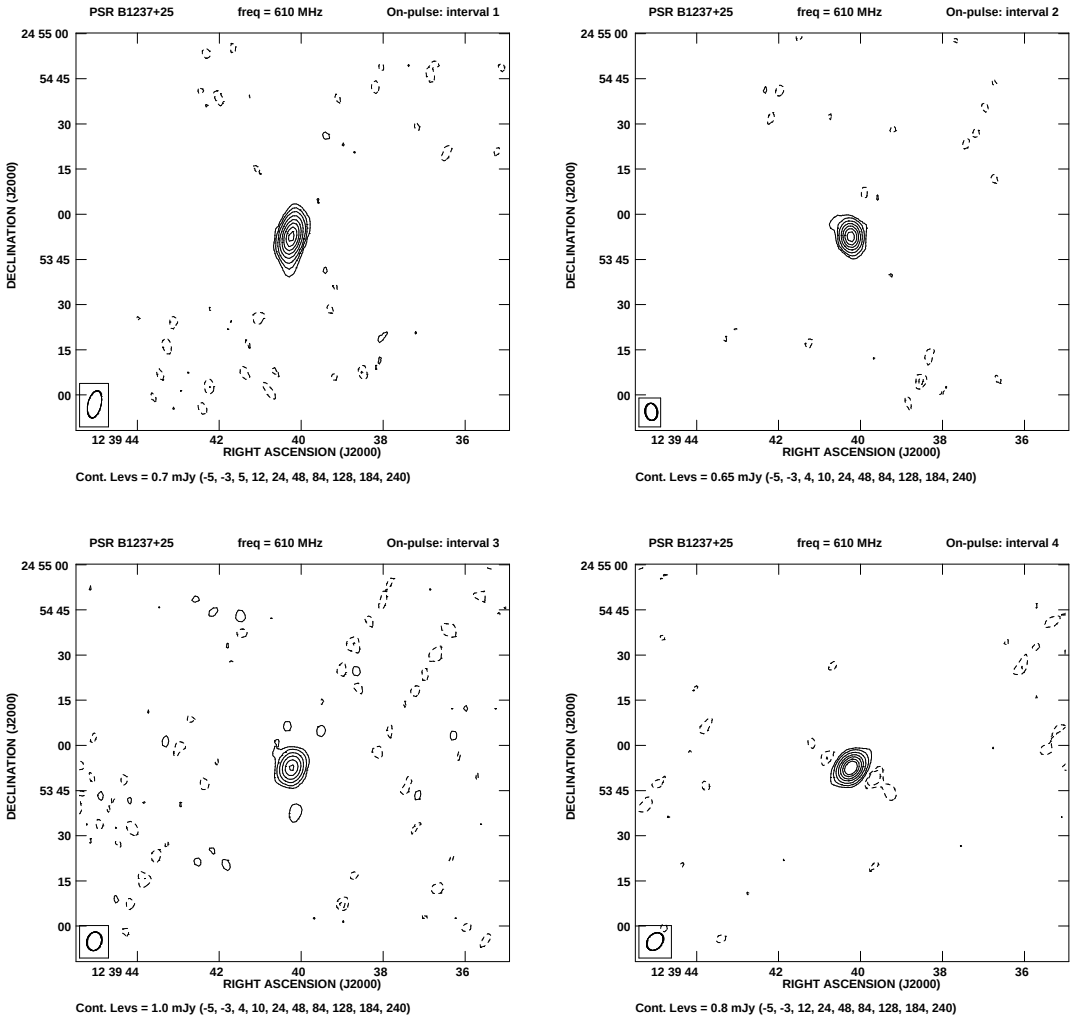

Figure A.14 The figure show the contour maps for the on-pulse emission of the pulsar B1237+25 at short time intervals 40-45 minutes each. The observations were carried out on 13^{th} August, 2011 at the 610 MHz frequency band.

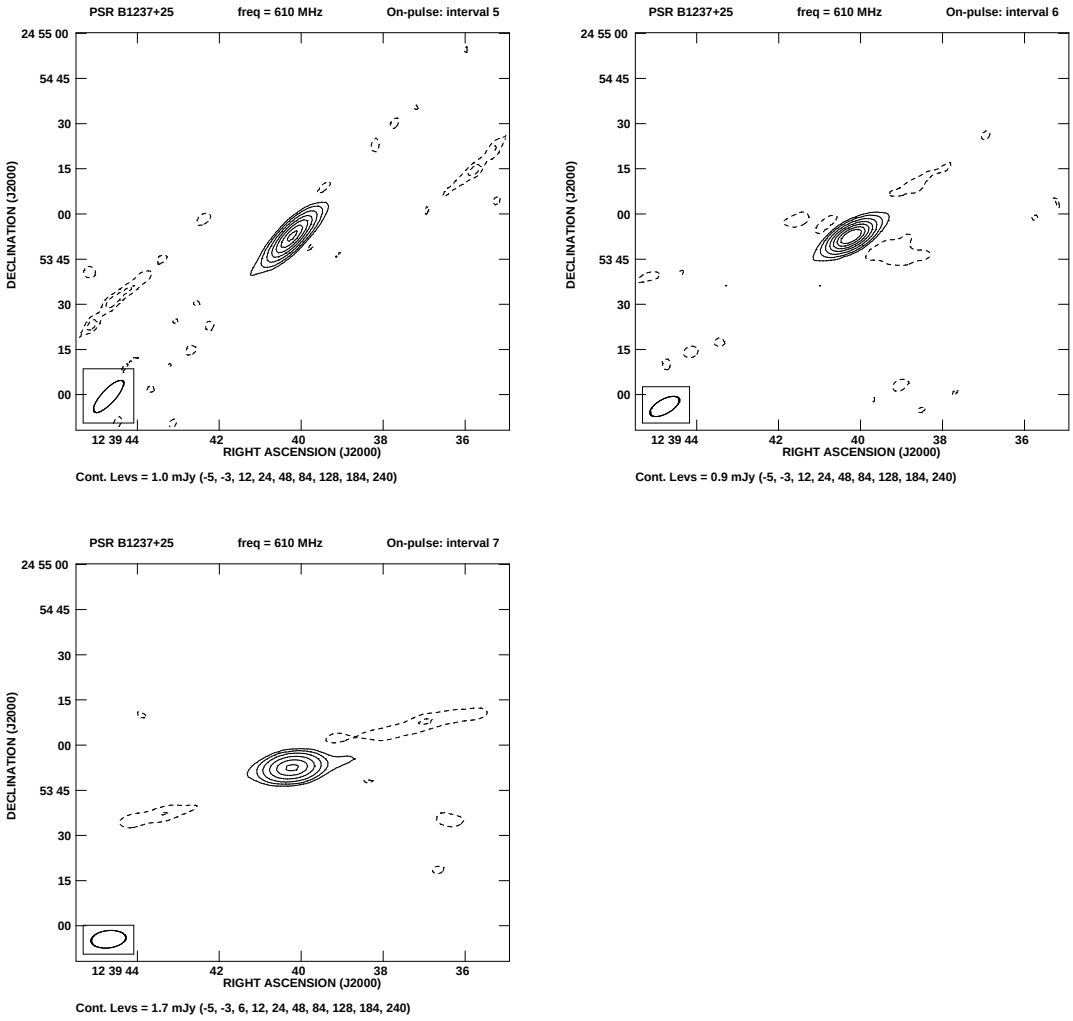

Figure A.15 Continued from last page. The figure show the contour maps for the on-pulse emission of the pulsar B1237+25 at short time intervals 40-45 minutes each. The observations were carried out on 13^{th} August, 2011 at the 610 MHz frequency band.

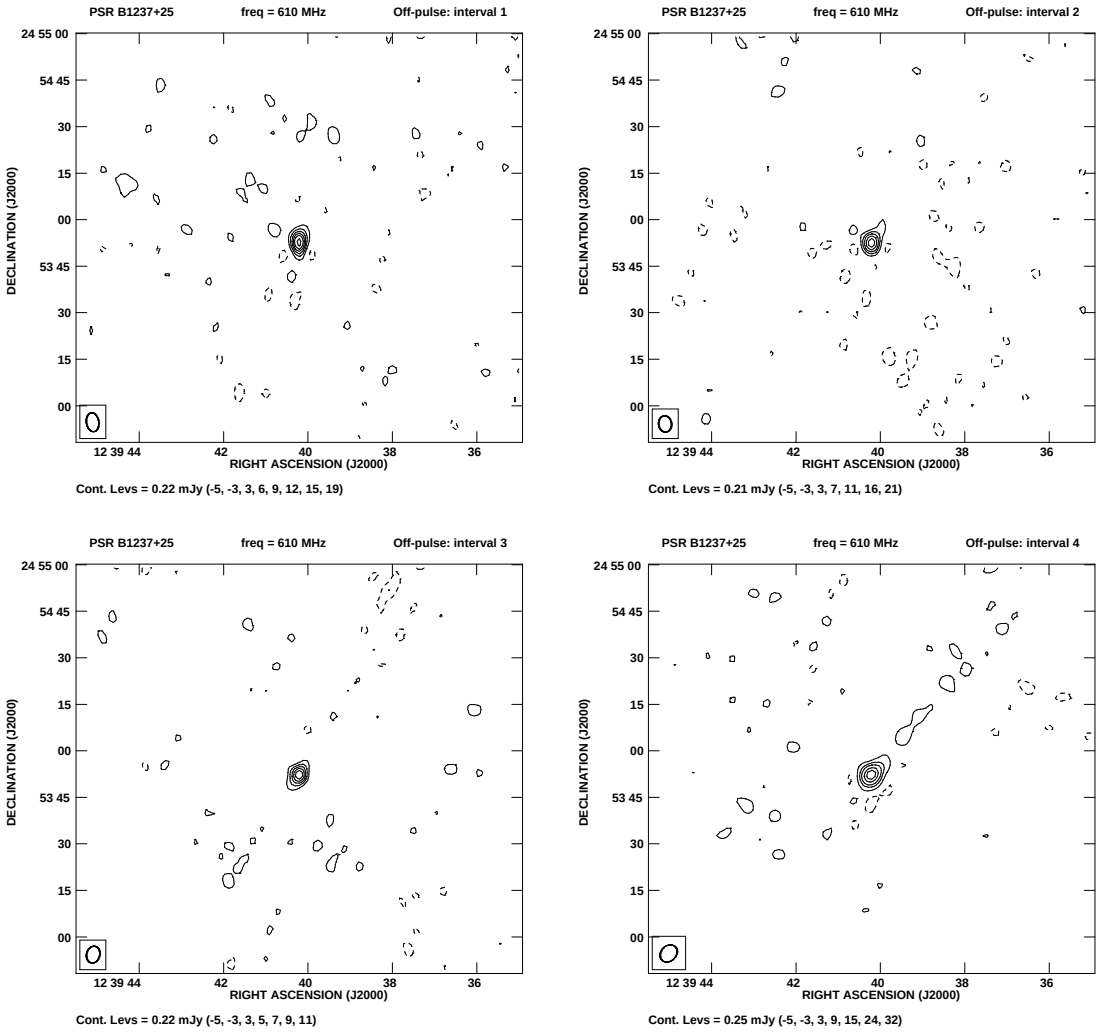

Figure A.16 The figure show the contour maps for the off-pulse emission of the pulsar B1237+25 at short time intervals 40-45 minutes each. The observations were carried out on 13^{th} August, 2011 at the 610 MHz frequency band.

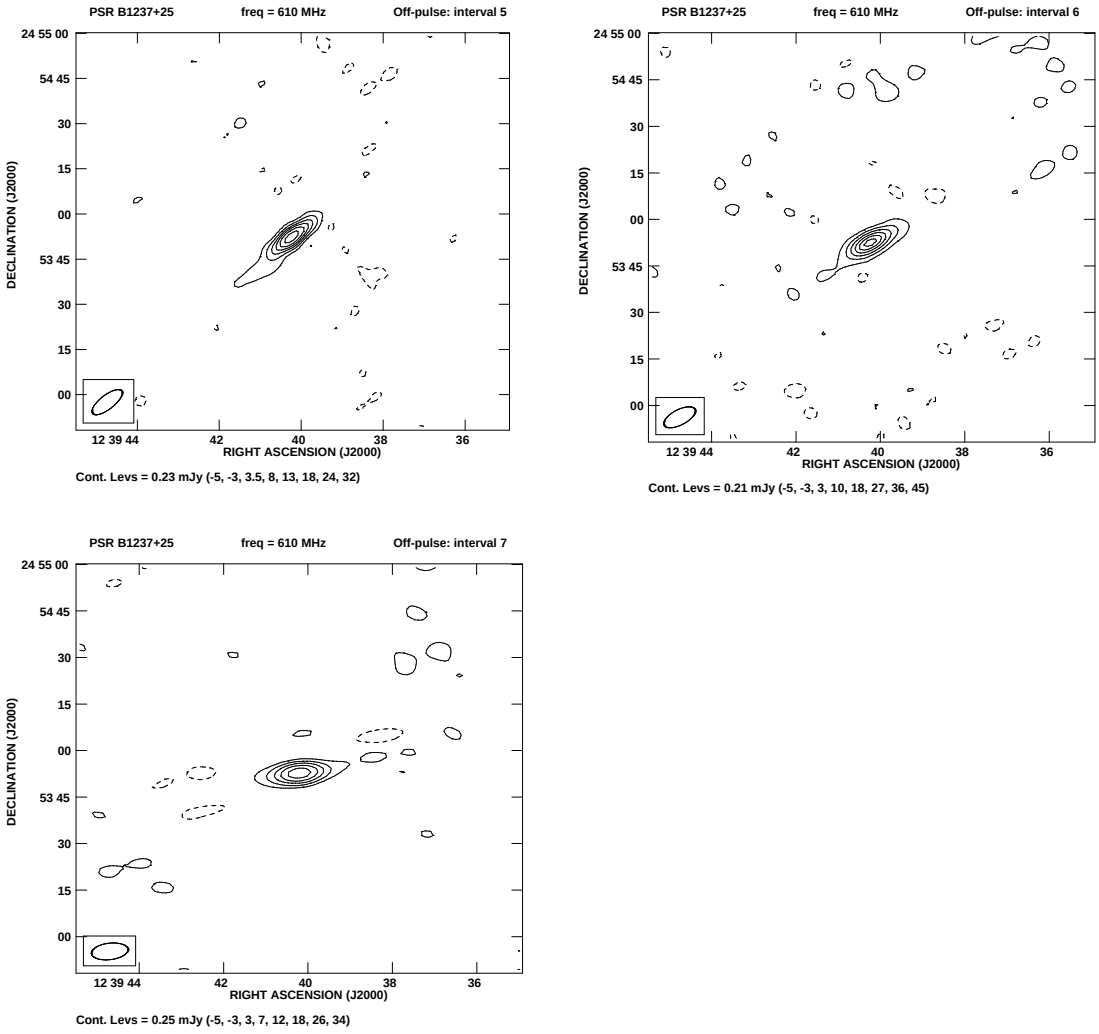

Figure A.17 Continued from last page. The figure show the contour maps for the off-pulse emission of the pulsar B1237+25 at short time intervals 40-45 minutes each. The observations were carried out on 13^{th} August, 2011 at the 610 MHz frequency band.

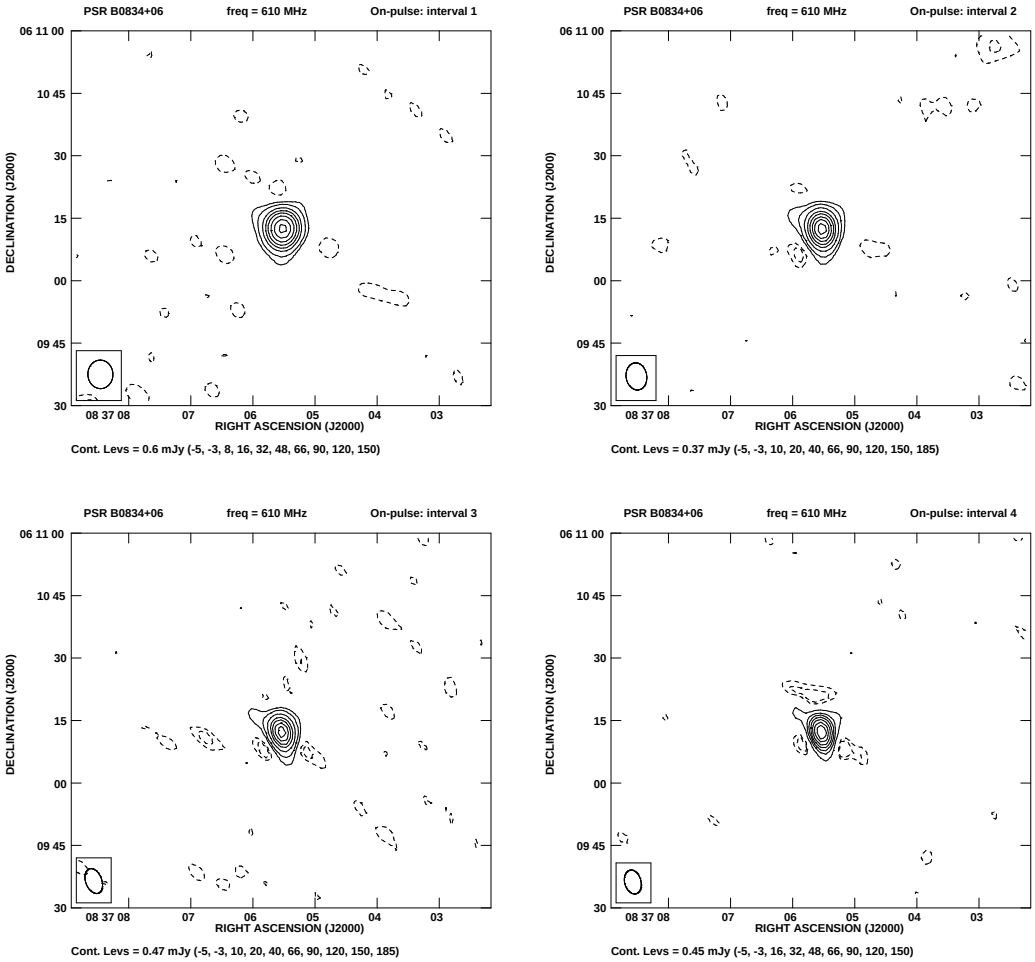

Figure A.18 The figure show the contour maps for the on-pulse emission of the pulsar B0834+06 at short time intervals 40-45 minutes each. The observations were carried out on 27^{th} August, 2011 at the 610 MHz frequency band.

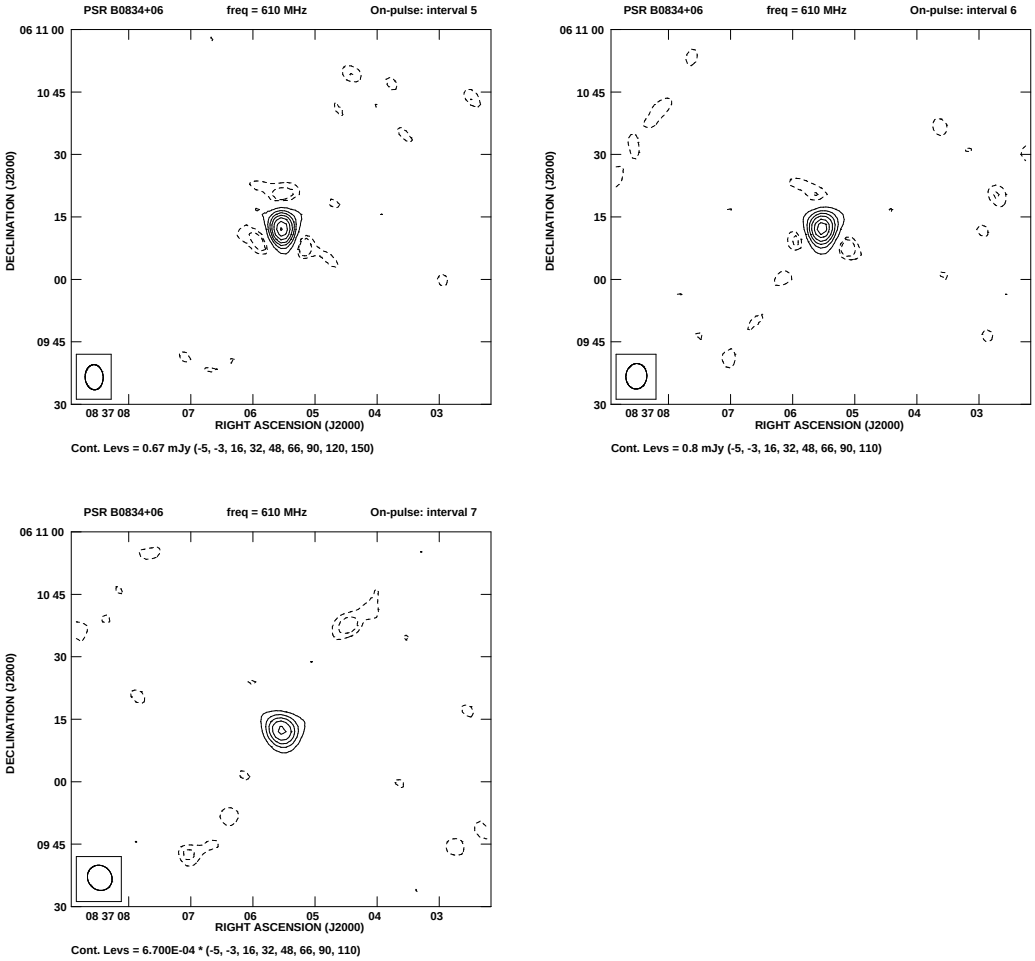

Figure A.19 Continued from last page. The figure show the contour maps for the On-pulse emission of the pulsar B0834+06 at short time intervals 40-45 minutes each. The observations were carried out on 27^{th} August, 2011 at the 610 MHz frequency band.

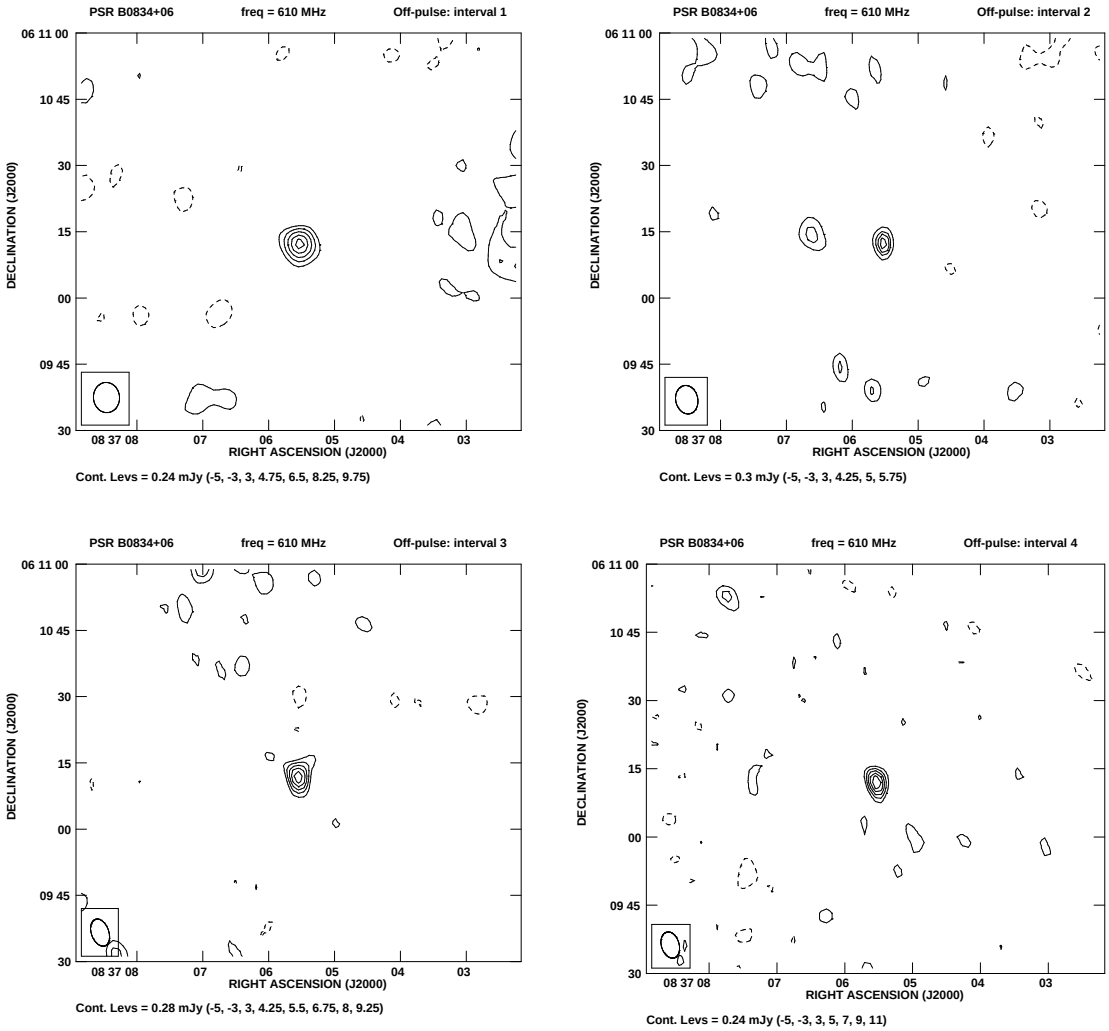

Figure A.20 The figure show the contour maps for the Off-pulse emission of the pulsar B0834+06 at short time intervals 40-45 minutes each. The observations were carried out on 27^{th} August, 2011 at the 610 MHz frequency band.

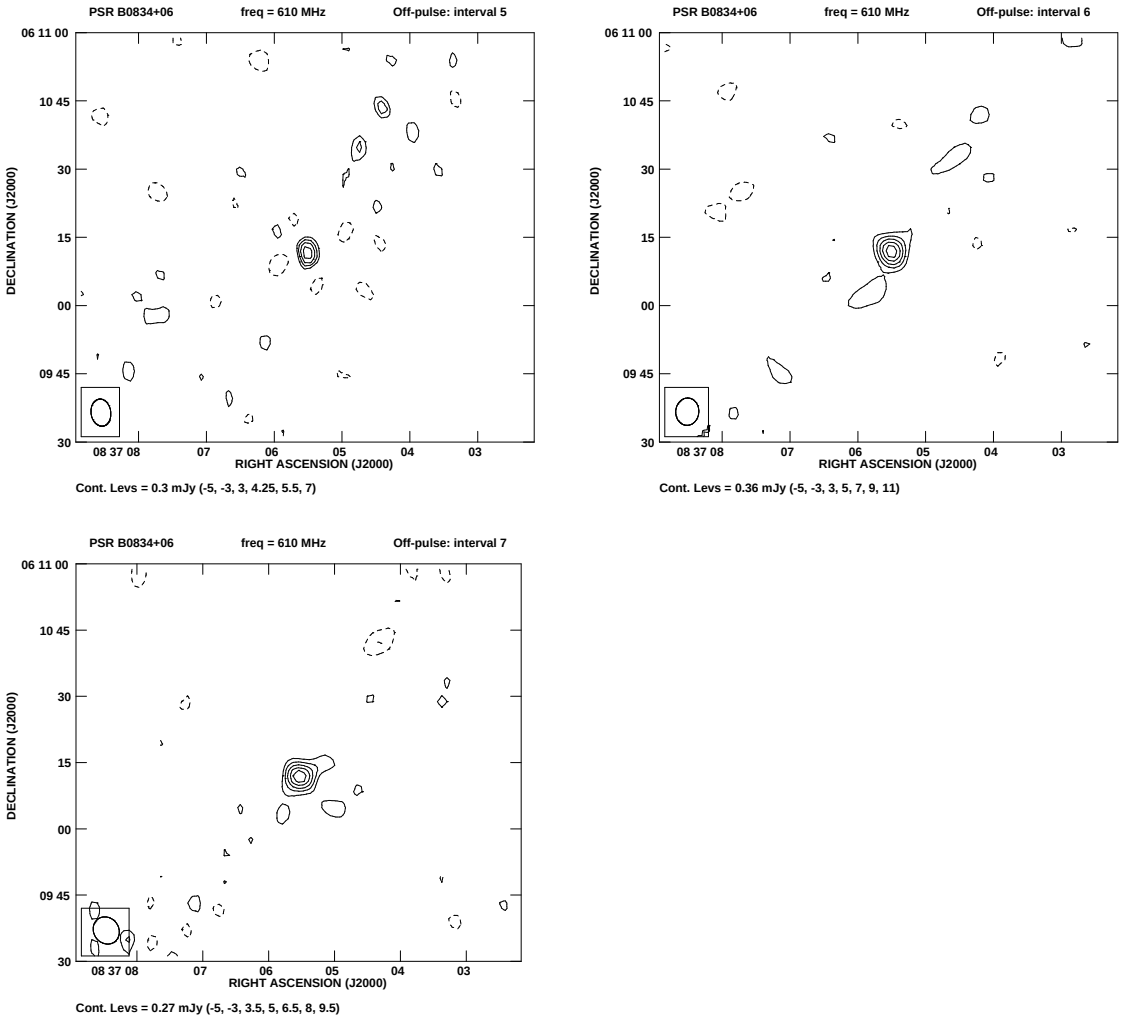

Figure A.21 Continued from last page. The figure show the contour maps for the off-pulse emission of the pulsar B0834+06 at short time intervals 40-45 minutes each. The observations were carried out on 27^{th} August, 2011 at the 610 MHz frequency band.

Bibliography

Asseo, E., Melikidze, G.I. 1998, MNRAS, 301, 59

Arons, J. 1983, Nature, 302, 301

Baars, J. W. M., Genzel, R., Pauliny-Toth, I. I. K., Witzel, A. 1977, A&A, 61, 99

Backus, I., Mitra, D., Rankin, J. M. 2010, MNRAS, 404, 30

Bartel, N., Ratner, M. I., Shapiro, I. I., Cappallo, R. J., Rogers, A. E. E., Whitney, A. R. 1985, AJ, 90, 318

Basu, R., Athreya, R., Mitra D. 2011, ApJ, 728, 157

Basu, R., Mitra D., Athreya, R. 2012, ApJ, 758, 91

Basu, R., Mitra D., Melikidze, G. I. 2013, ApJ, 772, 86

Becker, R. H., White, R. L., Helfand, D. J. 1995, ApJ, 450, 559

Bhat, N. D. R.; Rao, A. P.; Gupta, Y. 1999, ApJS, 121, 483 Blandford, R. D., Ostriker, J. P., Pacini, F., Rees, M. J. 1973, A&A, 23, 145

Blandford, R. D., Ostriker, J. P., Pacini, F., Rees, M. J. 1973, A&A, 23, 145

Blaskiewicz, M.; Cordes, J.M.; Wasserman, I. 1991, ApJ, 370, 643

Chatterjee, S., Cordes, J. M. 2002, ApJ, 575, 407

Cheng, K. S., Ho, C., Ruderman, M. 1986a, ApJ, 300, 500

Cheng, K. S., Ho, C., Ruderman, M. 1986b, ApJ, 300, 522

Cohen, N. L., Cotton, W. D., Geldzahler, B. J., Marcaide, J. M. 1983, ApJ, 264, 273

Cordes, J. M. 1978, ApJ, 222, 1006

Dyks, J., Rudak, B., Harding, A. K. 2004, ApJ, 607, 939

Everett, J. E., Weisberg, J. M. 2001; ApJ, 553, 341

Frail, D. A., Giacani, E. B., Goss, W. M., Dubner, G. 1996, ApJ, 464, 165

Frail, D. A., Kulkarni, S .R. 1991, Nature, 352, 785

Frail, D. A., Scharringhausen, B. R. 1997, ApJ, 480, 364

Gangadhara, R. T., Gupta, Y. 2001, ApJ, 555, 31

Gangadhara, R. T. 2005, ApJ, 628, 923

Gaensler, B. M., Stappers, B. W., Frail, D. A., Johnston, S. 1998, ApJ, 499, 69

Gaensler, B. M.; Slane, P. O. 2006, ARA&A, 44, 17

Gaensler, B. M., Stappers, B. W., Frail, D. A., Moffett, D. A., Johnston, S., Chatterjee, S. 2000, MNRAS, 318, 58

Giacani, E. B., Frail, D. A., Goss, W. M., Vieytes, M. 2001, AJ, 121, 3133

Gil, J. A.; Gronkowski, P.; Rudnicki, W. 1984, A&A, 132, 312

Gil, J. A.; Jessner, A.; Kijak, J.; Kramer, M.; Malofeev, V.; Malov, I.; Seiradakis, J. H.; Sieber, W.; Wielebinski, R. 1994, A&A, 282, 45

Gil, J.; Lyubarsky, Y.; Melikidze, G.I. 2004, ApJ, 600, 872

Gil, J.; Melikidze, G. I.; Geppert, U. 2003, A&A, 407, 315

Gil, J.A.; Sendyk, M. 2000, ApJ, 541, 351

Glushak, A. P., Pynzar, A. V., Udaltsov, V. A. 1981, Soviet Ast., 25, 182

Gopal-Krishna 1978, MNRAS, 185, 521

Goldreich, P., Julian, W. H. 1969, ApJ, 157, 869

Gould, D. M., Lyne, A. G. 1998, MNRAS, 301, 235

Gupta, Y., Gangadhara, R. T. 2003, ApJ, 584, 418

Hankins, T. H., Fowler, L. A. 1986, ApJ, 304, 256

Hankins, T. H., Moffett, D. A., Novikov, A., Popov, M. 1993, ApJ, 417, 735

Hankins, T. H., Rickett, B. J. 1975, Methods in comp phy., 14, 55

Hester, J. J., Kulkarni, S. R. 1988, ApJ, 331, L121

Hewish, A., Bell, S.J., Pilkington, J.D.H., Scott, P.F., Collins, R.A. 1968, Nature, 217, 709

Hobbs, G., Lyne, A. G., Kramer, M., Martin, C. E., Jordan, C. 2004, MNRAS, 353, 1311

Kazbegi, A.Z.; Machabeli, G.Z.; Melikidze, G.I. 1987, AuJPh, 40, 755

Kazbegi, A.Z.; Machabeli, G.Z.; Melikidze, G.I. 1991, MNRAS, 253, 377

Kijak, J.; Gil, J. 1998, MNRAS, 288, 631

Kijak, J.; Gil, J. 1998, MNRAS, 299, 855

Kijak, J.; Gil, J. 2003, A&A, 397, 969

Kijak, J.; Lewandowski, W.; Maron, O.; Gupta, Y.; Jessner, A. 2003, A&A, 531, 16

Kothes, R.; Landecker, T.L.; Reich, W.; Safi-Harb, S.; Arzoumanian, Z. 2008, ApJ, 687, 516

Krzeszowski, K.; Mitra, D.; Gupta, Y.; Kijak, J.; Gil, J.; Acharyya, A. 2009, MNRAS, 393, 1617

Latham, C.; Mitra, D.; Rankin, J. 2012, MNRAS, 427, 180

Lorimer, D.R.; Yates, J.A.; Lyne, A.G.; Gould, D.M. 1995, MNRAS, 273, 411

Lyne, A. G., Manchester, R. N. 1988, MNRAS, 234, 477

Lyutikov, M.; Blandford, R.D.; Machabeli, G. 1999, MNRAS, 305, 338

Malov, I.F., Suleimanova, S.A. 1998, ARep, 1998, 388

Manchester, R.N; Hobbs G.B.; Teoh, A.; Hobbs, M. 2005, AJ, 129, 1993

Maciesiak, K.; Gil, J.; Melikidze, G. I. 2012, MNRAS, 424, 1762

Maron, O.; Kijak, J.; Kramer, M.; Wielebinski, R. 2000, A&AS, 147, 195

Melikidze, G.I.; Gil, J.A.; Pataraya, A.D. 2000, ApJ, 544, 1081

Medin, Z.; Lai, D. 2010, MNRAS, 406, 1379

Mitra, D. 2012, Electromagnetic Radiation from Pulsars and Magnetars. Proceedings of a Conference held at University of Zielona Góra, Zielona Góra, Poland, 24-27 April 2012. San Francisco: Astronomical Society of the Pacific, 2012, p.141

Mitra, D., Deshpande, A. A. 1999, A&A, 346, 906

Mitra, D.; Gil, J.; Melikidze, G. I. 2009, ApJ, 696, 141

Mitra, D.; Konar, S.; Bhattacharya, D. 1999, MNRAS, 307, 459

Mitra, D.; Rankin, J.M. 2002, ApJ, 577, 322

Mitra, D., Li, X. H. 2004, A&A, 421, 215

Mitra, D., Rankin, J. M. 2011, ApJ, 727, 92

Mitra, D.; Gil, J.; Melikidze, G.I. 2009, ApJ, 696, 141

Perry, T. E., Lyne, A. G. 1985, MNRAS, 212, 489

Radhakrishnan, V., Cooke, D. J. 1969; Aph. Lett, 3, 225

Rankin, J. M. 1983, ApJ, 274, 333

Rankin, J. M. 1990, ApJ, 352, 247

Rankin, J. M. 1993, ApJ, 405, 285

Rankin, J.M. 1993, ApJS, 85, 145

Rathnasree, N., Rankin, J. M. 1995, ApJ, 452, 814

Rickett, B.J. 1990, ARA&A, 28, 561

Ruderman, M. A., Sutherland, P. G. 1975, ApJ, 196, 51

Schönhardt, R. E. 1973, nature phy. sci, 243, 62

Schönhardt, R. E. 1974, A&A, 35, 13

Spitkovsky, A. 2006, ApJ, 648, L51

Stappers, B. W., Gaensler, B. M., Johnston, S. 1999, MNRAS, 308, 609

Strom, R. G., Van Someren Greve, H. W. 1990, Ap&SS, 171, 351

Stinebring, D.R., Condon, J.J, 1990, ApJ, 352, 207

Stinebring, D.R., Smirnova T.V., Hankins, T.H., Hovis, J.S., Kaspi, V.M., Kempner, J.C., Myers E., Nice D.J. 2000, ApJ, 539, 300

Sturrock, P. A. 1971, ApJ, 164, 529

Swarup, G., Ananthakrishnan, S., Kapahi, V. K., Rao, A. P., Subrahmanya, C. R., Kulkarni, V. K. 1991, Current Sci., 60, 95

Taylor, J. H., Manchester, R. N., Lyne, A. G. 1993, ApJS, 88, 529

Thomson, A. R., Moran, J. M., Swenson G. W. 1986, Interferometry and Synthesis in Radio Astronomy (Wiley Interscience, New York).

Treumann, R. A. 2006, A&A Rev., 13, 229

Ursov, V. N., Usov, V. V. 1987, Ap&SS, 140, 325

Weiler, K. W., Goss, W. M., Schwarz, U. J. 1974, A&A, 35, 473

Weiler, K.W., Sramek, R.A. 1988, ARA&A, 26, 295